

**Sorption of Metal Ions onto Sedimentary Rock
in the Presence of Gamma-Irradiated Humic Acid**

2022

Zhao Qi

Acknowledgement

A dissertation is a long and solitude journey. Since I came to Japan in September 2018, I had received many supports and helps from my family, my teachers and friends.

First and most importantly, I would like to express my deepest gratitude and appreciation to my supervisor Prof. T. Sasaki. I am very grateful that he accepted me as a PhD student. I am very happy and lucky to obtain this opportunity to work in his lab for the unforgettable three years. His enthusiasm for research has been contagious and has given me the inspiration to keep going. His intelligence and attitude to science and research will enlighten and guide my future career forever. There is no doubt that he is the excellent, patient and qualified supervisor. I would like to thank Prof. T. Kobayashi for his helps during my Ph.D. study. He always provided me with many helpful guidance in the experiment and valuable suggestions about experiments and dissertation writing. He never minded my visits to his office for lots of questions and help. I can't imagine that I could achieve my study successfully without his guidance and help. I would also like to express great appreciation to Prof. I. Takagi for his review of this thesis, and Ms. Souma for her document assistance. I am really thankful for they constant encouragement. My heartfelt thanks to every previous and current member in Laboratory of Nuclear Materials during the past three years, although I could not recall some names. I am very grateful to enjoy a happy life with them. My life in Japan was so colorful and interesting because of the friendship. Moreover, it is a nice memory that we take the group seminar every Tuesday. My sincere gratitude is also expressed to Prof. T. Saito (KUANS, Kyoto University), Prof. M. Yoneda, Dr. N.Thuong, Mr. Fajri (Laboratory of Environmental Risk Analysis, Kyoto University) and Dr. K. Miyakawa, Dr. H. Sasamoto (Horonobe Underground Laboratory, JAEA), who have contributed to this thesis in equipment or materials. I am also grateful that they took much

time to review my thesis very carefully and gave me many valuable suggestions.

Lastly, I would like to thank my family for all their love and encouragement. Because of the faithful supports and encourages from my parents throughout my Ph.D. periods, I have the motivation and confidence to go on. I would also acknowledge China Scholarship Council for the financially support on my life and work at Japan, and Kyoto University for the three-year tuition full exemption.

Zhao Qi

In Katsura Campus, Kyoto University

March 2022

Abstract

High-level waste (HLW), which refer to the highly radioactive materials produced as a byproduct of the reactions that occur inside nuclear reactors, are potentially hazardous. The radionuclides in neutron-irradiated uranium-based fuel, such as ^{135}Cs and ^{243}Am , are planned to be buried in well-engineered deep underground repositories after fuel reprocessing, vitrification, and packing. Although the possibility of early failure of waste packages after repository closure is extremely low, percolation of groundwater into the repositories can be an issue. The radionuclides can leach into natural groundwater systems from fractured waste packages and subsequently migrate to the biosphere. The migration of radionuclides released from repositories is expected to be significantly affected by their sorption on the host rock interface. Humic substance (HS) molecules can react with metal ions and form metal–HS complexes, which are also considered as organic metal colloids. The complexation of HS with metal ions has been demonstrated to affect the sorption behavior of metal ions in groundwater. The gamma rays stemming from the decay of radionuclides can pass through the steel canister of the waste packages, with the surface dose of the HLW package being estimated to be over 0.1 kGy/h, even after 50 years of cooling. This gamma irradiation would affect the chemical properties of HSs and the interactions between HSs and metal ions.

This study was primarily aimed at exploring the effects of a gamma-irradiated HS solution on the sorption of metal ions. To this end, the influence of gamma irradiation on the complexation of HS with metal ions was clarified, along with the apparent formation constants and complexation affinity in terms of the molecular-weight fraction.

The effects of gamma irradiation on the complexation of HS with calcium ions were investigated. Three types of HS solutions with different origins were gamma-irradiated using a ^{60}Co source to 0–500 kGy at dose rates of 1 kGy/h and 0.1 kGy/h. The molecular and

chemical properties of the HS were evaluated using total organic carbon (TOC) measurements, UV–Vis spectrometry, ^{13}C nuclear magnetic resonance, and acid–base titration. A possible mechanism of the influence of radiolysis on the HSs was proposed. The complexation ability of the irradiated HS with Ca^{2+} ions was studied using a Ca ion-selective electrode. The apparent formation constants of the Ca–HS complexes were found to increase as the irradiation dose increased, which was attributed to the relative increase in the ratio of phenolic –OH groups to the carboxylic groups of the HS. The contribution of the phenolic –OH groups to the stability of the complexes was suppressed at a pH of 5 owing to their high acid dissociation constants. In addition, the gamma-irradiation dose rates of 1 kGy/h and 0.1 kGy/h did not significantly affect the properties of the HS and the apparent formation constants of the Ca–HS complexes.

The effects of gamma irradiation on the molecular weight of metal–humic-acid (HA) complexes and the complexation affinity were investigated. Non-irradiated and irradiated HA molecules were fractionated by ultrafiltration into four categories: >100, 50–100, 10–50, and <10 kDa. TOC measurements and potentiometric titration analysis suggested that (1) certain gamma-irradiated HA molecules degraded into smaller molecules, and (2) the radiolytic-degradation-induced phenolic –OH became the predominant functional group in the low-molecular-weight fractions of HA. The effects of the absorbed dose on the distributions of Cs^+ , Sr^{2+} , and Eu^{3+} ions in the molecular-weight fractions of the metal–HA systems were examined to analyze the complexation affinity. The metal ions were distributed in the lower-molecular-weight fractions at different doses, which corresponded to the degradation of HA molecules. Monovalent Cs^+ ions did not modify the molecular weight distribution of the TOC of the degraded HA molecules, whereas the Sr^{2+} and Eu^{3+} ions redistributed the TOC toward the higher-molecular-weight fractions.

The influences of HA and its radiological degradation on the sorption of Cs^+ and Eu^{3+}

by sedimentary rock obtained from the Horonobe Underground Research Laboratory in Japan were investigated. A batch sorption experiment was performed to evaluate the effects of gamma-irradiated HA on the sorption of Cs^+ and Eu^{3+} ions. The addition of non-irradiated HA weakened the sorption of Eu because of the lower sorption of the neutral or negatively charged Eu–HA complexes compared with that of free Eu ions. The sorption of Cs^+ was barely affected by the presence of irradiated HA. The concentration ratios of the HA-complexed species, which included decomposed HA, and the non-complexed species in the solid and liquid phases were evaluated by sequential filtration and chemical equilibrium calculations. The ratio was low in both phases for Cs, which suggested minimal contribution of the HA to the sorption of Cs. However, the ratio for Eu^{3+} in the liquid phase was high, indicating the higher complexing ability of HA to Eu^{3+} than that of HA to Cs^+ ions. Therefore, the sorption of free Eu^{3+} was found to dominate in scenarios where the gamma irradiation dose was applied to the HA solution under the gamma radiation field near the HLW package.

Existing sorption databases have been widely established over decades in various countries for evaluating the sorption of metal ions in groundwater. The results obtained in this study provide new insight on considering the effects of the long-term gamma irradiation field in the presence of HSs while evaluating the retardation and acceleration effects of radionuclide migration, which is crucial for the safety assessment of nuclear waste disposal.

Contents

List of Figures -----	XI
List of Tables -----	XV
List of Abbreviations -----	XVII
Chapter 1 Introduction -----	1
1.1 Nuclear energy -----	1
1.2 Nuclear wastes -----	3
1.3 Final disposal of nuclear wastes -----	6
1.3.1 Concept of deep geological repository-----	6
1.3.2 GDF-related policies and scheduling in various countries-----	9
1.3.3 Underground research laboratory-----	12
1.4 Short- and long-term evolutions of GDF -----	13
1.4.1 Waste package as an artificial barrier-----	13
1.4.2 Groundwater in deep underground locations-----	14
1.4.3 Gamma irradiation around waste packages-----	15
1.4.4 Leaching of radionuclides in vitrified waste-----	18
1.5 Humic substance -----	18
1.5.1 Natural organic matter in areas of deep geological waste repositories-----	18
1.5.2 Classification and chemical properties of HSs-----	19
1.5.3 Complexation of metal ions with HSs-----	22
1.5.4 Size distribution of metal–HA complexes-----	26
1.6 Sorption behavior of radionuclides -----	28
1.6.1 Sorption of metal ions in GDF-----	28
1.6.2 Impact of gamma irradiation on radionuclide sorption-----	31
1.7 Objective of the thesis -----	33
Reference -----	37
Chapter 2 Effect of gamma irradiation on the complexation of humic substances with Ca²⁺ ions -----	51
2.1 Introduction -----	51

2.2	Experimental -----	52
2.2.1	Preparation of HS samples -----	52
2.2.2	Gamma irradiation on HS samples -----	54
2.2.3	Characterization of irradiated HS solution -----	55
2.2.4	Determination of apparent formation constant-----	56
2.3	Theoretical -----	57
2.4	Results and discussion -----	60
2.4.1	pH and appearance of HS solution -----	60
2.4.2	TOC measurements of HS solution-----	61
2.4.3	UV–Vis spectrometry -----	62
2.4.4	¹³ C NMR analysis-----	65
2.4.5	Titration of functional groups -----	66
2.4.6	Effect of gamma irradiation on Ca–HS complexation -----	70
2.5	Summary -----	72
	Reference -----	73

Chapter 3	Gamma-irradiation-induced molecular-weight distribution and complexation affinity of humic acid with Cs⁺, Sr²⁺ and Eu³⁺ -----	77
3.1	Introduction -----	77
3.2	Experimental -----	78
3.2.1	Preparation of irradiated HA samples -----	78
3.2.2	Sequential ultrafiltration -----	79
3.2.3	Characterization of irradiated HA samples -----	80
3.2.4	Experiment on molecular weight distribution of metal–HA complexes -----	80
3.2.5	Accuracy of ultrafiltration -----	81
3.3	Theoretical -----	82
3.4	Results and discussion -----	83
3.4.1	Chemical characteristics of HA solution-----	83
3.4.2	Distribution of TOC in molecular-weight fractions -----	85
3.4.3	Determination of –COOH and phenolic –OH group contents -----	87
3.4.4	Distribution of Cs ⁺ , Sr ²⁺ , and Eu ³⁺ ions in the metal–HA molecular weight fractions-----	91

3.4.5 Dependence of the gamma irradiation with complexation affinity in molecular-weight fractions-----	93
3.5 Summary -----	95
Reference -----	97
Chapter 4 Sorption of Cs⁺ and Eu³⁺ ions onto sedimentary rock in the presence of gamma-irradiated humic acid-----	103
4.1 Introduction -----	103
4.2 Materials and methods-----	104
4.2.1 Collection of sedimentary rock samples -----	104
4.2.2 Characterization methods of sedimentary rock samples -----	105
4.2.3 Preparation and characterization of irradiated HA solution -----	107
4.2.4 Sorption experiment -----	108
4.3 Theoretical -----	108
4.4 Results and discussion -----	115
4.4.1 Characterization of Horonobe sedimentary rock sample -----	115
4.4.2 Chemical properties of gamma-irradiated HA solution-----	117
4.4.3 Effect of gamma irradiation on the sorption of HA molecules-----	118
4.4.4 Effect of gamma irradiation on the sorption of Cs ⁺ and Eu ³⁺ ions -----	120
4.5 Summary -----	126
Reference -----	128
Chapter 5 Conclusions, significance of the study, and recommendations for future work -----	135
5.1 General conclusions-----	135
5.2 Significance of this thesis -----	137
5.3 Recommendations for future research -----	140
Reference -----	141

List of Figures

- Fig. 1-1** Schematic of HLW disposal in Japan (multi-barrier concept)..... 7
- Fig. 1-2** Conceptualization of groundwater flow in and around Horonobe URL area..... 15
- Fig. 1-3 (a)** Classification of humic substances (HSs), and the difference in physiochemical properties; **(b)** Hypothetical structures of humic acid (HA) and fulvic acid (FA). It is worth noting that HA and FA are not pure substance, but mixtures of various substances with similar chemical properties. 20
- Fig. 1-4** Typical chemical interactions (sorption and complexation) of radionuclides (M) in a groundwater system. 29
- Fig. 1-5** Primary products from gamma-irradiation-induced radiolysis of water 31
- Fig. 2-1** Flow diagram of purification of Aldrich humic acid (AL-HA) based on the pH solubility of organic components 53
- Fig. 2-2** Dependence of total organic carbon (TOC) content on dose and dose rate 62
- Fig. 2-3** UV–Vis absorption spectra of non-irradiated and irradiated HS samples **(a)**: 1 kGy/h; **(b)**: 0.1 kGy/h..... 63
- Fig. 2-4** Dependence of organic carbon content of several types of C atoms in a sample of S-HA on gamma irradiation dose at dose rate of 1 kGy/h..... 65
- Fig. 2-5** Experimental titration data of humic substances obtained via nonlinear fitting. The points and solid lines represent experimental data and the fitting equations with six parameters Q_1 , Q_2 , K_1 , K_2 , m_1 , m_2 , respectively. **(a)**: 1 kGy/h; **(b)**: 0.1 kGy/h..... 67
- Fig. 2-6** Simplified radiolysis mechanisms of humic substances (HS): **(a)** decarboxylation and **(b)** hydroxylation..... 69
- Fig. 2-7** Dependence of $\log \beta_{\text{app}}$ on gamma irradiation dose and dose rate; here β_{app} is the apparent formation constant of the Ca–HS complexes at pH 5 and 0.01 mol/dm³ (NaClO₄); Q_1 and Q_2 denote the organic charge densities of –COOH and phenolic –OH groups, respectively; solid and broken lines represent the eye guide..... 70
- Fig. 2-8** Distribution of Ca²⁺ ions concentration complexed with HS before and after gamma irradiation; the percentages represent the ratios of [CaR₂] (darker areas) to [Ca²⁺]_{tot}; here [CaR₂] and [Ca²⁺]_{tot} denote the concentration of Ca²⁺ ions bound to HS and that of the added Ca²⁺ ion solution. 71
- Fig. 3-1** Diagram of HA purification procedure..... 79
- Fig. 3-2 (a)** Logarithm dependence of absorbed dose on [H⁺]; the square plot at 0 kGy is highlighted and the solid line represents the linear fitting relationship. **(b)** Color of

- humic acid (HA) solutions at different absorbed dose. (c) Dependence of absorbed dose on the zeta potential of HA samples (pH of 8, ionic strength of 0.05 mol/dm³). The error bars indicate the standard deviations for three measurements. 84
- Fig. 3-3** Fractional distribution of total organic carbon in solution (ionic strength of 0.05 mol/dm³, pH of 8) with absorbed dose: (a) humic acid (HA) and (b) Cs–HA, Sr–HA, and Eu–HA systems. Here, UF₁, UF₂, UF₃, and UF₄ denote the >100, 50–100, 10–50, and <10 kDa nominal molecular weight limit fractions (dark to light in color), respectively. 87
- Fig. 3-4** Titration data points and their “best fit” *Q* vs. pH model curves of gamma-irradiated (0, 1, 5, 10, 50, 100 kGy) HA and its molecular weight fractions. *Q* denotes the organic charge density. Here, UF₁, UF₂, UF₃, and UF₄ denote the >100, 50–100, 10–50, and <10 kDa nominal molecular weight limit fractions, respectively..... 88
- Fig. 3-5** Distributions of Cs(I), Sr(II), and Eu(III) in the molecular weight fractions of the metal–humic acid systems (pH of 8 and ionic strength of 0.05 mol/dm³). Here, UF₁, UF₂, UF₃, and UF₄ denote the >100, 50–100, 10–50, and <10 kDa nominal molecular weight limit fractions (dark to light in color), respectively..... 92
- Fig. 4-1** (a) Geological map of the Horonobe region showing the location of the URL site and boreholes HDB-1 to HDB-11; (b) Diagram of the Horonobe Underground Research Facility. Red-colored shafts and galleries have already been excavated as of April 2015. This layout may be changed depending on the results of further investigation. 105
- Fig. 4-2** Characterization of the rock sample of the Koetoi Formation. a: XRD spectra; b: Micrographs obtained at × 30 and × 400, respectively; c: The charge density of solid surface with pH 116
- Fig. 4-3** Characterization of gamma-irradiated HA solution. (a) total organic carbon content (TOC), (b) functional group content. Error bars represent the standard errors of the mean of triplicate experiments. Curves represent the eye guide..... 117
- Fig. 4-4** Dependence of the sorption coefficient of HA on the sedimentary rock samples on gamma irradiation dose. (a) HA only system; (b) Acid dissociation ratio in HA only system; (c) and (d) Cs–HA and Eu–HA systems. The 0.20 μm pore size filter was used. Curves represent the eye guide. (C_{org})_i = 81.12, 69.85, 60.67, 52.05 mg/dm³ for 0, 10, 50, 100 kGy, respectively; [Cs⁺]_i = 0.97 × 10⁻⁸ mol/dm³, [Eu³⁺]_i = 1.06 × 10⁻⁸ mol/dm³; L/S = 0.5 m³/kg, I = 0.05 mol/dm³ (NaCl), pH = 8 ± 0.3..... 119
- Fig. 4-5** Dependence of sorption coefficient of Cs⁺ (a) and Eu³⁺ (b) on the sedimentary rock

samples on gamma irradiation dose. The 0.20 μm pore size filter was used. Curves represent the eye guide. $(C_{\text{org}})_i = 81.12, 69.85, 60.67,$ and 52.05 mg/dm^3 for 0, 10, 50, and 100 kGy, respectively; $[\text{Cs}^+]_i = 0.97 \times 10^{-8} \text{ mol/dm}^3$, $[\text{Eu}^{3+}]_i = 1.06 \times 10^{-8} \text{ mol/dm}^3$; $L/S = 0.5 \text{ m}^3/\text{kg}$, $I = 0.05 \text{ mol/dm}^3$ (NaCl), $\text{pH} = 8 \pm 0.3$ 123

Fig. 4-6 Dependence of α_l and α_s for Cs^+ -HA and Eu^{3+} -HA systems on irradiation dose. Curves represent the eye guide..... 124

List of Tables

Table 1-1	Summary of key radionuclides in HLW and other radionuclides of interest to the present study. Condition: pressurized water reactor (PWR); burnup, 45000 MWd/tU, initial concentration, 4.5 % ^{235}U , cooling 4 years.....	5
Table 1-2	Inventories of spent fuel from nuclear power plants in select countries. CEEA: Canadian Environmental Assessment Agency; CAEA: China Atomic Energy Authority; EC: European Commission; USEIA: U. S. Energy Information Administration.....	6
Table 1-3	Schedules of deep geological repository development in certain countries. The abstract information was obtained from recent public news.....	10
Table 1-4	Nominal dose rates in air calculated for the Mark II 4L-12 SF container (average burnup: 220 MWh/kgU).....	17
Table 1-5	Total organic carbon (TOC) contents (representing natural organic matter content) of Horonobe groundwater collected by drilling	19
Table 2-1	Dependence of appearance and pH of humic substance (HS) solution with dose and dose rate. The values below the pictures show the pH. The supernatant in HA series samples (S-HA and AL-HA) at 500 kGy was used due to the formation of precipitation, while the other irradiated solution was used without any additional treatment.....	61
Table 2-2	Optical indices of S-HA, S-FA and AL-HA obtained using UV–Vis absorbance data at different gamma irradiation doses and dose rates.....	64
Table 2-3	Nonlinear regression fitting of potentiometric titration curves of S-HA, S-FA and AL-HA.....	68
Table 3-1	Optimized fitting parameters for humic acid (HA) samples and their fractions; here, UF ₁₋₄ denote fractions with molecular weights of >100, 50–100, 10–50, and <10 kDa, respectively; Q_1 and Q_2 denote the maximum capacities of –COOH and phenolic –OH groups, respectively; K_1 and K_2 denote the mean acid dissociation constants of –COOH and phenolic –OH, respectively; n_1 and n_2 denote empirical constants reflecting the range of the equilibrium constants for the –COOH and phenolic –OH protonated sites, respectively; S denotes the sum of Q_1 or Q_2 for the UF ₁ –UF ₄ fractions, Q_{tot} denotes the maximum capacity of proton-exchange sites ($= Q_1 + Q_2$), and D denotes the relative content ratio of –COOH to phenolic –OH groups ($= Q_1/Q_2$).....	89

Table 3-2 Complexation affinities of the molecular weight fractions of humic acid for Cs ⁺ , Sr ²⁺ , and Eu ³⁺ ions; here, [M] and <i>c</i> denote the concentration of metal and total organic carbon content, respectively, and UF ₁₋₃ denote fractions with molecular weights of >100, 50–100, and 10–50 kDa, respectively.....	94
Table 4-1 Comparison of the ratio of TOC content, capacity, and metal content in the <10 kDa fraction to the non-filtered fraction.....	111
Table 4-2 Estimated logarithmic concentration (mol/dm ³) of metal species in the <10 kDa fraction (pH 8, / 0.05 mol/dm ³ NaCl).....	113
Table 4-3 Distribution of estimated concentration of metal species in ternary systems (metal ion–HA–rock) by modeling. The subscript “free”, “SO–M”, “MHA” and “SO–MHA” represented the free metal ions, the metal ions sorbed, the metal ions complexed with HA and the metal–HA sorbed, respectively.....	125

List of Abbreviations

IAEA	International Atomic Energy Agency
IEA	International Energy Agency
SF	Spent fuel
FP	Fission products
HLW	High-level nuclear waste
CEAA	Canadian Environmental Assessment Agency
CAEA	China Atomic Energy Authority
EA	European Commission
USEIA	U. S. Energy Information Administration
SKB	Swedish Nuclear Fuel and Waste Management Co.
GDF	Geological disposal facility
NUMO	Nuclear Waste Management Organization of Japan
NWMO	Nuclear Waste Management Organization of Canada
URL	Underground research laboratory
JAEA	Japan Atomic Energy Agency
HS	Humic substance
HA	Humic acid
FA	Fulvic acid
ISE	Ionic selective electrode
TOC	Total organic carbon content
UV–Vis	Ultraviolet–visible spectroscopy
NMR	Nuclear magnetic resonance
ICP-MS	Inductively coupled plasma mass spectrometry
MHHM	Modified Henderson–Hasselbalch model
XRD	X-ray powder diffraction
SEM	Scanning electron microscopy
BET	Brunauer–Emmett–Teller
EDX	Energy-dispersive X-ray
PZC	Point of zero charge

Chapter 1 Introduction

1.1 Nuclear energy

Global warming induced by greenhouse gases is known to cause the frequent occurrence of extreme disasters worldwide, such as melting glaciers, expanding deserts, melting permafrost, glacial retreat, sea ice loss, intense storms, and species extinction. The release of greenhouse gases is attracting attention, particularly with respect to CO₂. More than 200 countries have adopted the United Nations Framework Convention on Climate Change (1992) [1], the Kyoto Protocol (1997) [2], and the Paris Agreement (2015) [3] to address global-warming-related issues. In these frameworks, the committed states must regularly reduce greenhouse gas emissions to restrict the rise in mean global temperature to below 2 °C (3.6 °F) above pre-industrial levels. For example, China, which is the world's largest CO₂ emitter (27 % of global emissions), has made commitments to progressively reduce CO₂ emissions before 2030 after their peak and to achieve carbon neutrality by 2060 [4]. According to a report from the U.S. Environmental Protection Agency, electricity production was the second largest share of greenhouse gas emissions in 2019. Approximately 62 % of the electricity was derived from burning fossil fuels—mostly coal and natural gas—which produced over 25 % of global greenhouse gases [5]. Moreover, the use of electricity is expected to significantly increase with time owing to developments in economic activities, technology, and daily life. Considering the limitations of traditional fossil-fuel-based power stations, the development of sustainable, carbon-free, and environmentally friendly energy is imperative as a critical countermeasure to global warming. Nuclear power is currently recognized as the only well-established large-scale emission-free power source that can satisfy the increasing demand for electricity for ensuring energy security and mitigating global warming [6].

Overall, 442 nuclear power plants are in operation globally across 32 countries [7]. The electricity from nuclear power plants has provided approximately one-tenth of the total electricity production in 2020, which is expected to dramatically increase to one-quarter of the global electricity generated in 30 years [8]. According to data from the International Atomic Energy Agency (IAEA), nuclear power currently provides 19 %, 72 %, 40 %, 18 %, 6.2 %, and 4.2 % of the total electricity generated in the US, France, Sweden, Russia, Japan, and China, respectively [9]. Moreover, countries such as China, India, Japan, Pakistan, the Russian Federation, and the Republic of Korea have announced plans to significantly expand nuclear energy production. For example, a report from the International Energy Agency (IEA) notes that China has established the largest nuclear power capacity since 2012; this has increased by 85 % up to 2019, resulting in the generation of 2011 GWe of power, which is approximately a quarter of the increasing global nuclear power capacity [10]. In addition, Argentina, France, South Africa, Ukraine, and the USA have also expressed an intention to expand their existing programs [11]. For example, the Nuclear Regulatory Commission (USA) has approved 41 uprates of existing plants over the last decade (from August 2010 to January 2021), totaling over 2285 MWe [12].

Nuclear power generation has successively increased for seven years from 2011 [13], and almost reached the record high that was set in 2006, reflecting the rebuilding of public confidence in nuclear power after the Fukushima Daiichi nuclear disaster [8]. The World Energy Outlook 2020 report released by IEA had predicted that the nuclear power industry would probably expand significantly by 1610 TWh (60 %) in the 2018–2040 period [14]. However, the nuclear electricity supply slightly decreased in 2020, which is believed to be temporary owing to the COVID-19-induced reduction in electricity demand; the nuclear electricity generation is expected to continuously increase after this crisis [15]. Nevertheless, the safe handling of radioactive nuclear waste generated by nuclear plants remains under

scientific scrutiny owing to the proliferation of new large-scale nuclear plants [16].

1.2 Nuclear wastes

Electricity production from nuclear power primarily involves harnessing the energy released from controlled continuous splitting of atoms of certain elements as thermal energy using either a gas or water, which is subsequently used to produce steam that drives a steam turbine connected to an electricity-producing generator. The basic fuel in the reactor is U, which is typically in an oxide form and arranged in the form of fuel rods. Nuclear fission can be achieved by irradiating samples of heavy nuclides (^{235}U) with slow-moving thermal neutrons; this involves splitting of a large fissile atomic nucleus into two lighter nuclei of uneven mass (known as the fission products), which releases kinetic energy, gamma radiation, and 2.5 free neutrons on average. A portion of these neutrons may be absorbed by other fissile atoms and trigger additional fission events, which release more neutrons; this is known as a chain nuclear reaction [17].

Similar to the waste produced by conventional thermal power stations, which harness the thermal energy released from burning fossil fuels, nuclear reactors also produce waste via the nuclear fission reactions. Typically, one-third of the fuel (40–90 fuel assemblies) is discharged from the reactor as spent fuel (SF) every 12 to 24 months [18]. At least 270000 tons of SF has been produced worldwide based on the estimated current global nuclear energy capacity [19]. Moreover, approximately 12000 tons of additional SF is produced annually via global commercial reactor operation [20]. Countries such as the UK, France, Russia and Japan have a closed nuclear-fuel-cycle policy for reprocessing SF [21]. Reprocessing is required for two main reasons. First, 96 % of the SF mass is U, which mostly includes the original ^{238}U and a small amount of ^{235}U . Although SF reprocessing is expensive, the reprocessed U can be recovered and re-used as fuel, which increases fuel utilization and

conserves uranium resources. Second, reprocessing can significantly decrease the volume of waste that should be treated in the subsequent stages. For example, reprocessing the SF from a typical 1000 MWe large nuclear reactor that produces 25–30 tons of SF annually can reduce the waste volume to only $\sim 3 \text{ m}^2$ per year [19]. The nuclear waste leftover after reprocessing is denoted as high-level waste (HLW), which consists of radioisotopes with medium to long lives generated by fission, such as ^{135}Cs , and traces of the minor actinides generated by neutron capture, such as ^{241}Am and ^{238}Pu . The possible compositions in HLW are summarized in **Table 1-1** [22].

Although the HLW proportion of the total nuclear waste volume is only $\sim 3 \%$, it accounts for over 95 % of the total radioactivity produced during nuclear power generation [23]. Ingestion of these radioisotopes through the food chain, which is known as internal exposure, can be hazardous to human health [24]. Upon internal exposure, alpha particles released by α -radiation bodies (such as isotopes of Am and Cm) or ionizing radiation induced by fission products can damage genetic material, such as DNA. If this damage is not appropriately repaired, cells may die or eventually become cancerous [25]. In addition, accumulation of this radiation in certain organs may occur depending on the type of the radioactive material. For example, the association between radiation exposure induced by a short-lived ^{131}I (and a long-lived ^{129}I) and the occurrence of thyroid cancer has been well documented. An increased risk of thyroid carcinoma was observed as a consequence of fallout from the thermonuclear explosion in the Chernobyl nuclear plant accident in Belarus and Ukraine, especially in children [26]. The ^{137}Cs and the long-lived ^{135}Cs fission products tend to distribute throughout the body upon entry because of their similar properties to that of K. The presence of radioactive Cs in the human body increases the possibility of cancer and tumors. ^{90}Sr can cause bone cancer [27], tissue cancer, and leukemia [28] upon entering the human body owing to its similar properties to those of Ca.

Table 1-1 Summary of key radionuclides in HLW and other radionuclides of interest to the present study [22]. Condition: pressurized water reactor (PWR); burnup, 45000 MWd/tU, initial concentration, 4.5 % ^{235}U , cooling 4 years.

Element	Mass (g)	Isotope	Radioactivity (Bq)	Half live (a)	Decay mode
Cs	3.50E+03	Cs-135	2.34E+15	2.3E+06	β
		Cs-137	4.74E+15	30.07	β, γ
Sr	1.16E+03	Sr-90	3.40E+15	29.12	β
		Eu-152	2.56E+11	13.3	β, γ
Eu	2.09E+02	Eu-154	4.20E+14	8.6	β, γ
		Eu-155	2.11E+14	4.96	β, γ
Np	6.78E+02	Np-237	1.77E+10	2.14E+06	α
		Pu-238	1.50E+04	87.7	α
		Pu-239	1.32E+13	2.41E+04	α
Pu	1.04E+04	Pu-240	2.10E+13	6.57E+03	α
		Pu-241	4.92E+15	14.36	α, β, γ
		Pu-242	8.82E+10	3.76E+05	α
		Am-241	4.10E+13	432	α
Am	4.55E+02	Am-242m	3.71E+11	152	α
		Am-243	9.69E+11	7.37E+03	α
		Cm-243	1.04E+12	28.5	α
Cm	4.06E+01	Cm-244	1.13E+14	18.1	α
		Cm-245	1.20E+10	8.50E+3	α

1.3 Final disposal of nuclear wastes

1.3.1 Concept of deep geological repository

Certain countries have accumulated large inventories of SF via the use of commercial nuclear power plants over decades (**Table 1-2**). It is worth noting that in certain cases, the SF totals include contributions from different types of reactors with varying levels of radioactivity; therefore, the tabulated data might not be directly comparable.

Table 1-2 Inventories of spent fuel from nuclear power plants in select countries [29]. CEAA: Canadian Environmental Assessment Agency; CAEA: China Atomic Energy Authority; EC: European Commission; USEIA: U. S. Energy Information Administration.

Country	Spent fuel inventory (tons)	Inventory date	Source of information
Canada	54,000	Jun., 2016	CEAA
China	4,367	Dec., 2013	CAEA
Finland	1,934	End of 2013	EA
France	14,146	End of 2013	EA
Germany	8,397	End of 2013	EA
Japan	17,838	Jun., 2017	Takubo et al.
Russia	21,362	Jan., 2014	Rosatom et al.
South Korea	14,620	End of 2015	Kang et al.
Sweden	6,296	End of 2013	EC
United Kingdom	5,329	End of 2013	EC
United States	69,682	Dec. 2015	USEIA

The aforementioned nuclear waste is currently in temporary storage, that is, they are typically placed in carefully constructed vats, which are subsequently lowered into cooling water pools (known as SF pits) in the wet storage method [30]. However, the majority of the

cooling pools lack defense-in-depth measures, such as secondary containment, and are vulnerable to loss of cooling; moreover, they lack independent back-up power in several cases, and are thus vulnerable to natural disasters. For example, after an earthquake and tsunami struck a nuclear power plant in Fukushima (Japan, 2011), a water tank that stored radioactive waste was the subject of immense worry. Highly radioactive SF would have been exposed if this pool had dried up, raising the threat of a catastrophic release of radioactive materials into the biosphere [31]. Therefore, the development of safe and efficient strategies for long-term isolation of nuclear waste from the biosphere is critical [32].

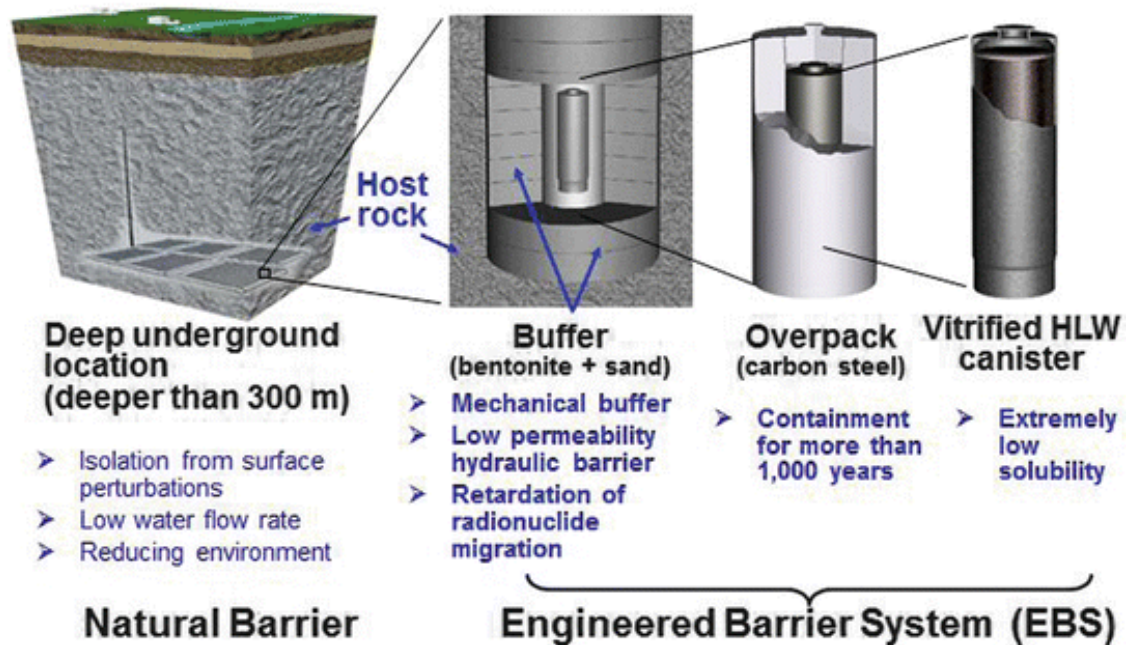


Fig. 1-1 Schematic of HLW disposal in Japan (multi-barrier concept) [33].

Because the high radiotoxicity of hazardous radionuclides presents a danger that can last for thousands of years, dealing with nuclear waste does not just involve preventing harm that can be caused in the present, but also ensuring that the waste is not detrimental to future generations. Various nuclear waste, SF, and HLW disposal strategies, such as ocean disposal, space disposal, and glacier disposal, have been proposed to ensure biosphere safety [34]. One of these approaches—deep geological disposal—involves placing radioactive waste

deep underground to completely isolate it from ecosystems; this is the currently preferred option for long-term waste management [35]. Geological isolation of long-half-life radionuclides has been proven to be an effective method by several natural scenarios. The most convincing example is a scenario that occurred billion years ago in Oklo, in what is now Gabon in West Africa, where several spontaneous natural nuclear reactors operated within a rich vein of uranium ore for approximately 500000 years before ceasing operation. They produced all the radionuclides found in HLW, including over 5 ton of fission products and 1.5 ton of plutonium, all of which remained at the site and eventually decayed into non-radioactive isotopes. Therefore, this case presumably confirms the feasibility and security of adopting deep geological disposal for HLW.

Fig. 1-1 shows the HLW disposal scheme employed in Japan, as proposed by the Nuclear Waste Management Organization of Japan (NUMO). Each geological disposal facility (GDF) consists of multiple barriers that include both natural barriers and engineered barrier systems (EBSs). In an EBS, vitrified HLW form the first barrier; the dissolution rate of vitrified waste, which is incorporated into a borosilicate glass, is extremely low. The second and third barriers are a thick package made of carbon steel and a buffer made of bentonite and sand, respectively [33]. The EBS is generally considered the most important part of the barrier systems for waste containment on the order of hundreds to thousands of years; however, the components may subsequently begin to degrade. Further isolation of HLW is achieved by constructing the facility in rock, termed as host rock, at a depth of several hundred meters; this system is referred to as the natural barrier. The host rock isolates waste from the surface environment, which not only protects the biosphere from the hazardous radionuclides, but also provides a chemically, mechanically, and hydro-geologically stable environment. Moreover, the host rock can actively retard the transport of radionuclides in groundwater through their sorption onto the mineral surface. According to

NUMO, the possible deterioration in containment function would be local; moreover, even if certain safety functions decline, other safety functions can work complementarily to ensure an effective overall containment performance by the multi-barrier system [36].

1.3.2 GDF-related policies and scheduling in various countries

Although the geological disposal of HLW is widely accepted by nuclear industries and regulators globally (e.g., IAEA) to be the appropriate and permanent solution for containing radioactive waste based on economic and safety considerations, no country has established GDFs for storing HLW from commercial nuclear reactors. Because of their historic or anticipated reliance on nuclear energy, several countries have invested significant resources in radioactive waste management programs, and have developed repositories at different paces for SF and/or HLW disposal. In addition, social, economic, political, technical, and geographic considerations influence the scheduling of the radioactive waste management decisions of countries. **Table 1-3** summarizes the current development and planning of HLW disposal in certain countries.

Table 1-3 Schedules of deep geological repository development in certain countries. The abstract information was obtained from recent public news.

Country	Status
Construction underway	
Finland	Construction is in progress. The joint functional test, which will take place in 2023, will test final disposal using the canisters non-containing spent nuclear fuel. Once the joint functional test is complete under the monitor by authorities, the actual final disposal activities will begin around 2025 [37].
Submitted a licensing application to build a repository	
Sweden	An application from Sweden’s radioactive waste management company (SKB) for license to construct was submitted in March 2011. In June 2018, the local municipal council has now approved the planned repository at Forsmark. The final decision to authorize the project will now be made by the Swedish government. SKB plans to start construction of the used fuel repository and the encapsulation plant in the mid-2020s and they will take about ten years to complete [38].
Site selected	
France	France decision drove the establishment of 500 m underground rock laboratory in eastern France situated in clays and known as the Industrial Centre for Geological Storage (Cigéo). The structure will comprise hundreds of storage tunnels covering a total area of 25 km ² and will last for a century. The construction may start in a few years if granted a license [39].
Russia	A one-stop-shop for spent fuel management is one way to describe Russia’s Mining and Chemical Complex (MCC) near Krasnoyarsk, Siberia. The complex is designed to handle spent fuel at its different stages, all at one site. The repurposing of the MCC under this integrated approach began in 2017. The site’s existing personnel and facilities provided the necessary infrastructure to jumpstart the integration. The complex is expected to eventually have an underground research laboratory for high-level waste disposal by 2035 [40].
Active site selection	
Canada	The nonprofit Nuclear Waste Management Organization, which was set up by the Canadian government, is considering two sites for Canada’s first permanent nuclear waste facility—Ignace, Ontario, or South Bruce, which is

within the Great Lakes basin. The organization has said it plans to select one of the two sites in 2023 for a facility that would permanently store high-level nuclear waste deep underground in a network of tunnels and areas to store spent nuclear fuel containers for the long term. However, in September 2021, a resolution was introduced in the House expressing opposition to the site in South Bruce [41].

China The country's strategy for HLW disposal consists of three stages, with stage one: laboratory studies and preliminary site selection, completed in 2020. The second stage, underground in-situ testing, is set to take place from 2021 to 2050, following the construction of the underground research laboratory. The final stage, the construction of the disposal facility, is planned to take place from 2041 to 2050, assuming the in-situ testing confirms the area's suitability [42].

Germany In the fall of 2020, Germany's Federal Company for Radioactive Waste Disposal (BGE) announced that 90 locations have been named in Germany that could safely house containers of radioactive nuclear waste permanently. The company says it needs to find a location by 2031 and hopes to begin storing containers of radioactive waste at the site by 2050 [43].

Japan Japan's 2000 Designated Radioactive Waste Final Disposal Act envisaged a location for the repository would be selected by about 2025, with disposal beginning around a decade later. However, considering the public sentiment against atomic power, the government has scrapped the target date to complete the waste repository after a wholesale review of the nuclear industry [44].

Switzerland In November 2018, the Federal Council decided that five potential sites are being evaluated. Switzerland's national radioactive waste disposal cooperative Nagra expects to submit the general license application for the disposal facilities by 2024. A decision on the approval of the license is expected around 2030 and is subject to an optional national referendum. The repository for LLW/ILW is planned to be in operation by 2050, with the one for HLW planned to be operational ten years later [45].

United Kingdom Three sites in the north of England are being assessed as potential locations for a long-term nuclear waste facility [46].

United States In December 2021, The US Department of Energy (DOE) issued a request for information in the Federal Register, aimed at completing a draft siting process it has been working on since 2015. The move represents a re-start of the federal programmer after plans for a repository at Yucca Mountain dropped in 2009 [47].

1.3.3 Underground research laboratory

Prior to the construction of GDFs, several countries such as Japan, Canada, and France followed the underground research laboratory (URL) program, the aims of which were as follows:

- (1) URL could be used to develop the technology needed for the construction, operation, and closure of a deep geological repository;
- (2) URL could provide access to the geologic environment under realistic repository conditions, to verify the technical reliability of geological disposal through testing and research conducted in actual deep geological environments and monitoring systems;
- (3) Importantly, URL can be used to demonstrate the concepts and technology of radioactive waste disposal to the general public, which is crucial for enhancing social understanding and confidence.

For example, the Japan Atomic Energy Agency (JAEA) operated the Horonobe URL in Hokkaido and the Mizunami URL in Gifu under geological conditions of sedimentary rock and saline water, and crystalline rock and fresh water, respectively [48], since 2005. The French national agency for the management of radioactive waste initiated the first phase of a URL project in 2000, and has operated the Meuse/Haute Marne URL, which is located 500 meters underground in Bure in the Meuse département, since 2007. In 2021, the CAEA (China) announced the construction of the Beishan URL near Jiuquan City in Gansu province [49]. The URL will be situated in granite up to 560 meters below ground level in the Gobi Desert, and is planned to be used to test the suitability of the area for the long-term storage of HLW [50]. The URL, which comprises a spiral ramp and three vertical shafts and horizontal disposal galleries, is estimated to be constructed in seven years at a cost of over 420 million USD. It is designed to operate for 50 years, and an underground repository for

HLW is planned near the URL by 2050 if the research proves successful and the site is found to be suitable [51].

1.4 Short- and long-term evolutions of GDF

As mentioned earlier, deep geological disposal of radioactive nuclear waste is particularly beneficial in terms of the insulation of the waste from the biosphere up to a time when its radiotoxicity will have decayed to levels that cannot be considered hazardous. Therefore, the possible failure of deep geological repositories must be investigated to assess the safety of this nuclear-waste-disposal strategy. From the perspective of time scale, the failures in deep geological disposal can be categorized into initial and long-term versions. Initial failure is mainly induced by defects present in any large assembly of engineering components. For example, dislocations and point defects (vacancies, interstitial atoms, and impurities) can cause microscopic segregation and precipitation phenomena in materials under aging or irradiation. Moreover, certain defects in copper and iron alloys cannot be detected during their manufacturing. These defects and their interactions with each other determine the plastic properties of the packaging material, that is, the possibility of leakage of nuclear waste [52]. In addition, the timeframe of safe isolation of nuclear waste is speculated to be on the order of 10^5 – 10^6 years [53]. Therefore, long-term failure involves large uncertainties of natural disasters in the areas of geological repositories, such as climate change and volcanic activity, and long-term corrosion.

1.4.1 Waste package as an artificial barrier

Waste package is an important component of EBSs used for waste containment. Reports by certain institutions have revealed the presence of defects in the waste package, which can lead to the initial failure of deep geological repositories. The nature, size, and

location of these defects depend on the material and manufacturing technology in question. SKB (Sweden) is particularly concerned with the flaws of closure welds in copper shell packaging. Two ~10-mm-sized defects were identified in tests conducted on the manufacturing of the cast iron insert and the minor defects in the copper shell [54]. The Japan Nuclear Cycle Development Institute (JNC, predecessor of JAEA) suggested that an initial failure of 10^{-3} could be conservatively allowed in the waste package of HLW with respect to all containers that are disposed of [55]. In addition, certain chemical and physical effects can accelerate the initial failure of deep geological repositories, such as (1) heat-induced alterations of the waste package; (2) radiation-induced loss of the mechanical integrity of the waste package; and (3) partial chemical corrosion. These factors can affect the toughness and strength of isolation materials, and increase the probability of nuclear leakage.

1.4.2 Groundwater in deep underground locations

Geological information, such as groundwater conditions, is crucial in the selection of sites for GDFs. For instance, groundwater flow systems in and around the Horonobe URL area have been examined based on the results of groundwater flow analyses (**Fig. 1-2**). These results indicate that the groundwater flow systems in the URL-containing area are governed by the undulating topography, and can be divided into local and regional flow systems, depending on depth. The boundary between the two systems is located at a depth of approximately 400 m below ground level, and the groundwater flow near the URL (drifts located at a depth of approximately 500 m) is highly likely to be governed primarily by the regional flow system [56]. Matsumoto et al. estimated the groundwater velocity in a 300-m-underground Horonobe area to be 0.37 m/year by conducting a single-well push-pull (SWPP) test [57]. Although the GDF sites must avoid underground water intrusion as much

as possible, the groundwater is expected to inevitably intrude into repositories upon the early and long-term failure of the multi-barrier system owing to the alteration and degradation. However, the exact period of this event cannot be predicted with accuracy owing to the uncertainties associated with the long timescale.

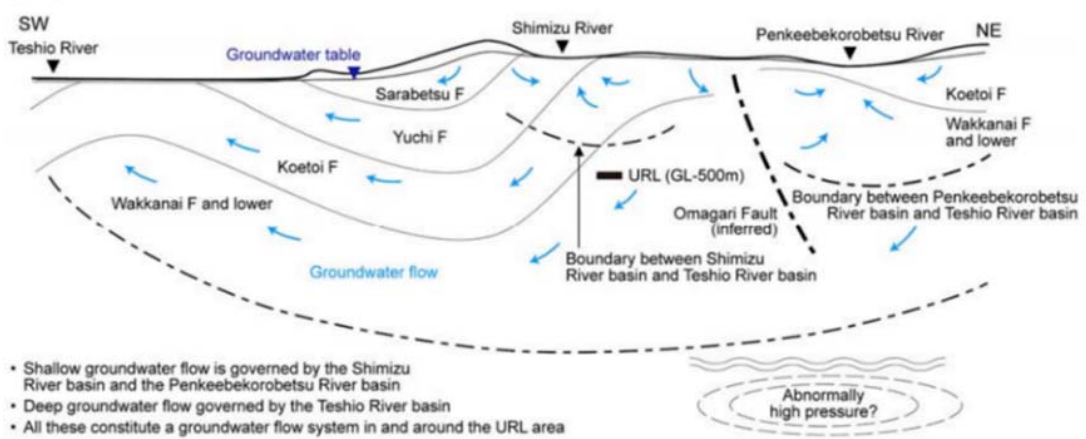


Fig. 1-2 Conceptualization of groundwater flow in and around Horonobe URL area [56].

1.4.3 Gamma irradiation around waste packages

The gamma irradiation effects in nuclear waste glasses are induced by self-radiation arising from the radioactive decay of radioactive nuclei, such as ^{137}Cs . Gamma rays are not particles but a high-energy form of electromagnetic radiation. Gamma rays have tremendous penetration power and require several inches of dense material (such as lead) to shield them. The gamma-ray field can be characterized by the exposure rate, which is linearly proportional to the radioactivity of a point source and inversely proportional to the square of the distance, as follows:

$$F = \Gamma \frac{\alpha}{r^2} \quad (1-1)$$

where F is the exposure rate (R/h), r is the distance (cm), α is the source activity (mCi), and Γ is the exposure rate constant, which is dependent on the particular radionuclide used as the gamma-ray source. For example, the exposure rate constant for ^{137}Cs , which is the main

contributor to the gamma irradiation in nuclear waste, is $3.40 \text{ R}\cdot\text{cm}^2/\text{h}\cdot\text{mCi}$. The ionizing radiation dose rate can be converted into the radiation absorbed dose rate as follows: $1 \text{ R/h} = 0.01 \text{ Gy/h}$ [58].

The dose rate in the vicinity of the waste package has been evaluated using various approaches. MicroShield (Grove Software Inc.) is a comprehensive photon/gamma-ray shielding and dose assessment program that is widely used for designing shields and estimating the source strength from radiation measurements [59]. It includes a built-in library that provides standard reference values for various key inputs, such as the radionuclide data, material attenuation and buildup factors, and dose conversion factors. MicroShield uses the point-kernel method as a numerical approach, in which a volume source is treated as a number of point sources. The direct photon flux from each point source to the dose point is analytically calculated, including attenuation and buildup along each path [60]. The 37-element CANDU “long” bundle is used as the fuel bundle for components such as ^{137}Cs , ^{140}Ba , ^{144}Ce , ^{106}Ru , ^{90}Sr , ^{113}Sn , and ^{103}Rn . Moreover, the ICRP-107 library (ICRP, 2008) is used for nuclide half-lives and branching ratios [61]. The total gamma photon spectra are divided into 18 discrete energy groups with mean energies in the range of 0.01–5.50 MeV. Each energy group of the photons is separately executed and subsequently combined to reflect the total dose rate of the gamma irradiation.

For example, the Nuclear Waste Management Organization of Canada (NWMO) used MicroShield v9.05 software to perform modelling and calculation of the gamma irradiation dose rate inside and outside Mark II 4L-12, which was selected as the fuel container [62]. The detailed dimensions defined of Mark II 4L-12, including gross cavity volume and module volume have been described in a previous report [63]. The nominal dose rates as a function of cooling time are listed in **Table 1-4**. Although these values show a clear intensity decay in the first 500 years, the gamma irradiation dose rate is noticeably high and

cannot be neglected. SKB proposed that the radiation at the outer surface of the container can be expected to be ~0.5 Gy/h at the early stage of disposal after closing the repository [64]. It is worth noting that the aforementioned dose rates were estimated assuming SF as the nuclear waste instead of HLW.

Table 1-4 Nominal dose rates in air calculated for the Mark II 4L-12 SF container (average burnup: 220 MWh/kgU) [63].

Gamma irradiation dose rate (Gy/h)					
Cooling time (years)	10	20	50	100	200
Fuel surface	96.8	65.3	30.6	9.55	0.949
Container surface	5.08	3.20	1.43	0.45	4.40E-2
Cooling time (years)	500	1000	10 ⁴	10 ⁵	10 ⁶
Fuel surface	5.56E-3	3.38E-3	2.41E-3	3.38E-3	4.23E-3
Container surface	1.53E-4	1.04E-4	1.20E-4	2.72E-4	4.07E-4

In addition, the JNC calculated the irradiation dose at the surface of an HLW overpack using a three-dimensional model and the MCNP-4A radiation transport analysis code based on the Monte Carlo method, which was developed by the Los Alamos National Laboratory (LANL; USA) [55]. The output of ORIGEN-2 was utilized for the radiation source term. The gamma-ray sources were assumed to be generated by neutron radiation and the accompanying decay of fission products. The following analytical conditions were used to assess the effects on corrosion: burn-up, 45,000 MWd/tU; initial enrichment, 4.5 %; buffer composition, 70 wt.% bentonite and 30 wt.% silica sand. The degree of saturation of the buffer was assumed to be 100 % to ensure maximum contribution from the radiolysis of water. The surface dose rate of the HLW package in the repository was estimated to be over

0.1 kGy/h, even after 50 years of cooling [55]. For instance, the duration of radiation exposure equivalent to a gamma dose of 100 kGy near-by the HLW waste packages will be about one month.

1.4.4 Leaching of radionuclides in vitrified waste

Upon intrusion of groundwater into the GDFs, radionuclides can leak from the carbon or stainless-steel packages after long-term erosion, contaminate the natural groundwater system, and finally enter the human biosphere. Yanagisawa and Sakai investigated the leaching behavior of simulated nuclear waste glass under saturated vapor pressure in groundwater, and determined that certain elements readily leached out with increasing rates, as follows: $B < Na < Mo \text{ (as } MoO_4^{2-}) < Li < K < Si < Cs$ [65]. Vernaz and Dussosoy summarized the corrosion mechanisms of nuclear waste glass, and suggested that after an initial glass hydration step, a thin reaction zone is created, within which an exchange reaction of H^+ with alkali metal inter-diffusion profile occurs. Subsequently, the hydrated silicate network congruently dissolves, hydrating all the glass elements [66]. It is worth noting that the dissolution of radionuclides by groundwater was not included in the research scope of this study.

1.5 Humic substance

1.5.1 Natural organic matter in areas of deep geological waste repositories

Natural organic matter (NOM) is a complex matrix of organic materials that is abundant and ubiquitous in the environment, and would be even present in deep underground waters where a certain amount of radioactive waste disposed in the future. Because organic ligands are known to affect the migration of radionuclides, NOM in groundwater is crucial for investigating geological settings and hydraulic conditions. Data related to groundwater

components have been acquired primarily through borehole investigations. For example, the Horonobe URL has collected data using groundwater from an existing borehole (HDB 9-11) since 2004, and the determined total organic carbon (TOC) contents (representing NOM concentration) of the groundwater are summarized in **Table 1-5**. Terashima et al. also collected groundwater samples at depths of 140–350 m in the Horonobe area, and the analytical results showed that the NOM concentration varied from 7.8 to 23.5 mg/dm³ [67]. In addition, Horonobe reports (JAEA-Research-2010-035) also determined a slowly increasing concentration of the organics with depth [68].

Table 1-5 Total organic carbon (TOC) contents (representing natural organic matter content) of Horonobe groundwater collected by drilling [68].

Borehole	HDB-9		HDB-10		HDB-11	
Mid-depth (m)	54.05	237.20	50.61	457.87	204.03	625.03
TOC (mg/dm ³)	2	9	36	20	19	31

1.5.2 Classification and chemical properties of HSs

In one protocol, the water is continuously filtered (<0.45 μm), its pH adjusted to 2 using HCl, and the product is passed through the DAX-8 resin according to the definition of HSs in NOM. Herein, the organic components sorbed on the resin are considered as HSs [69]. Generally, HSs constitute a major proportion (50–90 %) of NOM from environmental waters (in terms of TOC). HSs are the refractory, dark-colored, and heterogeneous organic compounds produced as byproducts of the chemical decomposition and condensation of living beings, such as animals, plants, and microorganisms. According to the classical solubility-related definition of HSs [70], that is, the degree of dissolution in water at different pH values, heterogeneous HSs are categorized into three fractions, as follows:

- (1) Humic acid (HA) is the fraction that is insoluble in solutions with pH below 1 but soluble at higher values of pH.
- (2) Fulvic acid (FA) is the fraction that is soluble at all pH values.
- (3) Humin is the fraction that is insoluble in water at all pH values.

The properties of HA, FA, and humin are briefly described in **Fig. 1-3a**. It is worth noting that the separation of HSs into three fractions does not indicate the existence of three distinct types of organic molecules [71].

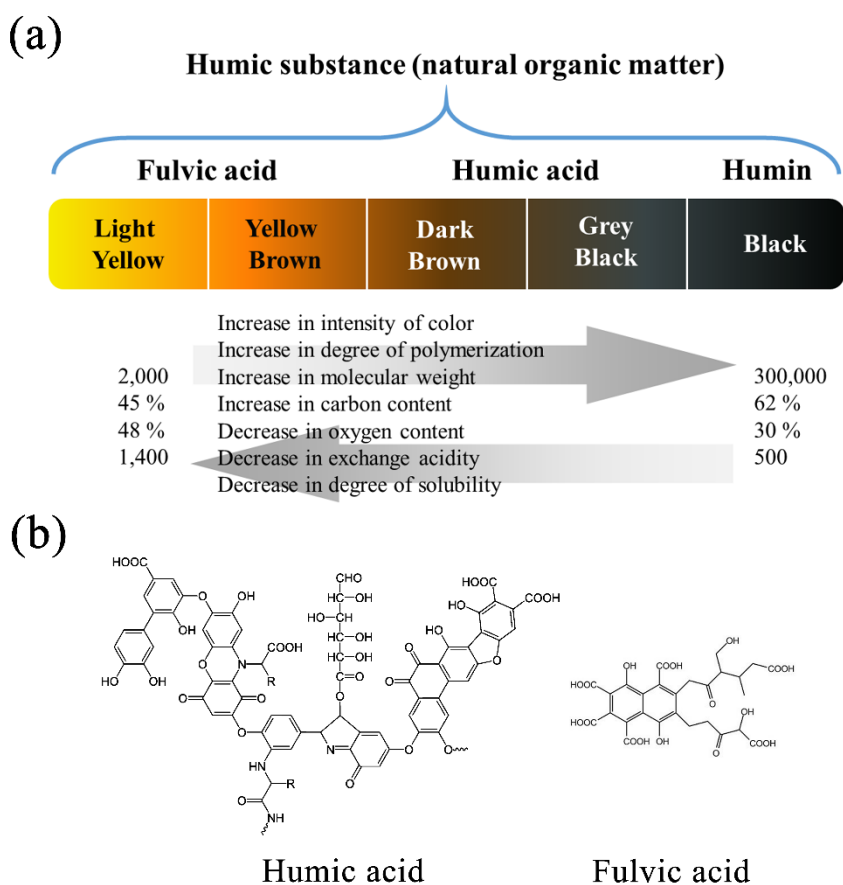


Fig. 1-3 (a) Classification of humic substances (HSs), and the differences in physiochemical properties [72]; **(b)** Hypothetical structures of humic acid (HA) [73] and fulvic acid (FA) [74]. It is worth noting that HA and FA are not pure substances, but mixtures of various substances with similar chemical properties.

HSs are inherently natural organic carbon-chain heterogeneous mixtures that

mainly consist of C, O, H, N, and S. The average elemental composition of HS extracted from different sources is approximately 50 % C, 35 % O, and 5 % H, with the remaining percentage distributed between N and S [75]. The acidic functional groups of HA can vary according to geographical origin, age, climate, and biological conditions. In general, HAs are mainly composed of aliphatic, aromatic, hydroxyl, carbonyl, carboxylic acid, phenolic, enolic, quinone, and ether functional groups, and can include sugars and peptides, according to evidence obtained by infrared radiation (IR) spectroscopy and nuclear magnetic resonance (NMR) spectroscopy [76]. Among these, the -COOH and phenolic -OH groups are known to be the most abundant reactive functional groups, and are responsible for the weakly acidic behavior of HSs. The acidic functional groups are also responsible for the ability of HSs to bind with cationic metals and form complexes.

Fig. 1-3b shows the hypothetical model structures of HA and FA. However, the chemical structures of HSs remain controversial owing to their heterogeneity and complexity [77]. HA is believed to comprise randomly coiled macromolecules consisting of carbon chains and carbon rings, according to the early concepts of polymers. The evidence supporting the polymeric structure of HSs includes the high molecular weight of soil-based HS (average values of 53000, 25000 and 77000 Da) determined by sedimentation velocity ultracentrifugation [78, 79]. However, recent information gathered using spectroscopic, microscopic, pyrolysis, and soft-ionization techniques does not corroborate the macromolecular structure of HSs. The current understanding views HSs not as high-molecular-weight macromolecules but as heterogeneous and relatively small molecular components of the soil organic matter auto-assembled in supramolecular associations by multiple weak interactions, such as hydrogen bonds and van der Waals forces [80]. The stabilization of their structure has been primarily attributed to the hydrogen bonds and the intra- or intermolecular interactions. Simpson examined HS solutions by two-dimensional

diffusion-ordered spectroscopy (DOSY), and found that low- and high-concentration HA solutions (5 mg/dm³ and 100 mg/dm³, respectively) contained aggregates with diffusivities corresponding to average molecular masses of >66000 Da and 2500–6100 Da, respectively [81]. In addition, HS molecules volatilized by electrospray ionization mass spectrometry (ESI-MS) have average molecular mass distributions of approximately 1000 [82] or 2000 Da [83]. Laser desorption ionization (LDI) provided mass/charge distributions with number-weighted averages closer to 500 Da [84]. These ESI- and LDI-MS average masses are considerably lower than those measured by traditional methods such as ultracentrifugation. Several independent analytical techniques have consistently indicated the presence of relatively small, independent moieties in HSs, thereby corroborating the definition of these organic materials as collections of diverse low-molecular-mass molecules.

1.5.3 Complexation of metal ions with HSs

The interactions between HSs and radionuclides have been considered in the safety assessment of nuclear waste disposal, which is crucial for the prediction of radionuclide migration. Since 1985, the OECD Nuclear Energy Agency (NEA) has operated the thermochemical database (TDB) project with participating countries such as Canada, France, Japan, the UK, and the USA [85]. The TDB was setup to collect and arrange high-quality, traceable, internally consistent, and internationally recognized chemical thermodynamic data of selected elements relevant to the safety of radioactive waste repositories, and provide appropriate data for geochemical modelling, such as solubility and speciation calculations, and predicting radionuclide migration from near-field into the far-field [86]. A crucial goal of the TDB project involves obtaining thermodynamic data on the interactions of organic ligands with metal ions, primarily the conditional stability constants, that is, the apparent formation constant ($\log \beta_{\text{app}}$).

Various techniques have been adopted to determine the complexation stability constant of HSs with metal ions. For example, fluorescence titration (FT) is a simple, powerful, sensitive, and nondestructive technique that enables investigation of the extent and mechanism of the HS–metal-ion interactions. The complexation of HS with metal ions causes a marked decrease in the fluorescence intensity; essentially, a linear relationship exists between the fraction of the total bound ligands and the fluorescence intensity, which involves a static quenching mechanism. Plaza et al. investigated the complexation constant of Cu(II) with HSs by FT (HA, 15 mg/dm³; pH, 6; and *I*, 0.1 mol/dm³ NaCl). A simple 1:1 stoichiometry was assumed for the Cu–ligand binding, and the stability constants (log *K*) of the Cu–HA complexes were estimated to be 5.14–5.36. In addition, regression analysis showed that the complexing capacity of Cu and the stability constant were not significantly correlated with the C/N, C/H, and O/C atomic ratios in the HA molecules [87].

The ion-selective electrode (ISE) method is a conventional approach for directly and readily measuring the activity of free (non-complexed) metal ions. Sasaki et al. investigated a homemade Eu-ISE consisting of bis(diphenylphosphoryl) methane as an ionosphere, which exhibited an adequate Nernstian response to free Eu³⁺ in test solutions. The HA extracted from Elliott soil was used to determine the formation constants of Eu³⁺ with HA (~6.0) using an ISE. Additionally, the Eu ions were proposed to preferentially interact with the stronger coordination sites in the presence of excess complexation sites in HA, resulting in an increase in the formation constant. Moreover, the weaker coordination sites were found to be useful for complexation under conditions involving insufficient complexation sites [88].

Sasaki et al. determined the formation constants of HSs with Am(IV) and Pu(IV) using a solvent extraction method. The organic phase of xylene containing the β -diketone extractant of 4, 4, 4-trifluoro-1-(2-thienyl)-1, 3-butanedione was adopted as the extractant. The log β_{app} values of the Th(IV)–HA complexes were approximately 20 and increased with

increasing pH. Moreover, the $\log \beta_{\text{app}}$ values of Pu–HA complexes were 12.9–14.3 at a pH of 4. The linear correlation between the H^+ and Na^+ concentrations and the formation constants was observed to correspond to the equilibrium reaction with the tetravalent metal ions. However, the concentrations of HA and M^{4+} ions did not show significant dependence, suggesting the existence of excessive functional groups that could strongly coordinate with the metal ions in the systems [89].

Sakuragi et al. investigated the distribution ratios of Am(III)–humate species to free Am(III) ions ($D = [\text{Am}]_{\text{Am-HA}}/[\text{Am}]_{\text{free}}$) in the pH range of 4–10 using the cation-exchange equilibrium method. The D values were found to be insensitive to an increase in pH ($\log D = 2.6\text{--}2.8$), indicating the formation of mixed hydroxo–humate complexes. The obtained D values were larger than those estimated using the stability constants of ternary complexations determined by spectroscopic analysis (1.4–2.1), indicating that the stability constants for ternary hydroxo complexation evaluated by spectroscopic analysis were underestimated [90].

The mechanism of HS–metal-ion complexation has received extensive scientific attention. As described earlier, the abundant functional groups, principally –COOH and phenolic –OH groups, result in the strong bonding of metal ions onto the surface or into the structure of HA molecules via complexation; this leads to the formation of metal–HA complexes via neutral or negative-surface-charge complexation reactions, which are also known as organic metal colloids [91, 92]. For example, Prado et al. studied the interactions of Cu^{2+} and Zn^{2+} ions with HA extracted from Brazilian peat soil. Infrared spectroscopy showed that the intensity of the peak corresponding to the stretching frequency of C=O decreased following complexation formation, indicating that the interaction with metals primarily occurred on the carboxylic acid groups of HA; no other differences were observed in the IR spectra. The changes in half-wave potentials indicated the formation of chemical bonds between metal ions and HA. The entropy determined by kinetic thermal analysis

indicated that the stability of HA bonded to the metal ions increased compared to that of HA alone [93].

Moreover, lanthanide ion probe spectroscopy (LIPS) has been adopted to examine changes in the fluorescence lifetime of the Eu probe metal as it binds to HSs. The coordination number of HSs bound to Eu^{3+} ions can be calculated according to the change in fluorescence data (616 nm, corresponding to the hypersensitive emission band). Thomason et al. revealed the existence of four different types of $-\text{COOH}$ sites—mono-, di-, tri-, and tetra-dentate—which bond with the probe metal as a function of metal loading. Calculations from this experiment suggested that the tetra-dentate complexes exhibited the strongest complex binding [94].

Schmeide et al. investigated the $\text{U(VI)}-\text{HS}$ complex structure at a pH of 2. A chemically modified HS was used to block phenolic $-\text{OH}$ groups to evaluate the effects of $-\text{COOH}$ and phenolic $-\text{OH}$ groups on the $\text{U}-\text{HA}$ complexation, in which the blocking of the phenolic $-\text{OH}$ groups in the modified HA was verified by Fourier transform infrared (FT-IR) spectroscopy. Extended X-ray absorption fine structure (EXAFS) spectroscopy was used to determine structural parameters of the near-neighbor surrounding of U(VI) complexed by HA. The results indicated that the blocking of the phenolic $-\text{OH}$ groups of HA did not alter the near-neighbor surrounding of U(VI) in the metal-HA complexes, confirming that the $-\text{COOH}$ in HA was primarily responsible for binding with U(VI) , and that the contribution of the phenolic $-\text{OH}$ was insignificant under the investigated experimental conditions. In addition, the $-\text{COOH}$ was found to primarily act as monodentate ligands to the U ions [95].

Geckeis et al. studied the natural association nature of a metal complexed with HS. Colloidal characterization by size-exclusion chromatography (SEC) and flow field-flow fractionation (FFFF) indicated that natural colloid-borne elements (such as rare-earth elements, Th, and U) were predominantly found in large colloids of size >15 nm. The larger

size of the metal-loaded colloids compared to that of HS alone suggested that the polyvalent metal ion binding in the HS was associated with polynucleation and the cation metal bridge. Moreover, the dissociation of the metal–HA complexes was investigated by adding a chelating cation exchanger resin. Radiotracer experiments revealed that equilibrium with isotopic Eu was not attained within a period of more than 100 days, indicating irreversible binding of at least a portion of the colloid-borne Eu ions. The possible metal–HA complexation was proposed to involve rapid reaction of the metal ions with the HS in the initial sites, and subsequent migration of the metal ions to stronger binding sites or to the interior sites of the coiled or agglomerated macromolecular structure of the HS [96].

1.5.4 Size distribution of metal–HA complexes

As described earlier, metal ions can complex with HSs and form organic colloids or pseudo colloids. The molecular weight of these organic metal-loaded colloids has been found to strongly relate to their environmental behavior (e.g., transport and retention) in groundwater during migration processes [97]. Generally, the colloids in the groundwater are fractionated by molecular weight (and size) when passing through the barrier materials, such as the host rock. During this filtration, the low-molecular-weight components are typically expected to be more mobile because the advection of high-molecular-weight components requires large fracture apertures. In addition, the dispersion coefficient of radionuclide colloids also depends on their molecular weight [98]. The empirical correlation between the diffusion coefficient (D) and the molecular weight (M), also known as the Mark–Houwink–Sakurada equation, is expressed as follows:

$$D = kM^\alpha, \quad (1-2)$$

where k and α are empirical constants. Therefore, the chemical properties of the molecular-

weight-dependent fractions of HS molecules and the molecular-weight-dependent complexation ability of the metal ions have also attracted considerable attention.

The molecular weights of metal–HA complexes have also been investigated. Nagao et al. studied the effect of size-separated HA fractions on the complexation properties of trivalent actinides by gel chromatography. The dominant size fractions of Am(III) were 3.05–450 nm in the presence of HA, while the percentage of Am(III) with a molecular size fraction less than 10 kDa was only 3 %. A positive correlation was observed between the percentage of Am and TOC in the fraction of more than 10 kDa. The lower-molecular-size fractions were found to exhibit an inferior complexation ability and a less competitive reaction than those of the high-molecular-size fractions. The complexation ability in each size fraction depends on the percentage of molecular size fractions of HA. Moreover, the molecular size distribution of HA is a factor that controls the complexation properties of metal ions with HA [99].

Bolea et al. investigated the possible interactions of approximately 30 elements with different size fractions of HSs using three common separation techniques: ultrafiltration, high-performance SEC (HPSEC), and asymmetrical FFFF (AsFFFF). The elements were classified into three main groups with regard to their interactions with the HSs. The first group primarily comprised monovalent alkaline metal ions and anionic species, such as B, W, and Mo, existing as oxyanions that were not significantly associated with the HSs. The second group consisted of elements that were at least partly associated with a smaller HS size fraction (such as Ni, Cu, Cr, and Co). The third group primarily comprised tri- and tetravalent metal ions, such as Al, Fe, lanthanides, Sn, and Th, which were considerably associated with larger HS fractions. The three separation techniques provided a fairly consistent size classification for most metal ions, although slight disagreements were observed [100].

1.6 Sorption behavior of radionuclides

1.6.1 Sorption of metal ions in GDF

As described in the introduction in **Section 1.4**, radionuclides can be leached into groundwater and subsequently migrate to the biosphere upon failure of the deep geological repositories. Generally, the radionuclides in the waste would have to penetrate various barrier systems to migrate into the natural environment, which can presumably be retarded by sorption processes. Sedimentary formations are regarded as a candidate for host rock around GDFs, and have been employed by several countries such as Japan, Canada, France, and Germany [101]. Sedimentary rock consists of clay minerals, quartz, feldspar, mica, and other materials. Clay minerals, such as illite and smectite, possess permanent net negative charges owing to isomorphic substitutions within the aluminosilicate lattice. Unlike the clay minerals, other oxide minerals, such as quartz and goethite, do not have any permanently charged sites. Instead, their surface charge is pH dependent, and protonates or deprotonates according to the solution pH [102, 103]. When nuclides migrate with the groundwater in the vicinity of waste repositories, the various positively charged metal ions are readily sorbed onto the host rock in the GDF area by various mechanisms that are dependent on the type of metal ions and the solution conditions. The sorption of radionuclides delays their transport by groundwater. For example, the sorption of Cs^+ ions onto sedimentary rock is controlled by the cation-exchange mechanism that specifically occurs in clay minerals, e.g., the highly selective frayed edge site (FES) in illite and the interlayer sites in smectite [104]. Under moderate conditions (low ionic strength, pH of 4–10), Sr^{2+} ions are known to sorb on the permanently charged surface sites of clay and the temporarily charged sites of oxide minerals via simple electrostatic interactions or formation of outer-sphere complexes. However, Fuller et al. suggested that the dominant mechanism of Sr sorption at a solution pH of 12–

14 involves the formation of inner-sphere complexes of Sr ions with the hanging hydroxyl groups at the edge of the clay, the surface hydroxyls of oxides, and the interlayer of illite [105]. Generally, Eu ions are selected as a chemical analog for trivalent actinides, such as Am and Cm. Analysis of the sorption of Eu^{3+} on Na-montmorillonite by time-resolved laser fluorescence spectroscopy (TRLFS) suggested that the cation-exchange reaction was a crucial sorption processes under conditions of $\text{pH} = 4\text{--}7$ and $I = 0.01 \text{ mol/dm}^3 \text{ NaNO}_3$, whereas the surface complexation of Eu^{3+} and its positively charged hydroxides, such as $\text{Eu}(\text{OH})^{2+}$, was mainly predominant under alkaline conditions, instead of the cation-exchange reaction [106]. In addition, the sorption of Eu on oxide minerals, such as alumina, silica, and hematite, has been observed because of their strong pH-dependent surface charge [107]. Therefore, the apparent mobility of radionuclides released from HLW repositories is expected to be significantly affected by the sorption processes on the host-rock–water interface [108, 109], which can delay the transport of nuclides [110]. The sorption of radionuclides in groundwater must be further examined to comprehensively elucidate radionuclide migration and to estimate the risks.

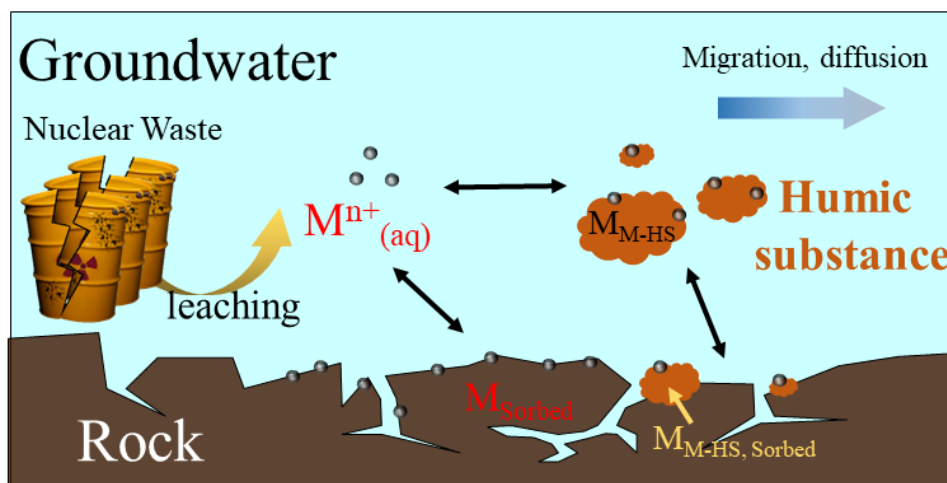


Fig. 1-4 Typical chemical interactions (sorption and complexation) of radionuclides (M) in a groundwater system.

HS molecules that are present in deep groundwater can react with metal ions to form metal–HS complexes. The formation of negatively charged metal-loaded organic colloids has been recently found to considerably disturb the sorption of metal ions [111, 112], as shown in **Fig. 1-4**. The sorption of metal ions in the presence of HSs has recently been found to be crucial in the modelling of radionuclide migration. Krepelova et al. investigated U(VI) sorption onto kaolinite in the absence and presence of HA by conducting batch experiments. The sorption of U(VI) was found to be enhanced by the addition of HA under acidic conditions compared to that of the HA-free system because of the positive surface charge of kaolinite under acidic conditions and the formation of additional negative binding sites for U(VI) via the sorption of HA onto kaolinite. In contrast, the sorption of U(VI) in the presence of HA at $\text{pH} > 6$ was inhibited compared to that without HA. The sorption percentage of U(VI) at a pH of 7 decreased from 95 % to 85 % and 60 % at HA contents of 0, 10, and 50 mg/dm^3 , respectively [113]. Seida et al. studied the sorption of Eu(III) onto sedimentary rock in the presence of HA. The sedimentary rock and HA were collected from a 500-m-deep rock and groundwater at Horonobe URL sites, respectively. The results indicated that the sorption of Eu(III) was a function of the HA concentration at a tested pH of 8.2 in a batch experiment. The sorption ability of Eu(III) on the rock reduced with increasing HA concentration owing to the Eu-ion–HA complex formation [114]. Therefore, the understanding of metal sorption in the presence of HA has been indispensable to investigating the migration behavior of nuclides.

The sorption coefficients of certain metal ions have been recently collected by several groups and organizations to establish a sorption database for reliably predicting radionuclide migration and assessing the safety performance of GDFs. For example, JAEA has developed a Thermodynamic, Sorption & Diffusion Database (JAEA-SDB) that compiles sorption coefficient data of metal ions with respect to buffer material and rock. The database was first

developed as an important basis for the H12 report on HLW disposal, and can be accessed through the internet. The JAEA has continued to improve and update the database in view of potential future data needs, with a focus on assuring the desired quality level and testing the usefulness of the database for possible applications to multi-parameter-dependent settings [115].

1.6.2 Impact of gamma irradiation on radionuclide sorption

Gamma rays are ionizing radiation. When gamma rays are absorbed by water, their high energy can rupture water molecules and form highly reactive free-radical products, such as HO·, H·, and H₂O₂ [116]. The framework in which water radiolysis occurs is experimentally and theoretically well understood [117], as illustrated in **Fig. 1-6** [118]. These radical products significantly react with organic matter and affect their chemical properties.

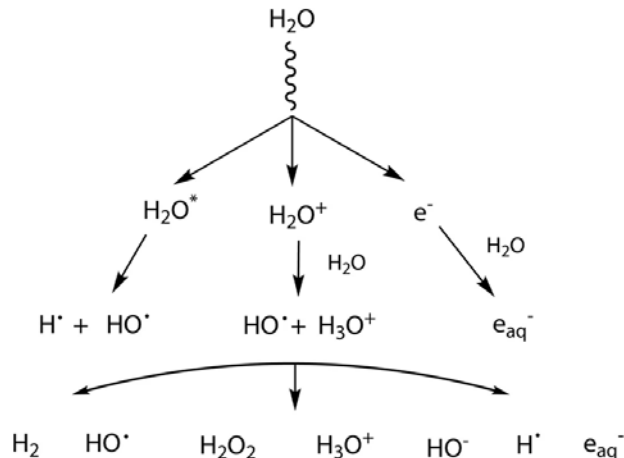


Fig. 1-5 Primary products from gamma-irradiation-induced radiolysis of water

Lee et al. investigated the effects of gamma irradiation on the physiochemical properties of alginate, including viscosity, molecular weight, and color. The molecular weight of raw alginate decreased from 300 to 25 kDa upon irradiation of 100 kGy. The irradiation-induced degradation of alginate was proposed to result from the oxidative

degradation initiated by HO· free radicals. The viscosity of irradiated alginate solution reached a near minimum at a dose of as low as 10 kGy. No appreciable color changes were observed in the samples irradiated up to 100 kGy; however, intense browning occurred at doses beyond 200 kGy [119].

Liu et al. studied the effects of gamma irradiation on the microstructure, thermal stability, and degradation of cellulose. FT-IR spectroscopy and electron paramagnetic resonance (EPR) analysis showed that the gamma irradiation destroyed the glycosidic bonds and inter- and intra-molecular hydrogen bonds in cellulose, generating reductive carbonyl groups. The gamma irradiation was found to damage the crystalline microstructure and surface morphology of cellulose, and the irradiation-derived degradation components, including glucose, xylose, arabinose, and fructose, were analyzed [120].

As mentioned in **Section 1.4.3**, a long-term high-penetration gamma irradiation field can be generated upon damage of well-designed barriers and weakening of their irradiation-shielding ability. In the area around waste packages, certain radical products generated from water molecules by gamma irradiation can induce decomposition and condensation reactions of soluble HS molecules, and subsequently affect the complexation and sorption behavior of metal ions. The significance of gamma-irradiation-induced chemical changes in HSs near nuclear waste has been recently established. Sawai et al. characterized HSs irradiated using ⁶⁰Co-emitted gamma rays, and found that the amount of high-molecular-weight compounds decreased as the radiation dose increased by gel-permeation chromatography and infrared spectrophotometry; moreover, the gamma irradiation was proposed to decompose the HSs [121]. Silva et al. observed release of CO₂ gas when HA solutions were gamma-irradiated, which was believed to be induced by the decomposition of –COOH, as indicated by IR spectra. Additionally, the molecular simulation package, HyperChem 4.5, which involves the Hamiltonian PM 3 semi-empirical method, was employed to simulate the IR spectra of

possible products of the irradiated HA. The radiolysis mechanisms of -COOH were believed to be linked to the benzyl ester and phenol ester structures of HA molecules [122]. Sasaki et al. investigated the changes in acidic-functional-group contents of a gamma-irradiated HS solution by acid–base titration, and found that a function of the various carboxylic groups in the HS was deactivated by the gamma irradiation. Moreover, the gamma irradiation dose was found to be dependent on the apparent formation constants of HS with Cu^{2+} ions; the apparent formation constants varied from 4 to 6 in the dose range of 0–500 kGy [123].

In summary, gamma-irradiation-induced physiochemical variations in HS solutions have been investigated. However, useful information on the complexing ability of HS to metal ions has not been adequately emphasized and explained. Moreover, the variation in the chemical properties of HSs can significantly affect the sorption behavior of metal ions. Additionally, the dependence of the sorption behavior of HA and nuclides on the gamma irradiation dose has not been sufficiently studied in the context of safety assessment.

1.7 Objective of the thesis

With respect to the global proliferation of new large-scale nuclear plants [16], the safe handling of HLW and SF generated by nuclear plants is a major scientific and engineering challenge. The long-lived fission products from the irradiation of uranium-based fuels [124] are planned to be buried in well-engineered deep underground repositories [125]. Although the possibility of early failure of waste packages after repository closure is extremely low, the radionuclides can probably leach via groundwater media from the fractured waste packages and subsequently migrate to the biosphere. Therefore, the migration of radionuclides is an important component of the safety assessment of nuclear waste.

The sorption of radionuclides onto host rock in GDF areas can be exploited as an effective barrier to inhibit their transport. Several simulation-, field-, and laboratory-based studies have demonstrated that the sorption of metal ions in groundwater can be significantly affected by NOM, such as the abundant and ubiquitous HS molecules in groundwater, via complexation or colloidal formations of HS and metal ions [111, 112]. However, the gamma rays stemming from the decay of radionuclides can pass through the steel canisters of waste packages under these conditions because of their high penetration, and a long-term gamma irradiation field can be generated near the waste packages [126]. The gamma irradiation can affect the chemical properties of HSs, subsequently leading to interactions between HSs and metal ions. Nevertheless, the effects of gamma-irradiated HSs on the sorption of metal ions have not been clarified to date.

This study was aimed at elucidating the dependence of gamma-irradiated HA solutions on the sorption of metal ions, which can enable the prediction of radionuclide migration and help establish a sorption coefficient database. For this purpose, research was conducted on investigating the impact of gamma irradiation on the complexation of HSs with metal ions, including the apparent formation constant and the complexation affinity in terms of molecular-weight fractions.

The thesis includes several chapters that explain the research conducted on achieving the aforementioned goals. The first part includes an introductory section that describes the research background and purpose of this study (**Chapter 1**). The general concepts of deep geological disposal of nuclear waste, the possible consequences of disposal failure, and the sorption behavior of radionuclides are summarized herein. Moreover, the motivation for an investigation on the effects of gamma irradiation on the sorption behavior of radionuclides in groundwater is established.

The second part includes the experimental, results, and discussion sections. The gamma-irradiation-induced complexation of metal ions with HS, including the apparent formation constant and the complexation affinity in terms of the molecular-weight fractions, are described in **Chapter 2** and **Chapter 3**. The data and results described in **Chapters 2** and **3** provide the data for simulation and explanation, as reported in **Chapter 4**, in which the effects of gamma-irradiated HA solutions on the sorption of metal ions are described. Therefore, the crucial research-related information is described in **Chapters 2, 3, and 4**. **Chapter 2** reports the use of various analytical approaches, such as TOC analysis, UV–Vis spectroscopy, ^{13}C NMR, and potentiometric titration, to investigate the physicochemical properties of HSs. Moreover, the effects of the irradiation dose on the complexation ability of metal ions and HSs, that is, the apparent formation constant of HS–metal-ion complexes, was discussed based on the Ca-ISE method. The fractionation of an HA solution irradiated with doses of 0–100 kGy via ultrafiltration is detailed in **Chapter 3**, with an emphasis on the identification of gamma-irradiation-induced changes in TOC and the number of functional groups ($-\text{COOH}$ and phenolic $-\text{OH}$) in each HA fraction. Based on the concentration of metal ions and organic carbon in each fraction, the effects of gamma irradiation on the molecular-weight-dependent complexation affinity of HA fractions with Cs^+ , Sr^{2+} , and Eu^{3+} ions were evaluated; these ions are the mono-, di-, and tri-valent cations typically found in nuclear waste, respectively. In **Chapter 4**, batch sorption experiments conducted for studying the sorption coefficients of gamma-irradiated HA and Cs^+ and Eu^{3+} as typical mono- and tri-valent cations in nuclear waste, respectively, are described. Sedimentary rock samples obtained from a depth of 140 m at the Horonobe URL (JAEA) were used as the solid sorbent. The aging effects of the irradiated HA–metal interactions on sorption are also discussed.

The third part of this thesis (**Chapter 5**) includes the conclusions, significance of thesis and recommendation for further work. The research presented in **Chapters 2, 3,** and **4** are summarized, and the future studies which are not considered in the thesis are proposed.

Reference

- [1] United Nations, United nations framework convention on climate change (UNFCCC), 1992.
- [2] United Nations, Kyoto protocol to the united nations framework convention on climate change, 1998.
- [3] United Nations, Paris agreement, 2015.
- [4] B. Li, How China plans to achieve carbon peak and carbon neutrality, 2021. Retrieved 1, 2022, from <https://earth.org/china-carbon-peak-carbon-neutrality/>.
- [5] U.S. environmental protection agency, Sources of greenhouse gas emissions, Retrieved 1, 2022, from <https://www.epa.gov/ghgemissions/sources-greenhouse-gas-emissions>.
- [6] A. Horvath, E. Rachlew, Nuclear power in the 21st century: Challenges and possibilities, *Ambio* **45** (2016), 38–49.
- [7] International Atomic Energy Agency (IAEA), Nuclear power reactors in the world, Reference data series No.2, 2021.
- [8] World Nuclear Association, Nuclear power in the world today, 2022. Retrieved 1, 2022, from <https://www.world-nuclear.org/information-library/current-and-future-generation/nuclear-power-in-the-world-today.aspx>.
- [9] World Nuclear Association, Nuclear share figures, 2010-2020, 2021. Retrieved 1, 2022, from <http://www.world-nuclear.org/information-library/facts-and-figures/nuclear-generation-by-country.aspx>.
- [10] World Nuclear Association, Nuclear power in China, 2022. Retrieved 1, 2022, from <https://world-nuclear.org/information-library/country-profiles/countries-a-f/china-nuclear-power.aspx>.
- [11] International Atomic Energy Agency (IAEA), Annual report 2007, 50 years of atoms

- for peace, 2008.
- [12] U.S. Nuclear Regulatory Commission, Approved applications for power uprates, 2021. Retrieved 1, 2022, from <https://www.nrc.gov/reactors/operating/licensing/power-uprates/status-power-apps/approved-applications.html>.
- [13] H. Paillere, J. Donovan, Nuclear power 10 years after Fukushima: The long road back. Retrieved 1, 2022, from <https://www.iaea.org/newscenter/news/nuclear-power-10-years-after-fukushima-the-long-road-back>.
- [14] International Energy Agency (IEA), World energy Outlook 2020, Paris, 2020.
- [15] International Energy Agency (IEA), Global Energy Review 2021, 2021.
- [16] S. Saito, Role of nuclear energy to a future society of shortage of energy resources and global warming, *J. Nucl. Mater.* **398** (2010), 1–9.
- [17] H.P. gen. Schieck, Key nuclear reaction experiments, Discoveries and consequences. 2015.
- [18] U.S.E.I.A. (EIA), Nuclear explained: The nuclear fuel cycle, 2021.
- [19] A.M. Macfarlane, M. Miller, Nuclear energy and uranium resources, *Elements*. **3** (2007), 185–192.
- [20] The global crisis of nuclear waste, a report commissioned by GP France, 2018.
- [21] Spent fuel reprocessing options, IAEA-TECDOC-1587, 2008.
- [22] T. Fukui, T. Matsuda, Disposal of high level nuclear waste (in Japanese), in: Recycle of nuclear fuel (in Japanese).
- [23] World Nuclear Association, What is nuclear waste, and what do we do with it?, 2021. Retrieved 1, 2022, from <https://world-nuclear.org/nuclear-essentials/what-is-nuclear-waste-and-what-do-we-do-with-it.aspx>.
- [24] Center for Disease Control and Prevention, Contamination vs. exposure, Emerg.

- Manag. Radiation, Chem. Branch, 2018.
- [25] Radiation Effects Research Foundation, How radiation harms cells, Retrieved 1, 2022, from https://www.rerf.or.jp/en/about_radiation/how_radiation_harms_cells_e/.
- [26] M.L. Iglesias, A. Schmidt, A. Al Ghuzlan, L. Lacroix, F. de Vathaire, S. Chevillard, M. Schlumberger, Radiation exposure and thyroid cancer: A review, *Arch. Endocrinol. Metab.* **61** (2017), 180–187.
- [27] E.B. Howard, W.J. Clarke, M.T. Karagianes, R.F. Palmer, Strontium-90-induced bone tumors in miniature swine, *Radiat. Res.* **39** (1969), 594–607.
- [28] S.C. Darby, R. Doll, Fallout, radiation doses near Dounreay, and childhood leukaemia, *Br. Med. J.* **294** (1987), 603–607.
- [29] M. V. Ramana, Technical and social problems of nuclear waste, *Wiley Interdiscip. Rev. Energy Environ.* **7** (2018), 1–12.
- [30] U.S. Nuclear Regulatory Commission, Backgrounder on radioactive waste. Retrieved 1, 2022, from <https://www.nrc.gov/reading-rm/doc-collections/fact-sheets/radwaste.html>.
- [31] S. Moffett, Three permanent disposal sites for radioactive waste in Europe by 2025, 2014. Retrieved 1, 2022, from <https://ec.europa.eu/research-and-innovation/en/horizon-magazine/three-permanent-disposal-sites-radioactive-waste-europe-2025>.
- [32] S. Gin, A. Abdelouas, L.J. Criscenti, W.L. Ebert, K. Ferrand, T. Geisler, M.T. Harrison, Y. Inagaki, S. Mitsui, K.T. Mueller, J.C. Marra, C.G. Pantano, E.M. Pierce, J. V. Ryan, J.M. Schofield, C.I. Steefel, J.D. Vienna, An international initiative on long-term behavior of high-level nuclear waste glass, *Mater. Today.* **16** (2013), 243–248.
- [33] A. Yoshida, Considering the geological disposal program of high-level radioactive waste through classroom debate, Debate. In: Nakajima K. (eds) Nuclear Back-end and

- Transmutation Technology for Waste Disposal. Springer, Tokyo. 2015.
- [34] Ashik Kalam, Where is Europe's nuclear waste?. Retrieved 1, 2022, from <https://www.virtual.prosperoevents.com/blog/where-is-europes-nuclear-waste>.
- [35] M.C. Thorne, Is Yucca Mountain a long-term solution for disposing of US spent nuclear fuel and high-level radioactive waste?, *J. Radiol. Prot.* **32** (2012), 175–180.
- [36] Special Review Committee on the NUMO Safety Case Atomic Energy Society of Japan, Report of the Special Review Committee on the NUMO safety case Special Review Committee on the NUMO Safety Case Atomic Energy Society of Japan, 2019.
- [37] World nuclear news, Construction of test disposal tunnel under way at Onkalo, 2021. Retrieved 1, 2022, from <https://world-nuclear-news.org/Articles/Construction-of-test-disposal-tunnel-under-way-at>.
- [38] World nuclear news, Swedish municipality gives approval for fuel repository, 2020. Retrieved 1, 2022, from <https://world-nuclear-news.org/Articles/Swedish-municipality-gives-approval-for-fuel-repos>.
- [39] Power technology, Managing nuclear waste in France: the long and short game, 2018. Retrieved 1, 2022, from <https://www.power-technology.com/features/managing-nuclear-waste-france-long-short-game/>.
- [40] N. Jawerth, Under one roof: Russia's integrated strategy for spent fuel management, International Atomic Energy Agency (IAEA), 2019. Retrieved 1, 2022, from <https://doi.org/https://www.iaea.org/newscenter/news/under-one-roof-russias-integrated-strategy-for-spent-fuel-management>.
- [41] M.N. Burke, Michigan reps press Biden to stop Canadian plan to store nuclear waste near Lake Huron, The Detroit News, 2021. Retrieved 1, 2022, from <https://www.detroitnews.com/story/news/politics/2021/11/26/biden-pressed-stop-canadian-nuclear-waste-storage-near-lake-huron/8725074002/>.

- [42] B. Carter, G. Nieder-Wertermann, China begins construction of its first underground research laboratory for high level waste disposal, International Atomic Energy Agency (IAEA), 2021. Retrieved 1, 2022, from <https://www.iaea.org/newscenter/news/china-begins-construction-of-its-first-underground-research-laboratory-for-high-level-waste-disposal>.
- [43] Made for minds, Germany to shut controversial Gorleben nuclear waste facility, 2021. Retrieved 1, 2022, from <https://www.dw.com/en/germany-to-shut-controversial-gorleben-nuclear-waste-facility/a-59211763>.
- [44] The Straits Times, Villages in Japan are competing to become a nuclear waste site, 2021. Retrieved 1, 2022, from <https://www.straitstimes.com/asia/east-asia/villages-in-japan-are-competing-to-become-a-nuclear-waste-site>.
- [45] World nuclear news, Nagra reports on siting options for Swiss encapsulation plant, 2020. Retrieved 1, 2022, from <https://world-nuclear-news.org/Articles/Nagra-reports-on-siting-options-for-Swiss-encapsul>.
- [46] T. Greene, Nuclear storage plans for north of England stir up local opposition, The Guardian, 2021. Retrieved 1, 2022, from <https://www.theguardian.com/environment/2021/aug/23/nuclear-storage-plans-for-north-of-england-stir-up-local-opposition>.
- [47] World nuclear news, USA relaunches used fuel management programme, 2021. Retrieved 1, 2022, from <https://www.world-nuclear-news.org/Articles/USA-relaunches-used-fuel-management-programme>.
- [48] S. Yamasaki, Underground research laboratory program in Japan: Its technical and social aspects, Japan Nuclear Cycle Development Institute Horonobe Underground Research Center.
- [49] B. Carter, G. Nieder-Westermann, China begins construction of its first underground

- research laboratory for high level waste disposal, International Atomic Energy Agency (IAEA), 2021. Retrieved 1, 2022, from <https://www.iaea.org/newscenter/news/china-begins-construction-of-its-first-underground-research-laboratory-for-high-level-waste-disposal>.
- [50] J. Zaugg, N. Fang, China plans giant underground lab to research nuclear waste, Cable News Network (CNN). 2019. Retrieved 1, 2022, from <https://edition.cnn.com/2019/09/06/china/china-nuclear-waste-intl-hnk-trnd/index.html>.
- [51] World Nuclear News, China starts building underground lab, 2021. Retrieved 1, 2022, from <https://world-nuclear-news.org/Articles/China-starts-building-underground-lab>.
- [52] A.H. Delandar, Modeling defect structure evolution in spent nuclear fuel container materials, KTH Royal Institute of Technology, 2017.
- [53] V. V. Rondinella, Failure mechanisms of high level nuclear waste forms in storage and geological disposal conditions, in: Handb. Adv. Radioact. Waste Cond. Technol., Woodhead P, 2011: pp. 397–432.
- [54] Radioactive waste management, Geological disposal: waste package evolution status report, 2017.
- [55] Japanese Nuclear Cycle Development Institute (JNC), H12: Project to establish the scientific and technical basis for HLW disposal in Japan., Ibaraki, 2000.
- [56] T. Fujita, et., Horonobe Underground Research Laboratory project synthesis of phase I investigation 2001–2005. Volume “Geological disposal research,” Japan Atomic Energy Agency Tono Geoscientific Research Unit, JAEA-Research. 39 (2010).
- [57] S. Matsumoto, I. Machida, K.H. Hebig, S. Zeilfelder, N. Ito, Estimation of very slow groundwater movement using a Single-Well Push-Pull test, *J. Hydrol.* **591** (2020), 125676.

- [58] Unit Converter, Convert roentgen/hour [R/h] to gray/second [Gy/s].
- [59] Grove software, MicroShield® Pro and MicroShield® LT.
- [60] A. Sweetnam, Deep geologic repository project for low and intermediate level waste—project description, Report Number: 00216-REP-07722.07-00001, 2005.
- [61] M. Gobien, Preliminary hazard assessment of waste from an advanced fuel cycle, NWMO-TR-2015-22, 2015.
- [62] R.P. Morco, J.M. Joseph, D.S. Hall, C. Medri, D.W. Shoesmith, J.C. Wren, Modelling of radiolytic production of HNO₃ relevant to corrosion of a used fuel container in deep geologic repository environments, *Corros. Eng. Sci. Technol.* **52** (2017), 141–147.
- [63] M. Wu, M. Behazin, J. Nam, P. Keech, R. Morco, Internal corrosion of used fuel container, NWMO-TR-2019-02, Ontario, 2019.
- [64] D. Cui, J. Low, K. Spahiu, Environmental behaviors of spent nuclear fuel and canister materials, *Energy Environ. Sci.* **4** (2011), 2537–2545.
- [65] F. Yanagisawa, H. Sakai, Leaching behaviour of a simulated nuclear waste glass in groundwater of 50–240 °C, *Appl. Geochemistry* **3** (1988), 153–163.
- [66] E.Y. Vernaz, J.L. Dussossoy, Current state of knowledge of nuclear waste glass corrosion mechanisms: the case of R7T7 glass, *Appl. Geochemistry* **7** (1992), 13–22.
- [67] M. Terashima, T. Endo, K. Miyakawa, Determination of humic substances in deep groundwater from sedimentary formations by the carbon concentration-based DAX-8 resin isolation technique, *J. Nucl. Sci. Technol.* **57** (2020), 380–387.
- [68] H. Kunimaru, T., Ota, K., Alexander, W. Russell, Yamamoto, Groundwater/porewater hydrochemistry at Horonobe URL : Data Freeze I, JAEA-Research 2010-035, 2010.
- [69] D.L. Sparks et al, Methods of soil analysis. Part 3-chemical methods. Madison (WI): Soil Science Society of America, 1996.
- [70] J.H. Weber, S.A. Wilson, The isolation and characterization of fulvic acid and humic

- acid from river water, *Water Res.* **9** (1975), 1079–1084.
- [71] M.H.B. Hayes, P. MacCarthy, R.L. Malcolm, R.S. Swift, The search for structure: setting the scene, in: John Wiley & Sons (Ed.), *Humic Substance. II*, New York, 1989.
- [72] L. Cooper, The value of humic substances in the carbon lifecycle of crops: humic acids, fulvic acids and beyond, *AgroPages Mag.* (2017), 1–6.
- [73] F.J. Stevenson, *Humus chemistry: genesis, composition, reactions*, 1994.
- [74] S. Wang, C.N. Mulligan, Effect of natural organic matter on arsenic release from soils and sediments into groundwater, *Environ. Geochem. Health* **28** (2006), 197–214.
- [75] B.A.G. De Melo, F.L. Motta, M.H.A. Santana, Humic acids: Structural properties and multiple functionalities for novel technological developments, *Mater. Sci. Eng. C* **62** (2016), 967–974.
- [76] F.J. Stevenson, *Humus chemistry: genesis, composition, reactions*, John Wiley & Sons, 1994.
- [77] M.J.M. Wells, Supramolecular answers to the organic matter controversy, *J. Environ. Qual.* **48** (2019), 1644–1651.
- [78] F.J. Stevenson, Q. van Winkle, W.P. Martin, Physico-chemical investigations of clay-absorbed organic colloids: 2, *Soil Sci. Soc. Am. Proc.* **17** (1953), 31–34.
- [79] E.L. Piret, R.G. White, H.C. Walther, A.J. Madden, Some physico-chemical properties of peat humic acids, *Sci. Proc. R. Dublin Soc.* **A1** (1960), 39–79.
- [80] A. Nebbioso, A. Piccolo, Advances in humeomics: Enhanced structural identification of humic molecules after size fractionation of a soil humic acid, *Anal. Chim. Acta* **720** (2012), 77–90.
- [81] A.J. Simpson, Determining the molecular weight, aggregation, structures and interactions of natural organic matter using diffusion ordered spectroscopy, *Magn. Reson. Chem.* **40** (2002), 72–82.

- [82] A. Piccolo, M. Spiteller, Electrospray ionization mass spectrometry of terrestrial humic substances and their size fractions, *Anal. Bioanal. Chem.* **377** (2003), 1047–1059.
- [83] T.L. Brown, J.A. Rice, Effect of experimental parameters on the ESI FT-ICR mass spectrum of fulvic acid, *Anal. Chem.* **72** (2000), 384–390.
- [84] T.L. Brown, J.A. Rice, The effect of laser wavelength and power density on the laser desorption mass spectrum of fulvic acid, *Org. Geochem.* **31** (2000), 627–634.
- [85] Nuclear energy agency (NEA), Thermochemical Database (TDB) Project.
- [86] F.J. Mompeán, H. Wanner, The OECD nuclear energy agency thermochemical database project, *Radiochim. Acta* **91** (2003), 617–622.
- [87] C. Plaza, V. D’Orazio, N. Senesi, Copper(II) complexation of humic acids from the first generation of EUROSOLS by total luminescence spectroscopy, *Geoderma* **125** (2005), 177–186.
- [88] T. Sasaki, H. Yoshida, T. Kobayashi, I. Takagi, H. Moriyama, Determination of apparent formation constants of Eu(III) with humic substances by ion selective liquid membrane electrode, *Am. J. Anal. Chem.* **3** (2012), 462–469.
- [89] T. Sasaki, S. Aoyama, H. Yoshida, Y. Kulyako, M. Samsonov, T. Kobayashi, I. Takagi, B. Miyasoedov, H. Moriyama, Apparent formation constants of Pu(IV) and Th(IV) with humic acids determined by solvent extraction method, *Radiochim. Acta* **100** (2012), 737–745.
- [90] T. Sakuragi, S. Sawa, S. Sato, T. Kozaki, T. Mitsugashira, M. Hara, Y. Suzuki, Interaction of Americium(III) with humic acid over wide pH region, *J. Radioanal. Nucl. Chem.* **265** (2005), 349–353.
- [91] J. Adusei-Gyamfi, B. Ouddane, L. Rietveld, J.P. Cornard, J. Criquet, Natural organic matter-cations complexation and its impact on water treatment: A critical review,

- Water Res.* **160** (2019), 130–147.
- [92] R. Artinger, B. Kienzler, W. Schußler, J.I. Kim, Effects of humic substances on the ^{241}Am migration in a sandy aquifer: column experiments with Gorleben groundwater/sediment systems, *J. Contam. Hydrol.* **35** (1998), 261–275.
- [93] A.G.S. Prado, J.D. Torres, P.C. Martins, J. Pertusatti, L.B. Bolzon, E.A. Faria, Studies on copper(II)- and zinc(II)-mixed ligand complexes of humic acid, *J. Hazard. Mater.* **136** (2006), 585–588.
- [94] J.W. Thomason, W. Susetyo, L.A. Carreira, Fluorescence studies of metal–humic complexes with the use of lanthanide ion probe spectroscopy, *Appl. Spectrosc.* **50** (1996), 401–408.
- [95] K. Schmeide, S. Sachs, M. Bubner, T. Reich, K.H. Heise, G. Bernhard, Interaction of Uranium(VI) with various modified and unmodified natural and synthetic humic substances studied by EXAFS and FTIR spectroscopy, *Inorganica Chim. Acta.* **351** (2003), 133–140.
- [96] H. Geckeis, T. Rabung, T. Ngo Manh, J.I. Kim, H.P. Beck, Humic colloid-borne natural polyvalent metal ions: Dissociation experiment, *Environ. Sci. Technol.* **36** (2002), 2946–2952.
- [97] I. Baek, W.W. Pitt, Colloid-facilitated radionuclide transport in fractured porous rock, *Waste Manag.* **16** (1996), 313–325.
- [98] C.P. Jen, S.H. Li, Effects of hydrodynamic chromatography on colloid-facilitated migration of radionuclides in the fractured rock, *Waste Manag.* **21** (2001), 499–509.
- [99] S. Nagao, M. Aoyama, A. Watanabe, T. Tanaka, Complexation of Am with size-fractionated soil humic acids, *Colloids Surfaces A Physicochem. Eng. Asp.* **347** (2009), 239–244.
- [100] E. Bolea, M.P. Gorriz, M. Bouby, F. Laborda, J.R. Castillo, H. Geckeis, Multielement

- characterization of metal–humic substances complexation by size exclusion chromatography , asymmetrical flow field-flow fractionation , ultrafiltration and inductively coupled plasma-mass spectrometry detection : A comparative approach, *J. Chromatogr. A.* **1129** (2006), 236–246.
- [101] M. Fall, O. Nasir, T.S. Nguyen, A coupled hydro-mechanical model for simulation of gas migration in host sedimentary rocks for nuclear waste repositories, *Eng. Geol.* **176** (2014), 24–44.
- [102] C. Appel, L.Q. Ma, R.D. Rhue, E. Kennelley, Point of zero charge determination in soils and minerals via traditional methods and detection of electroacoustic mobility, *Geoderma* **113** (2003), 77–93.
- [103] T. Kanti, K.C. Khilar, Review on subsurface colloids and colloid-associated contaminant transport in saturated porous media, *Adv. Colloid Interface Sci.* **119** (2006), 71–96.
- [104] Z. Chen, G. Montavon, S. Ribet, Z. Guo, J.C. Robinet, K. David, C. Tournassat, B. Grambow, C. Landesman, Key factors to understand in-situ behavior of Cs in Callovo-Oxfordian clay-rock (France), *Chem. Geol.* **387** (2014), 47–58.
- [105] A.J. Fuller, S. Shaw, C.L. Peacock, D. Trivedi, I.T. Burke, EXAFS Study of Sr sorption to illite, goethite, chlorite, and mixed sediment under hyperalkaline conditions, *Langmuir* **32** (2016), 2937–2946.
- [106] T. Sasaki, K. Ueda, T. Saito, N. Aoyagi, T. Kobayashi, I. Takagi, T. Kimura, Y. Tachi, Sorption of Eu^{3+} on Na-montmorillonite studied by time-resolved laser fluorescence spectroscopy and surface complexation modeling, *J. Nucl. Sci. Technol.* **53** (2016), 592–601.
- [107] D.I. Kaplan, S.M. Serkiz, J.D. Allison, Europium sorption to sediments in the presence of natural organic matter: A laboratory and modeling study, *Appl.*

- Geochemistry* **25** (2010), 224–232.
- [108] M. Pédrot, A. Dia, M. Davranche, Double pH control on humic substance-borne trace elements distribution in soil waters as inferred from ultrafiltration, *J. Colloid Interface Sci.* **339** (2009), 390–403.
- [109] L. Qian, J. Zhao, P. Hu, Y. Geng, W. Wu, Effect of pH, fulvic acid and temperature on sorption of Th (IV) on zirconium oxophosphate, *J. Radioanal. Nucl. Chem.* **283** (2010), 653–660.
- [110] M. Ge, D. Wang, J. Yang, Q. Jin, Z. Chen, W. Wu, Z. Guo, Co-transport of U(VI) and akaganéite colloids in water-saturated porous media: Role of U(VI) concentration, pH and ionic strength, *Water Res.* **147** (2018), 350–361.
- [111] J.F. McCarthy, B. Gu, L. Liang, J. Mas-Pla, T.M. Williams, T.C.J. Yeh, Field tracer tests on the mobility of natural organic matter in a sandy aquifer, *Water Resour. Res.* **32** (1996), 1223–1238.
- [112] J.F. McCarthy, K.R. Czerwinski, W.E. Sanford, P.M. Jardine, J.D. Marsh, Mobilization of transuranic radionuclides from disposal trenches by natural organic matter, *J. Contam. Hydrol.* **30** (1998), 49–77.
- [113] A. Křepelová, S. Sachs, G. Bernhard, Uranium(VI) sorption onto kaolinite in the presence and absence of humic acid, *Radiochim. Acta* **94** (2006), 825–833.
- [114] Y. Seida, M. Terashima, Y. Tachi, K. Iijima, T. Nakazawa, M. Yamada, M. Yui, Sorption and diffusion of Eu in sedimentary rock in the presence of humic substance, *Radiochim. Acta.* **98** (2010), 703–709.
- [115] Y. Tachi, T. Suyama, M. Ochs, C. Ganter, Development of JAEA sorption database (JAEA-SDB): Update of data evaluation functions and sorption/QA data, JAEA-Data/Code. 2010–031, 2011.
- [116] I.E. Makariv, A. V. Ponomarev, Radiation-induced degradation of organic compounds

- and radiation technologies for purification of aqueous systems, in: Ionizing Radiation Effects and Applications (Ed.: B. Djezzar), London: United Kingdom, 2018.
- [117] H. Morawetz, Radiation chemistry-principles and applications, *J. Polym. Sci. Part C Polym. Lett.* **25** (1987).
- [118] S. Le Caër, Water radiolysis: Influence of oxide surfaces on H₂ production under ionizing radiation, *Water* **3** (2011), 235–253.
- [119] D.W. Lee, W.S. Choi, M.W. Byun, H.J. Park, Y.M. Yu, C.M. Lee, Effect of γ -irradiation on degradation of alginate, *J. Agric. Food Chem.* **51** (2003), 4819–4823.
- [120] Y. Liu, J. Chen, X. Wu, K. Wang, X. Su, L. Chen, H. Zhou, X. Xiong, Insights into the effects of γ -irradiation on the microstructure, thermal stability and irradiation-derived degradation components of microcrystalline cellulose (MCC), *RSC Adv.* **5** (2015), 34353–34363.
- [121] T. Sawai, T. Sawai, T. Shimokawa, Radiation decomposition of humic substances in landfill disposal leachate, *Radioisotopes* **28** (1979), 355–360.
- [122] W.T.L. Da Silva, S.C. Da Silva, M.O. De Oliveira Rezende, Influence of gamma-radiation on the behavior of humic acids from peat and tropical soil, *J. Radioanal. Nucl. Chem.* **222** (1997), 29–34.
- [123] T. Sasaki, R. Goto, T. Saito, T. Kobayashi, T. Ikuji, Y. Sugiyama, Gamma-ray irradiation impact of humic substances on apparent formation constants with Cu(II), *J. Nucl. Sci. Technol.* **55** (2018), 1299–1308.
- [124] Q. Hu, J. Weng, J. Wang, Sources of anthropogenic radionuclides in the environment : a review, *J. Environ. Radioact.* **101** (2010), 426–437.
- [125] K. Miura, Y. Okui, H. Horii, Micromechanics-based prediction of creep failure of hard rock for long-term safety of high-level radioactive waste disposal system, *Mech. Mater.* **35** (2003), 587–601.

- [126] H. Sawamura, K. Nishimura, M. Naito, T. Ohi, Y. Ishihara, A. Neyama, Evaluation of long-term irradiation field in geological disposal of high-level radioactive wastes, *J. Nucl. Sci. Technol.* **37** (2000), 310–315.

Chapter 2 Effect of gamma irradiation on the complexation of humic substances with Ca^{2+} ions

2.1 Introduction

If the HLW packaging failed during the early stages of disposal, radionuclides would leach from it. Of all radionuclides, the alkaline earth $^{90}\text{Sr}^{2+}$ ion (half-life of 29 y) significantly contributes to the radiotoxicity of fission products, and is the main cause of bone cancer [1], tissue cancer, and leukemia [2]. In addition, nuclear weapon testing, uranium mining, and catastrophic nuclear power plant accidents could also release radioactive Sr, which could subsequently migrate via groundwater. McCarthy et al. demonstrated that the mobilization and transport of radionuclides in groundwater resulted from their complexation with natural organic matter [3], which occurs because HA masks the absorption of radionuclide cations on mineral or rock surfaces by forming colloidal metal–HA complexes. Various thermodynamic studies on the interaction of HS with divalent metal ions, such as Pb^{2+} , Cu^{2+} , Cd^{2+} , and Zn^{2+} [4], and transuranium elements, including trivalent Cm^{3+} and Am^{3+} ions [5], have been performed, and have aimed to better understand and predict the migration patterns of hazardous metals. The complexes radionuclides form with HS increase the possibility of radionuclides to affect the population and environment. Hence, it is essential to investigate the interactions between metal ions and HS to estimate the radiation-associated risks.

As described in **Section 1.6.2**, the gamma irradiation field could induce the radicals from water molecules, which could react with HS in the groundwater. However, the particular chemical properties of HS attributed to gamma irradiation and the effects of gamma-irradiation on metal–HS interactions have not been fully elucidated yet. Therefore, in this study, various analytical approaches, namely total organic carbon (TOC) analysis, ultraviolet–visible (UV–Vis) spectroscopy, ^{13}C nuclear magnetic resonance (NMR), and

potentiometric titration, were adopted to investigate the effects of gamma irradiation on the physicochemical properties of HS. TOC analysis is a standard analytical technique that has been widely used to study the organic carbon content in HS. UV–Vis absorption spectroscopy is widely accepted as being an appropriate method to estimate the properties of HS. UV–Vis spectra revealed the presence of specific bonding arrangements in HS molecules, but offered little information on HS functionalities. However, the ratio of relative absorbance, which could be determined using UV–Vis spectroscopy and provide information on the structural changes HS underwent after gamma-irradiation. Liquid state ^{13}C NMR spectroscopy using the inverse-gated decoupling (IGD) technique could be a powerful analytical tool for obtaining quantitative information on the structure of aqueous HS [6]. Potentiometric acid–base titration in aqueous solution could be used to evaluate the proton exchange capacities of functional groups, particularly the O-containing carboxylic $-\text{COOH}$ and phenolic $-\text{OH}$ groups of HS. Using this information, the effect of the irradiation dose on the complexation ability of metal ions and HS, that is, the apparent formation constant of HS-metal ions complexes was discussed. In this study, Ca was adopted as the chemical analog of divalent alkaline-earth metal ions Sr [7]. The apparent formation constants of Ca-HS complexes were determined via the direct measurement of the concentration of free Ca^{2+} ions using a commercially available Ca ion-selective electrode (Ca-ISE).

2.2 Experimental

2.2.1 Preparation of HS samples

Three standard HS were used in this study,

(1) Elliott soil humic acid (abbreviated as S-HA, 1S102H) was supplied from the International Humic Substance Society (IHSS);

(2) Suwannee river fulvic acid (abbreviated as S-FA, 1S101F) was also supplied by

the IHSS;

(3) Technical humic acid sodium (abbreviated as AL-HA, H16752) was purchased from Sigma-Aldrich Co.

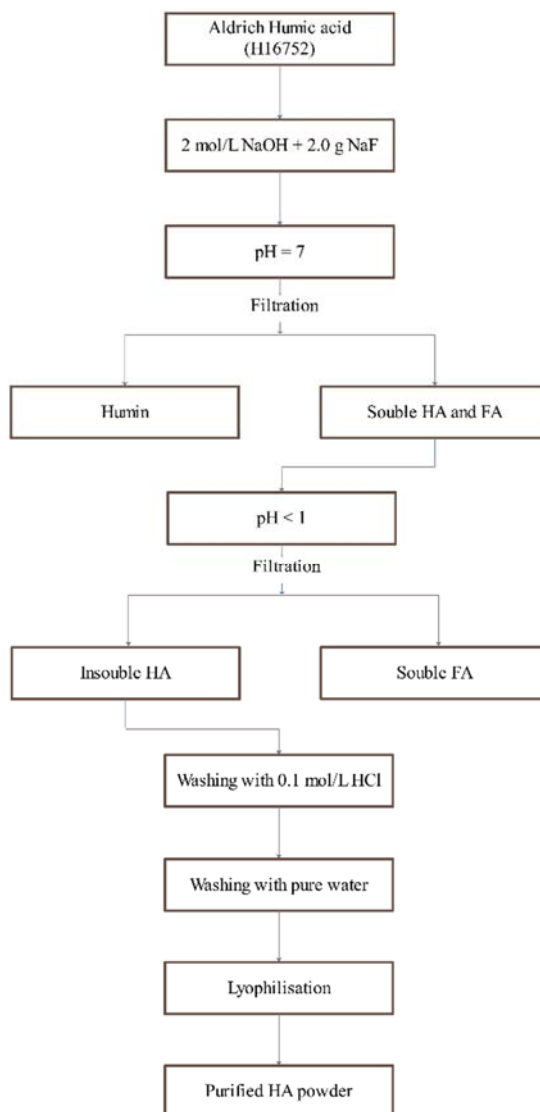


Fig. 2-1 Flow diagram of purification of Aldrich humic acid (AL-HA) based on the pH solubility of organic components.

S-HA and S-FA were used as received, without further treatment while AL-HA was purified prior to the experiments. The purification process of AL-HA is based on the pH-related solubility of organic ingredients (also see **Fig. 2-1**) [8, 9]. First, 20 g of crude HA sodium salt was dissolved in a 2 mol/dm³ NaOH solution under stirring, and 2.0 g of NaF

was added to the mixture to dissolve silicate impurities. The resulting dark-colored solution was subsequently acidified to pH 7.0, filtrated to remove humin, and then acidified to pH 1.0 via the dropwise addition of a HCl solution under continuous stirring to precipitate HA. The precipitate separated after centrifugation and sequential filtration (1.0 μm , 0.45 μm), was washed three times with a 0.1 mol/dm³ HCl solution followed by rinsing with deionized water to remove Cl⁻ ions. Lastly, the HA powder was lyophilized using a freeze dryer, stored, and sealed for subsequent analysis and experiments. The yield of purified HA was calculated to be approximately 30 %. The chemicals (Wako, Japan) used for our experiments were of analytical-grade. Ultra-pure water with a resistivity of >18.2 m Ω /cm at 25 °C, which was prepared using a Direct-Q UV 3 (Merck, USA) water purification system was used throughout the study.

0.37 g S-HA, 0.30 g S-FA and 0.36 g purified AL-HA powders were weight and added in 120 mL NaOH (1 mol/dm³). After complete dissolution, 1820 mL NaClO₄ (0.1 mol/dm³) solution and 60 mL HClO₄ (0.1 mol/dm³) was added into each HS solution, to obtained the initial concentration of 0.19 g/dm³, 0.15 g/dm³ and 0.18 g/dm³ for S-HA, S-FA and AL-HA, respectively. The ionic strength (*I*) and initial pH in HS solution were 0.1 mol/dm³ (NaClO₄) and about 11, respectively.

2.2.2 Gamma irradiation on HS samples

The aforementioned HS solution was divided into four 500-mL amber glass vessels (Duran, Germany), which were tightly sealed with screw caps without degassing. The vessels were subjected to gamma irradiation using an approximately 150-TBq ⁶⁰Co source at a temperature of 20–22 °C at the Institute for Integrated Radiation and Nuclear Science (KURNS), Kyoto University. Absorbed doses of gamma irradiation were 10, 100, and 500 kGy, and the constant dose rate were 1 or 0.1 kGy/h, respectively. After the exposure time

necessary to obtain the correct dose, the three irradiated samples and one non-irradiated sample were totally transferred to polyethylene bottles, stored in the dark for two weeks, and subsequently used for experiments.

2.2.3 Characterization of irradiated HS solution

2.2.3.1 TOC

A TOC-5000 analyzer (Shimadzu, Kyoto) was used for TOC analysis. To minimize the carbonate ion content, the HS sample solution was acidified to pH 2 and pure O₂ gas was bubbled through it for 5 min. Thereafter, the solution was injected into the vertical furnace of the analyzer via a sampling tube with the internal diameter of 2 μm. The combustion quartz tube, which was filled with Pt catalyst was maintained at 680 °C using pure O₂ gas flow, and the produced CO₂ was monitored using a non-dispersive infrared gas detector. All measurements were performed in triplicates.

2.2.3.2 UV–Vis spectroscopy

The UV–Vis absorption spectra of the dissolved HS were recorded on a SEC 2000-UV/Vis double beam spectrophotometer (ALS Co., Ltd., Japan) using quartz cells with the path length of 10 mm. After adjusting the pH to 8, the samples were scanned in the range of 230 to 750 nm at 25 °C (integration time of 20 ms). Milli-Q water was used as the reference for correction.

2.2.3.3 Liquid ¹³C NMR spectra

The liquid ¹³C NMR spectra of the samples were recorded using an AVANCE 600 (Bruker Instruments, Inc., Germany) spectrometer at 600 MHz and 25 ± 0.3 °C. The IGD technique was used for all measurements under the following conditions: spectrometer

frequency of 150.95 MHz, acquisition time of 0.87 s, relaxation delay of 10 s; solvent D₂O; and probe 5 mm CPTCI 1H-13C/15N/D Z-GRD. HA samples (0.5 mL) were used to fill 5 mm-diameter tubes. In addition, 0.05 mL of 100 mg/dm³ 3-trimethylsilylpropionic-2, 2, 3, 3-d₄ acid sodium salt solution was used as external chemical shift referencing. Scans numbering 20000 were accumulated for each sample.

2.2.3.4 Acid–base titration on HS solution

Potentiometric titrations were performed using an AT-510 (KEM Co., Ltd., Japan) automatic potentiometric titration instrument. The titration container was purged with high-purity N₂ for 10 min prior to the titrations, and high-purity N₂ was continuously flown above the solutions during the titrations to ensure that CO₂ did not contaminate the samples. The ionic strength of the background electrolyte ($I = 0.01 \text{ mol/dm}^3$) was controlled by adding NaClO₄ to it. After the pH of the combined glass electrode was calibrated using standard buffers, 20 mL HS solution was acidified to pH 3.0–3.5, and then titrated to the endpoint pH of 10.5. A CO₂-free standardized 0.01 mol/dm³ NaOH solution (Fujifilm Wako, Japan) was used as the titrant. Titrations were carried out at 25 °C in successive 10 μL/min intervals using a micropipette. Titration experiments were performed at 25 ± 0.5 °C under a constant stirring speed of 200 rpm. After each titrant aliquot was added, the volume of titrant and pH were automatically recorded when the readings stabilized below ± 0.1 mV/s. Herein, the measured pH was assumed to be the direct measurement of the H⁺ ion activity in the bulk solution. Each titration experiment lasted 2–2.5 h and generated more than 80 data points.

2.2.4 Determination of apparent formation constant

The activity of the free Ca²⁺ ions was measured using a 6583S-10C (HORIBA, Japan) Ca-ISE, which was calibrated using a standard Ca stock solution at 25 °C prior to

each measurement. First, the polypropylene vessels were filled with 20 mL HS solutions, and the surfaces of the sample solutions were purged with pure N₂ gas for 5 min. The volume unit of the titrant was maintained at 0.02 mL Ca(ClO₄)₂ solution (1 × 10⁻² mol/dm³). The stable potential of the Ca-ISE (fluctuations lower than ± 0.1 mV every 2 min) and pH were recorded for every titration step. Assuming that the activity was equal to the Ca²⁺ ion concentration at constant pH, a linear relationship should exist between the electromotive force E_{ISE} (mV) and the logarithm of the concentration of free Ca²⁺ ions (not complexed with HS) (mol/dm³), which would correspond to the Nernstian behavior of the Ca-ISE.

$$E_{\text{ISE}} = s \log[\text{Ca}^{2+}] + E^*, \quad (2-1)$$

where E^* is the standard electrode potential and s represent the slope. E^* and s could be determined by analyzing a series of standard solutions of known concentrations. The ionic strength of the sample solution was constant at 0.01 mol/dm³ NaClO₄, the pH was maintained at 5.00 ± 0.05, and the stirring speed was constant at 200 rpm. The titration was repeated 10 times. The log β_{app} values, where β_{app} is the apparent formation constant of the Ca-HS complexes, were calculated at each titration point and were subsequently averaged and used to determine the experimental standard deviation (σ).

2.3 Theoretical

The identification of the protonated functional groups of HS would help to investigate their reactivity during the interaction between HS and metal ions. Owing to the overlap in the wide-range titration results for the two abundant acidic functional groups, namely carboxylic -COOH and phenolic -OH, it was difficult to distinguish their individual contribution. In this study, a modified numerical model was adopted to quantify these two functional groups based on the change in the total concentration of organic anions ($[\text{R}^-]$)

with pH. Here $[R^-]$ (eq/dm³) is the concentration of the dissociated functional groups, which can be calculated using the electroneutrality equation. The dilution-corrected concentration of inorganic Na⁺ cations and Cl⁻ anions in solution were recalculated at each experimental point during titration considering the initial solution and additional titrant. $[H^+]$ was assumed to be the measured pH. The ionic product constant of water (pK_w) at 25 °C was retrieved from the literature [10]. Therefore, the organic charge at any point during a titration could be determined using the charge balance, as follows:

$$[R^-] = [Na^+] + [H^+] - [ClO_4^-] - [OH^-] \quad (2-2)$$

The organic charge density Q (meq/g) was obtained by normalizing $[R^-]$ to the dissolved organic carbon content, $(C)_{org}$, in the unit of g/dm³ at each point during the titration. Then, the titration curves (the pH dependence of Q) were obtained as follows:

$$Q = 1000 \times \frac{[R^-]}{(C)_{org}}. \quad (2-3)$$

Subsequently, the titration curves of the dependence of Q on pH were obtained. The binding sites of HS are typically attributed to the proton-dissociative O-containing functional groups (–COOH and phenolic –OH groups). Although other functional groups, such as the amino and sulfhydryl groups, could also participate in the protonation process, their contribution could be omitted because HS only contains low amounts of these groups [11]. Conceptually, the apparent protonation constants of –COOH and phenolic –OH groups were expressed as functions of the pH and ionic strength [12]. The apparent protonation constant (K_{app}) was defined as $[HR]/[H^+][R^-]$, where $[HR]$ (eq/dm³) is the concentration of non-dissociated groups in the solution.

$$\log K_{app} = \log K + m\text{pH} - b \log[Na^+], \quad (2-4)$$

where $\log K$ is defined as $\log K_{app}$ at pH 0 and $\log [Na^+] = 0$, m is a number between 0 and

1, which depends on the strength and abundance of binding sites [13], and b is a parameter associated with the protonated functional groups because it is related to the charge and charge density of macromolecules and does not depend on the types of functional groups [14]. The bulk Na^+ ion concentration in the background electrolyte solution was constant ($[\text{Na}^+] = 0.01 \text{ mol/dm}^3$), and b could not be evaluated, and therefore, it was set to be 0 in this study. The organic charge density Q comprised Q_i of the $-\text{COOH}$ (meq/g) and phenolic $-\text{OH}$ groups (meq/g), as illustrated in **Eq. (2-5)**:

$$Q = \sum_{i=1}^2 \frac{Q_i}{1+10^{(\log K_i + (m_i-1)\text{pH})}}, \quad (2-5)$$

where the $i = 1$ and 2 are the contributions of the $-\text{COOH}$ and phenolic $-\text{OH}$ groups, respectively. The optimal Q_i , $\log K_i$, and m_i ($i = 1$ and 2) parameters were determined using nonlinear least-square fitting analysis for the titration plots of Q vs. pH. The nonlinear iterative fitting routine of the Origin 2018 software was used. For more accurate and unique fitting results, the logarithms of the acid dissociation constants K_1 and K_2 were conditional: 3–6 for $\log K_1$, and 8–11 for $\log K_2$, respectively [15].

Assuming that one Ca^{2+} ion could interact with two neighboring anionic functional groups, the following mass conservation equations for Ca^{2+} and HS were defined when Ca^{2+} ions was added into the HS solutions:

$$[\text{Ca}^{2+}]_{\text{tot}} = [\text{Ca}^{2+}] + [\text{CaR}_2] \quad (2-6)$$

$$\frac{(\text{C})_{\text{org}}}{1000} Q_{\text{tot}} = [\text{HR}] + [\text{R}^-] + 2[\text{CaR}_2] \quad (2-7)$$

where $[\text{CaR}_2]$ (mol/dm^3) is the concentration of Ca^{2+} ions bound to HS, and was calculated as the difference between $[\text{Ca}^{2+}]_{\text{tot}}$ (mol/dm^3), which was the total concentration of added Ca^{2+} ion solution, and $[\text{Ca}^{2+}]$ (mol/dm^3), which was the concentration of free Ca^{2+} ions and was directly measured using the Ca-ISE. The hydrolysis reaction of Ca^{2+} ions was negligible

in this study; the distribution ratio of $[\text{Ca}(\text{OH})^+]$ was more than eight order of magnitude lower than the initial $[\text{Ca}^{2+}]$ at pH 5 using the hydrolysis constant [16]. In **Eq. (2-7)**, Q_{tot} was considered to be the maximum capacity of the proton-exchanging sites, which equaled the sum of Q_1 and Q_2 . The degree of dissociation of HS ($= [\text{R}^-]/([\text{HR}] + [\text{R}^-])$), was a pH-dependent constant. Eventually, an equation analogous to the Langmuir adsorption isotherm was used to calculate β_{app} , as **Eq. (2-8)**:

$$\beta_{\text{app}} = \frac{[\text{CaR}_2]}{[\text{Ca}^{2+}][\text{R}^-]} \quad (2-8)$$






















2.4 Results and discussion

2.4.1 pH and appearance of HS solution

The pH and appearance of irradiated HS solution were summarized in **Table 2-1**. The initial solution pH shifted to neutral from 11 with dose, indicating that the hydrogen ions were generated by the impact of gamma irradiation, while no pH shift was observed without gamma irradiation. A mount of produced gas in the irradiated HS bottles was found, even the cap of the glass bottle was popped when it was opened. The obvious change in solution color after gamma irradiation was also observed. The typical brownish color, which was caused by increasing the number of conjugated double bonds and π electron density in heteropolycondensates [17], was observed for the initial solutions: dark brown for HAs (S-HA and AL-HA) and light brown for S-FA. High dose gamma irradiations of 500 kGy obviously faded the samples from brown to colorless due to radiolysis degradation of organic compounds [18].

It is worthy noted that a blackish solidified matter precipitated in the S-HA and AL-HA series at 500 kGy while no significant precipitation was observed in the S-FA samples, which is probably due to the difference in natural chemical properties of HA and FA. Therefore, the supernatant in HA solution at 500 kGy was used in the experiments.

Table 2-1 Dependence of appearance and pH of humic substance (HS) solution with dose and dose rate. The values below the pictures show the pH. The supernatant in HA series samples (S-HA and AL-HA) at 500 kGy was used due to the formation of precipitation, while the other irradiated solution was used without any additional treatment.

Dose rate (kGy/h)	1				0.1		
Dose (kGy)	0	10	100	500	10	100	500
S-HA							
	11.2	10.7	7.2	6.9	10.3	7.6	6.2
S-FA							
	11.0	9.9	7.2	6.8	10.3	8.1	6.2
AL-HA							
	11.3	10.8	6.9	6.7	11.4	7.1	6.2

2.4.2 TOC measurements of HS solution

Organic carbon is the major component of the structural framework and functional groups of HS. The TOC of HS decreased as the gamma irradiation dose increased (**Fig. 2-2**), which indicated that the decomposition of HS progressed. Same as described above, a small amount of a gas popped when the cap of the glass bottle was opened after gamma irradiation. Silva et al. used IR spectroscopy and gas chromatography to demonstrate that CO₂ formed in gamma-irradiated HS solutions, and proposed that the presence of CO₂

confirmed the participation of the -COOH groups in the structural changes that HS underwent under gamma irradiation [19]. In addition, the TOC content of HS solution decreased by more than 80 % on average at the gamma irradiation dose of 500 kGy, which indicated that the organic carbons of the non-functional groups, such as the aliphatic or aromatic carbons, decomposed. Furthermore, the tendency of TOC to decrease as the gamma irradiation dose increased was similar at two different dose rates (1 and 0.1 kGy/h), and thus, it was hypothesized that decarburization was possibly independent of the dose rate.

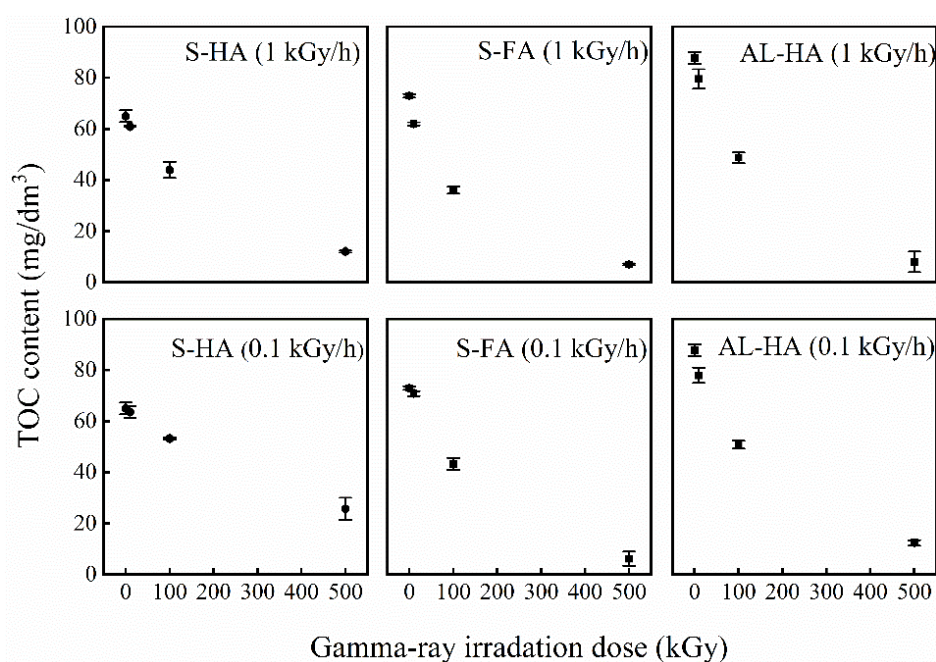


Fig. 2-2 Dependence of total organic carbon (TOC) content on dose and dose rate

2.4.3 UV–Vis spectrometry

A typical HS UV–Vis spectrum is depicted in **Fig. 2-3**. The absorbance of all HS samples decreased as the wavelength increased, where the typical absorbance without any clear shoulder peak ranged from 225 to 745 nm decreased monotonically with the total gamma irradiation dose. The decrease in the UV absorbance of the HS samples was explained by the decomposition of the unsaturated conjugated bonds in the chemical structure of the dissolved organic matter [20].

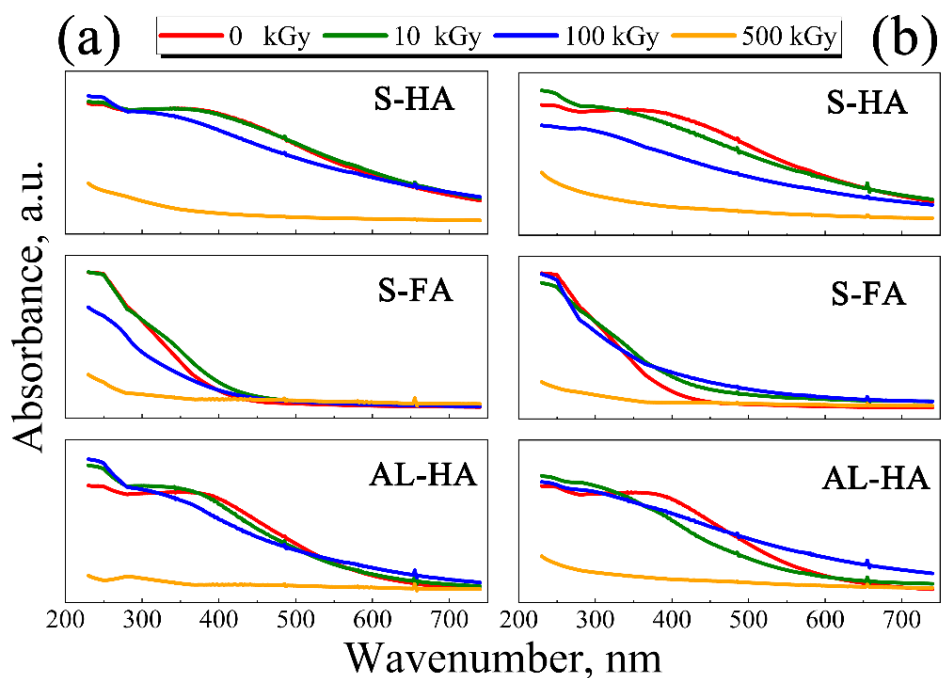


Fig. 2-3 UV–Vis absorption spectra of non-irradiated and irradiated HS samples (a): 1 kGy/h; (b): 0.1 kGy/h

For S-HA, S-FA and AL-HA, the A_2/A_3 ratio, where A_2 and A_3 are the absorbance at 250 and 365 nm, respectively, in general increased as the gamma irradiation dose increased (Table 1), which implied that the relative molecular weights of HS decreased [21]. The decomposition of both aliphatic and aromatic carbons owing to the radiolysis degradation of HS leads to the formation of smaller molecules [22, 23].

The A_4/A_6 values, where A_4 and A_6 are the absorbance of S-HA, S-FA and AL-HA at 465 and 665 nm, respectively, were related to the content of O-containing functional groups such as –OH, carbonyl, –COOH, and ester groups [24]. The decrease in A_4/A_6 suggested the decomposition of these O-containing functional groups of HS.

Table 2-2 Optical indices of S-HA, S-FA and AL-HA obtained using UV–Vis absorbance data at different gamma irradiation doses and dose rates

Irradiation dose (kGy)		0	10	100	500	10	100	500
Dose rate (kGy/h)		1			0.1			
S-HA	A_2/A_3	1.04	1.06	1.23	2.72	1.21	1.26	2.07
	A_4/A_6	2.75	2.50	2.12	2.25	2.40	2.16	2.10
	AI	1.00	1.07	1.47	1.26	1.12	1.26	1.56
S-FA	A_2/A_3	3.00	2.91	3.35	3.10	2.61	2.90	3.43
	A_4/A_6	5.26	4.47	4.26	2.00	3.29	2.93	2.00
	AI	0.86	0.99	1.23	1.25	0.98	1.52	1.41
AL-HA	A_2/A_3	1.06	1.22	1.47	1.59	1.32	1.24	1.89
	A_4/A_6	8.15	5.58	3.20	2.02	4.15	2.38	2.07
	AI	0.74	0.88	1.43	1.33	0.92	1.40	1.85

For phenolic substances, aniline derivatives, benzoic acids, and polycyclic aromatic hydrocarbons, the absorption in the range of 270-280 nm corresponds to the π - π^* electron transition [25]. The aromaticity index AI as unsaturation level of HS molecule represents the absorbance at 280 nm normalized by the TOC. These results in **Table 2-2** indicated the same tendency for all HS: that is, the AI increased with the gamma irradiation dose. This indicated that the effects of gamma irradiation on HA and FA appeared to be similar, and that aromatic structures could be more resistant to gamma irradiation than aliphatic ones. Moreover, the UV–Vis absorption spectra of the HS samples revealed that different gamma irradiation dose rates presented the same effect on all HS.

2.4.4 ^{13}C NMR analysis

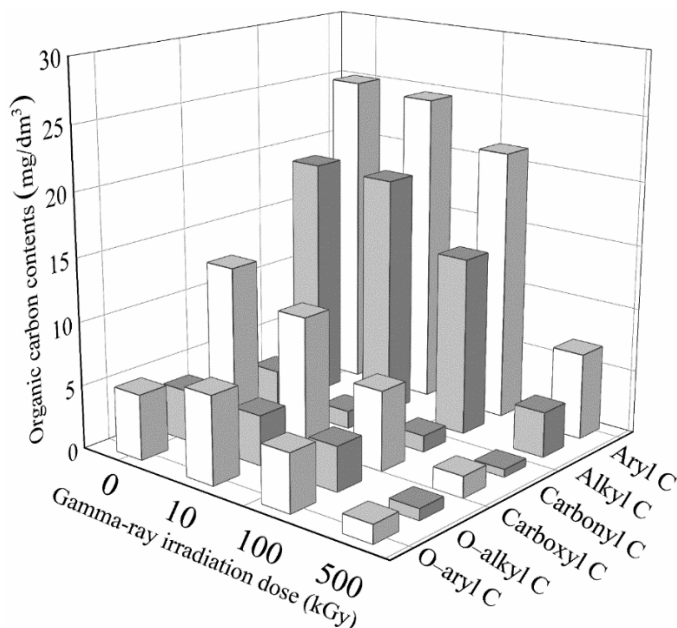


Fig. 2-4 Dependence of organic carbon content of several types of C atoms in a sample of S-HA on gamma irradiation dose at dose rate of 1 kGy/h

The ^{13}C NMR spectra peaks were assigned using their chemical shifts, and the range of shifts could be divided into six regions [27]: alkyl, O-alkyl, aryl, O-aryl, carboxyl, and carbonyl C (5–45, 45–110, 110–145, 145–165, 165–190, and 190–220 ppm, respectively). The three-dimensional graph in **Fig. 2-4** illustrates the dependence of the content of carbon atoms on the gamma irradiation dose for several types of C atoms in S-HA. Each content of carbon atom was estimated using the product of the relative ratio of the peak areas with corresponding TOC values. The aryl and alkyl C contents decreased significantly as the gamma irradiation dose increased, indicating that gamma irradiation contributed to the cleavage of the aromatic and aliphatic C bonds. Compared to the initial content of Aryl C, it was decomposed to 98 %, 85 %, 27 % by 10, 100 and 500 kGy irradiation, respectively. On the other hand, that of Alkyl C was 99 %, 73 %, 18 %, indicating that the extent of decomposition of aromatic C was less than that of aliphatic C. This phenomenon would be

consistent with the conclusion from UV–Vis spectroscopy study. The contents of carboxyl and carbonyl C decreased as the gamma irradiation dose increased. The contents of the other functional groups, namely O–alkyl and O–aryl C, also decreased overall as the gamma irradiation dose increased, although not linearly.

2.4.5 Titration of functional groups

The experimental plots of the titration experiment are presented in **Fig. 2-5**. Most fitting curves of the potentiometric titration data were in good agreement with the experimental results. The obtained parameters and the corresponding σ values are summarized in **Table 2-3**. No significant differences were observed in the data collected at different gamma irradiation dose rates; moreover, Q_1 decreased as the gamma irradiation dose increased, and Q_2 slightly increased as the gamma irradiation dose increased, although some data were scattered. These opposite tendencies could imply that phenolic structures were more resistant to gamma irradiation than the –COOH groups, which was in agreement with the results derived from the ^{13}C NMR data. Ilcin et al. investigated the anti-gamma-irradiation stability of HS by Fourier transform infrared spectroscopy, and proposed that the unstable moiety towards gamma irradiation was the –COOH group [28]. However, this would be only suitable for humic materials. Different phenomena were observed for other macromolecules like starch may be due to the decomposition of its abundant ester group [29]. Lastly, Q_{tot} decreased as the gamma irradiation dose increased.

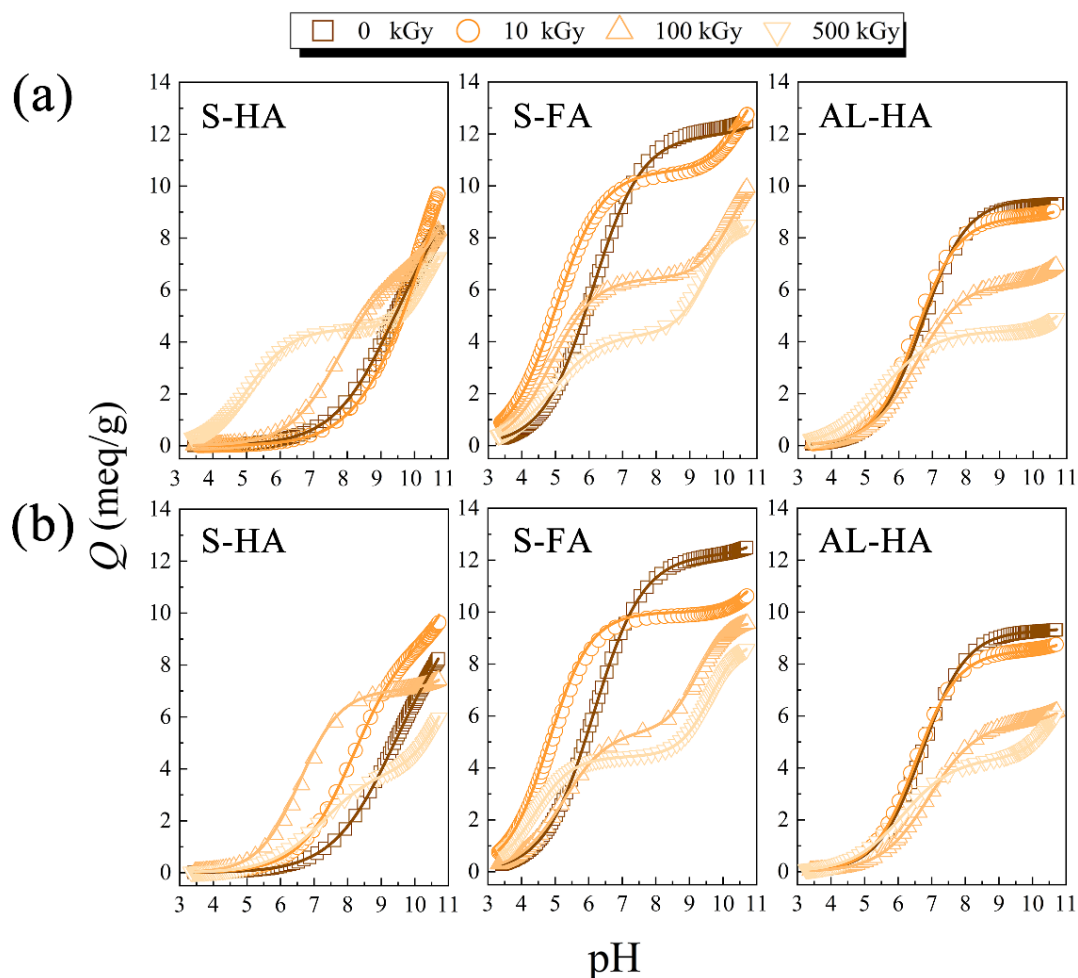


Fig. 2-5 Experimental titration data of humic substances obtained via nonlinear fitting. The points and solid lines represent experimental data and the fitting equations with six parameters Q_1 , Q_2 , K_1 , K_2 , m_1 , m_2 , respectively. **(a)**: 1 kGy/h; **(b)**: 0.1 kGy/h.

Both K_1 and K_2 decreased slightly as the gamma irradiation dose increased. This tendency could be attributed to the gamma irradiation inducing a decrease in the total number of functional group and in the molecular size of HS, which could be caused by the breaking of some of the intramolecular hydrogen bonds between the functional groups [30]. The same tendency was observed for all three analyzed HS, namely S-HA, S-FA, and AL-HA, although some points ascribed to the $-\text{COOH}$ and phenolic $-\text{OH}$ groups were scattered and appeared to be independent.

Table 2-3 Nonlinear regression fitting of potentiometric titration curves of S-HA, S-FA and AL-HA

Dose (kGy)	Dose rate (kGy/h)	Q_1 (meq/g)	Q_2 (meq/g)	Q_{tot} (meq/g)	$\log K_1$	$\log K_2$	m_1	m_2
S-HA								
0		9.61(14)	3.40(29)	13.01	4.48(45)	10.12(48)	0.52(04)	0.14(10)
10		8.85(35)	3.85(27)	12.70	4.76(72)	9.51(41)	0.50(08)	0.08(11)
100	1	6.89(49)	4.81(07)	11.70	4.51(24)	9.43(07)	0.42(10)	0.15(02)
500		4.51(34)	4.47(32)	8.98	3.46(07)	9.76(25)	0.32(00)	0.07(01)
10		9.14(45)	3.66(19)	12.80	4.50(03)	10.06(18)	0.45(03)	0.11(04)
100	0.1	7.05(24)	5.06(21)	12.11	4.67(24)	9.66(29)	0.30(08)	0.20(00)
500		3.97(41)	5.18(35)	9.15	3.96(34)	9.19(40)	0.45(14)	0.16(03)
S-FA								
0		12.23(71)	4.01(50)	16.24	3.63(17)	9.47(04)	0.41(11)	0.22(08)
10		10.46(45)	4.06(27)	14.52	3.16(29)	9.31(09)	0.37(07)	0.12(04)
100	1	6.45(62)	4.57(21)	11.02	3.33(04)	9.23(21)	0.32(02)	0.09(06)
500		4.31(44)	4.38(36)	8.69	3.06(10)	9.19(20)	0.38(11)	0.02(01)
10		9.87(60)	3.86(42)	13.73	3.37(48)	9.61(14)	0.31(15)	0.16(11)
100	0.1	5.46(24)	4.27(19)	9.73	3.41(26)	9.21(02)	0.35(04)	0.01(01)
500		4.44(11)	4.51(53)	8.95	3.42(08)	9.03(19)	0.22(09)	0.06(02)
AL-HA								
0		9.30(24)	3.17(50)	12.47	4.43(12)	10.11(75)	0.34(14)	0.24(10)
10		8.87(68)	3.57(25)	12.44	4.46(12)	9.68(36)	0.31(07)	0.21(12)
100	1	6.31(52)	4.13(30)	10.44	4.10(24)	9.71(28)	0.37(04)	0.16(07)
500		4.41(20)	4.24(07)	9.65	3.21(36)	9.87(45)	0.42(12)	0.16(05)
10		8.54(44)	3.24(61)	11.78	4.49(25)	9.91(11)	0.31(02)	0.18(11)
100	0.1	5.85(04)	3.78(32)	9.63	4.16(40)	9.66(32)	0.40(06)	0.19(03)
500		4.37(31)	3.62(41)	7.99	3.56(07)	9.49(08)	0.42(04)	0.12(07)

A possible reaction path for the radiolysis of HS molecules was proposed. Radiation-induced decarboxylation was caused by the radical-induced dissociation of the $-\text{COOH}$ groups (**Fig. 2-6a**). The gas generated by the irradiated aliphatic carboxylic acid was analyzed using a gas chromatograph [31, 32]. Then, the $-\text{COOH}$ group was dissociated and replaced by a H atom. This was accompanied by the generation of CO_2 gas, and would strongly support the decrease in TOC. Moreover, the HS molecule could be hydroxylated via the attack of an $\cdot\text{OH}$ radical (**Fig. 2-6b**). Campos et al. and Brillas et al. have identified the radiolytic degradation products of 2, 4-D dimethylamine salt using electrospray ionization mass spectrometry, and indicated that the lateral chains could break and phenolic $-\text{OH}$ groups would form [33, 34], which might result in the formation of small-molecular-size fraction. In addition, the radiolysis of HS might include the random cleavage of the C–C bonds and the ring-breakage reaction of aromatic compounds, which might also cause the decrease in the molecular weight of HS and in the TOC by producing a CH_4 gas [35]. Since no direct evidence for the mechanism of TOC decrease has been reported, however, further studies might be needed to clarify the mechanism of radiolysis.

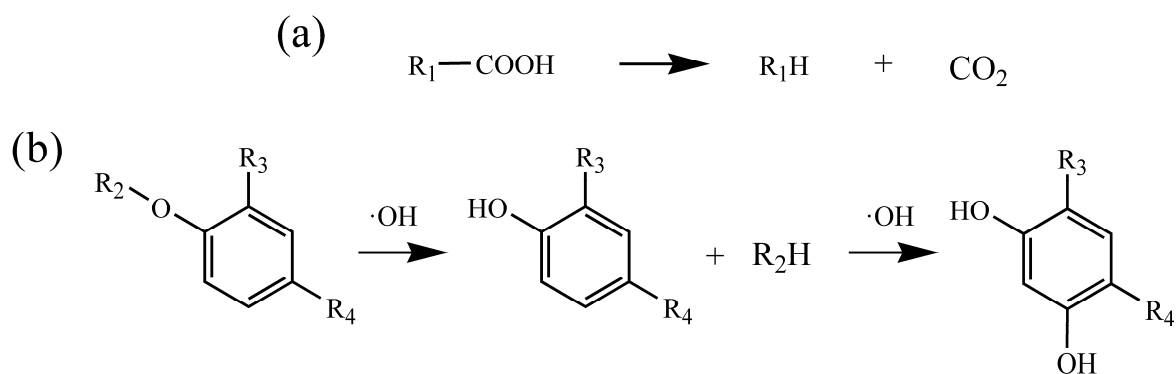


Fig. 2-6 Simplified radiolysis mechanisms of humic substances (HS): (a) decarboxylation and (b) hydroxylation.

2.4.6 Effect of gamma irradiation on Ca–HS complexation

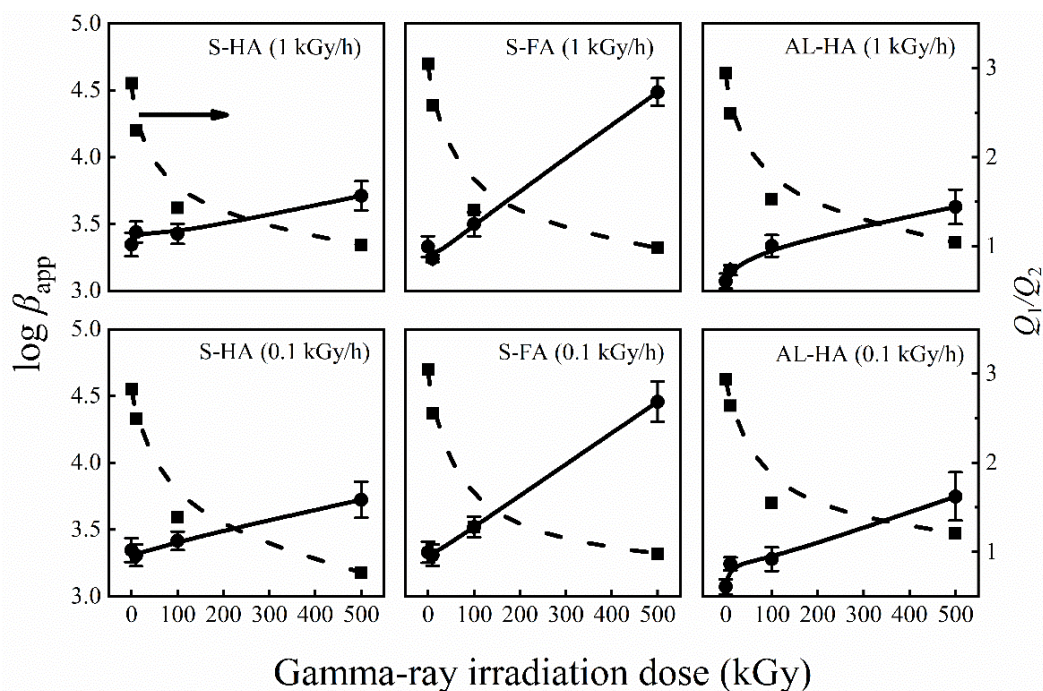


Fig. 2-7 Dependence of $\log \beta_{app}$ on gamma irradiation dose and dose rate; here β_{app} is the apparent formation constant of the Ca–HS complexes at pH 5 and 0.01 mol/dm^3 (NaClO_4); Q_1 and Q_2 denote the organic charge densities of $-\text{COOH}$ and phenolic $-\text{OH}$ groups, respectively; solid and broken lines represent the eye guide.

Fig. 2-7 illustrates the dependence of β_{app} of Ca–HS complexes on the gamma irradiation dose and dose rate. For the non-irradiated Ca–HS complex (0 kGy), $\log \beta_{app}$ was 3.0–3.5, which was in good agreement with the previously reported value of 3.32 at pH 5 [36]. Moreover, as the gamma irradiation dose increased, the β_{app} gradually increased. The Q_1/Q_2 ratios calculated from **Table 2-3** suggested that the content of $-\text{COOH}$ groups decreased and the content of phenolic $-\text{OH}$ groups increased with dose. The change of content ratio of $-\text{COOH}$ and phenolic $-\text{OH}$ groups would generally result in the different type of complexation at each binding site of HS [37, 38]. A predominance of phenolic groups with the high $\log K_2$ over $-\text{COOH}$ groups with the low $\log K_1$ would lead to an increase of

the β_{app} , since the formation of metal–ligand complexes is considered as a type of acid–base equilibrium reaction. Therefore, the Q_1/Q_2 ratio is one of indicators of the β_{app} value, even though the Q_{tot} value of HS decreased with dose increased in this study.

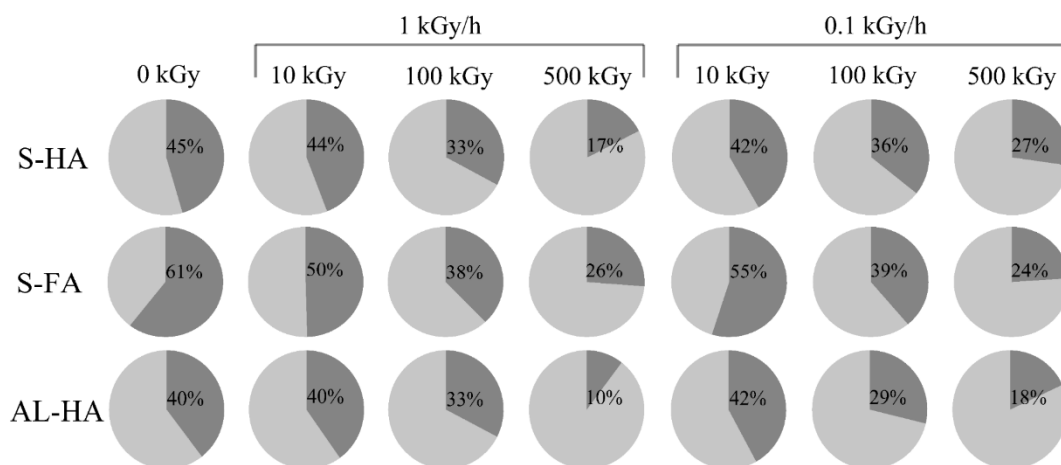


Fig. 2-8 Distribution of Ca^{2+} ions concentration complexed with HS before and after gamma irradiation; the percentages represent the ratios of $[CaR_2]$ (darker areas) to $[Ca^{2+}]_{tot}$; here $[CaR_2]$ and $[Ca^{2+}]_{tot}$ denote the concentration of Ca^{2+} ions bound to HS and that of the added Ca^{2+} ion solution.

Using the β_{app} values in **Fig. 2-7**, the distribution of Ca bound to HS to the total amount of calcium ($[CaR_2]/[Ca^{2+}]_{tot}$) was evaluated. **Fig. 2-8** illustrates the $[CaR_2]/[Ca^{2+}]_{tot}$ ratios calculated under a simulation condition at pH 5 and $[Ca^{2+}]_{tot} = 1 \times 10^{-5} \text{ mol/dm}^3$. The ratio of the concentration of Ca^{2+} complexed with HS to the total Ca^{2+} concentration in solution decreased as β_{app} increased. The results indicated that 40–60 % of the added Ca^{2+} ions reacted with the initial HS to form Ca–HS complexes, and the percentages significantly decreased to 10–30 % when the HS were exposed to gamma irradiation at doses of up to 500 kGy. This trend could be explained by the decrease in Q_{tot} of the HS. Although Q_2 increased as the gamma irradiation dose increased, the contribution of the phenolic –OH groups to Ca complexation would be suppressed at pH 5 owing to the high K_2 value.

2.5 Summary

The gamma irradiation field generated by the radioactive decay of atomic nuclei could affect the complexation ability of matrix ions, such as Ca^{2+} , and radionuclides in the presence of HS. The three HS in this study (S-HA, S-FA, and AL-HA) were irradiated using a ^{60}Co source of gamma rays, and the critical changes induced by gamma irradiation in their physiochemical properties were evaluated using classical potentiometric acid–base titration. Some notable conclusions were drawn using additional analysis methods, namely TOC analysis, UV–Vis spectrometry, and ^{13}C NMR spectrometry. The gamma irradiation doses used in this study decreased the TOC contents of HS and facilitated their degradation in the solution. We hypothesized that HS radiolysis could occur via the decarboxylation of $-\text{COOH}$ groups and hydroxylation of phenolic $-\text{OH}$ groups; however, the effect of the used gamma irradiation dose rate on the radiolysis process was not elucidated. The effect of gamma irradiation on the complexation of Ca^{2+} ions with HS was investigated at pH 5 using a Ca ion-selective electrode. Gamma irradiation increased the apparent formation constants of the Ca–HS complexes owing to the significant degradation of the $-\text{COOH}$ groups and formation of phenolic $-\text{OH}$ groups. However, the complexation ability of Ca^{2+} with HS at the same pH decreased after gamma-irradiation.

This report provides a new perspective for understanding the interactions of radionuclides with natural organic ligands in groundwater and emphasizes the idea that the effect of gamma irradiation should be considered for the more accurate prediction and estimation of nuclear hazards.

Reference

- [1] E.B. Howard, W.J. Clarke, M.T. Karagianes, R.F. Palmer, Strontium-90-induced bone tumors in miniature swine. *Radiat. Res.* **39** (1969), 594–607.
- [2] S.C. Darby, R. Doll, Fallout, radiation doses near Dounreay, and childhood leukaemia. *Br. Med. J.* **294** (1987), 603–607.
- [3] J.F. McCarthy, K.R. Czerwinski, W.E. Sanford, P.M. Jardine, J.D. Marsh, Mobilization of transuranic radionuclides from disposal trenches by natural organic matter. *J. Contam. Hydrol.* **30** (1998), 49–77.
- [4] S.W.C. Chien, M.C. Wang, Reactions of compost-derived humic substances with lead, copper, cadmium, and zinc. *Chemosphere* **64** (2006), 1353–1361.
- [5] B.V. Moulin, J. Tits, Complexation behaviour of humic substances towards actinides and lanthanides studied by time-resolved laser-induced spectrofluorometry. *Radiochim. Acta* **58** (1992), 121–128.
- [6] A. Watanabe, N. Fujitake, Comparability of composition of carbon functional groups in humic acids between inverse-gated decoupling and cross polarization/magic angle spinning ¹³C nuclear magnetic. *Anal. Chim. Acta* **618** (2008), 110–115.
- [7] S.W. Bailey, J.W. Hornbeck, C.T. Driscoll, H.E. Gaudette, Calcium inputs and transport in a base-poor forest ecosystem as interpreted by Sr isotope. *Water Resour. Res.* **32** (1996), 707–719.
- [8] J.I. Kim, G. Buckau, G.H. Li, H. Duschner, Characterization of humic and fulvic acids from Gorleben groundwater, *Fresenius. J. Anal. Chem.* **338** (1990), 245–252.
- [9] J. Kandrak, et al., Preparation and characterization of humic and fulvic acid working standards—practical experience, *J. Radioanal. Nucl. Chem.* **208** (1996), 577–592.
- [10] A.K. Covington, M.I.A. Ferra, R.A. Robinson, Ionic product and enthalpy of ionization of water from electromotive force measurements, *Faraday Trans. I.* **73**

- (1977), 1721–1730.
- [11] M.F. Benedetti, C.J. Milne, D.G. Kinniburgh, W.H. Van Riemsdijk, L.K. Koopal, Metal ion binding to humic substances: application of the non-ideal competitive adsorption model, *Environ. Sci. Technol.* **29** (1995), 446–457.
- [12] A. Kirishima, T. Ohnishi, N. Sato, O. Tochiyama, Simplified modelling of the complexation of humic substance for equilibrium calculations, *J. Nucl. Sci. Technol.* **47** (2010), 1044–1054.
- [13] O. Tochiyama, Y. Niibori, K. Tanaka, T. Kubota, H. Yoshino, A. Kirishima, B. Setiawan, Modeling of the complex formation of metal ions with humic acids, *Radiochim. Acta* **92** (2004), 559–565.
- [14] S. Kimuro, et al., Thermodynamic study of the complexation of humic acid by calorimetry, *J. Chem. Thermodyn.* **132** (2019), 352–362.
- [15] D.R. Lide, W.M.M. Haynes, G. Baysinger, L.I. Berger, H. V Kehiaian, D.L. Roth, K. Kuchitsu, D. Zwillinger, M. Frenkel, R.N. Goldberg, CRC Handbook of Chemistry and Physics, 90th Eed., *J. Am. Chem. Soc.*, 2009.
- [16] B. Kutus, A. Gácsi, A. Pallagi, I. Pálinkó, G. Peintler, P. Sipos, A comprehensive study on the dominant formation of the dissolved $\text{Ca}(\text{OH})_{2(\text{aq})}$ in strongly alkaline solutions saturated by $\text{Ca}(\text{II})$, *RSC Adv.* **6** (2016), 45231–45240.
- [17] K. Kumada, Studies on the colour of humic acids, *Soil Sci. Plant Nutr.* **11** (1965), 11–16.
- [18] T. Sasaki, R. Goto, T. Saito, T. Kobayashi, T. Ikuji, Y. Sugiyama, Gamma-ray irradiation impact of humic substances on apparent formation constants with $\text{Cu}(\text{II})$, *J. Nucl. Sci. Technol.* **55** (2018), 1299–1308.
- [19] W.T.L. da Silva, S.C. da Silva, Influence of gamma-radiation on the behavior of humic acids from peat and tropical soil, *J. Radioanal. Nucl. Chem.* **222** (1997), 29–34.

- [20] W. Goraczko, J. Slawinski, Luminescence from γ -irradiated humic acid, *J. Lumin.* **128** (2008), 1155–1161.
- [21] S. Valencia, J.M. Marín, G. Restrepo, Application of excitation–emission fluorescence matrices and UV/Vis absorption to monitoring the photocatalytic degradation of commercial humic acid, *Sci. Total Environ.* **442** (2013), 207–214.
- [22] Y. Jia, et al., Effects of light irradiation on the complexes of cadmium and humic acids : the role of thiol groups, *Chemosphere* **225** (2019), 174–181.
- [23] L. Ren, X. Wang, S. Li, J. Li, X. Zhu, L. Zhang, F. Gao, G. Zhou, Effect of gamma irradiation on structure, physicochemical and immunomodulatory properties of Astragalus polysaccharides, *Int. J. Biol. Macromol.* **120** (2018), 641–649.
- [24] V. Enev, E. Pospíšilová, M. Klučáková, T. Liptaj, L. Doskočil, Spectral characterization of selected humic substances, *Soil Water Res.* **9** (2014), 9–17.
- [25] Y.P. Chin, G. Alken, E. O’Loughlin, Molecular weight, polydispersity, and spectroscopic properties of aquatic humic Substances, *Environ. Sci. Technol.* **28** (1994), 1853–1858.
- [26] C.M. Preston, B.A. Blackwell, Carbon-13 nuclear magnetic resonance for a humic and a fulvic acid: signal-to noise optimization, quantitation, and spin-echo techniques, *Soil Sci.* **139** (1985), 88–96.
- [27] Y. Limura, T. Ohtani, S. Chersich, Characterization of DAX-8 adsorbed soil fulvic acid fractions by various types of analyses, *Soil Sci. Plant Nutr.* **58** (2012), 404–415.
- [28] M. Ilčín, O. Holá, B. Bakajová, J. Kučerík, FT-IR study of gamma-radiation induced degradation of polyvinyl alcohol (PVA) and PVA/humic acids blends, *J. Radioanal. Nucl. Chem.* **283** (2010), 9–13.
- [29] B.A. Ashwar, A. Shah, A. Gani, S.A. Rather, S.M. Wani, I.A. Wani, F.A. Masoodi, A. Gani, Effect of gamma irradiation on the physicochemical properties of alkali-

- extracted rice starch, *Radiat. Phys. Chem.* **99** (2014), 37–44.
- [30] J.A. Leenheer, R.L. Wershaw, G.K. Brown, Characterization and diagenesis of strong-acid carboxyl groups in humic substances, *Appl. Geochemistry* **18** (2003), 471–482.
- [31] A.R. Jones, The radiolysis of aliphatic carboxylic acids. On the decarboxylation of normal acids in the liquid state, *Radiat. Res.* **48** (1971), 447–453.
- [32] I. Velo-Gala, J.J. López-Peñalver, M. Sánchez-Polo, J. Rivera-Utrilla, Ionic X-ray contrast media degradation in aqueous solution induced by gamma radiation, *Chem. Eng. J.* **195–196** (2012), 369–376.
- [33] S.X. Campos, E.M. Vieira, P.J.M. Cordeiro, E. Rodrigues-Fo, M. Murgu, Degradation of the herbicide 2, 4-dichlorophenoxyacetic acid (2, 4-D) dimethylamine salt by gamma radiation from cobalt-60 in aqueous solution containing humic acid, *Radiat. Phys. Chem.* **68** (2003), 781–786.
- [34] E. Brillas, J.C. Calpe, J. Cassdo, Mineralization of 2, 4-D by advanced electrochemical oxidation processes, *Water Res.* **34** (2000), 2253–2262.
- [35] Y.S. Soebianto, I. Kusuhata, Y. Katsumura, K. Ishigure, J. Kubo, H. Kudoh, T. Seguchi, Degradation of polypropylene under gamma irradiation: protection effect of additives, *Polym. Degrad. Stab.* **50** (1995), 203–210.
- [36] G.R. Choppin, P.M. Shanbhag, Binding of calcium by humic acid, *J. Inorg. Nucl. Chem.* **43** (1981), 921–922.
- [37] T. Sasaki, H. Yoshida, S. Aoyama, T. Kobayashi, I. Takagi, H. Moriyama, Discrete fragment model for apparent formation constants of actinide ions with humic substances, *Radiochim. Acta* **103** (2015), 411–421.
- [38] R. Kautenburger, C. Hein, J.M. Sander, H.P. Beck, Influence of metal loading and humic acid functional groups on the complexation behavior of trivalent lanthanides analyzed by CE-ICP-MS, *Anal. Chim. Acta* **816** (2014), 50–59.

Chapter 3 Gamma-irradiation-induced molecular-weight distribution and complexation affinity of humic acid with Cs⁺, Sr²⁺ and Eu³⁺

3.1 Introduction

Many man-made radionuclides have been produced and released into the environment by human nuclear activities, including the operation of nuclear power plants, nuclear reactor accidents, nuclear weapon testing, and nuclear fuel reprocessing, and have caused severe radiological contamination incidents [1, 2]. The investigation of possible environmental behavior of hazardous radionuclides is necessary for evaluating biosphere safety.

Humic acid (HA) is a natural occurring organic matter in groundwater, the possible complexation ability of HA is important for predicting and investigating the environmental behavior of radionuclides. Because of the ionizable surface functional groups (mainly –COOH and phenolic –OH groups), the organic compound HA, could form stable uncharged metal–HA complexes via complexation reactions, which have been considered “organic metal colloids” [3]. Several simulations, field and laboratory studies have demonstrated that the apparent mobility of nuclides is attributed to the formation of organic colloids [4–6]. Moreover, during their migration, the molecular weight of metal–HA complexes strongly relates to their environmental behavior in groundwater, such as mobility speed. Small-weight components are typically expected to be more mobile when passing through geological materials because the advection of large-weight components requires large fracture apertures [7]. Jen et al. proposed that the dispersion coefficient of radionuclide colloids in groundwater is strongly related to their molecular weight [8]. Therefore, the study of the complexation affinity of HA with radionuclides in groundwater and the molecular weight distribution of

the metal–HA systems is critical for predicting the environmental behavior of nuclides.

Chapter 2 indicated that gamma irradiation affected the complexation affinity of HS with metal ions. However, the effect of absorbed dose on the molecular weight of metal–HA complexes has not been elucidated yet. An ultrafiltration technique should facilitate fractionation based on the weight of HA macromolecules [9], and that could be used to obtain enough volumes of HA fractions for chemical analysis and its evaluation. In this study, the HA solution irradiated with 0–100 kGy was fractionated via ultrafiltration. Emphasis was placed on the identification of gamma-irradiation-induced changes in the total organic carbon (TOC) and number of functional groups (–COOH and phenolic –OH) in each HA fraction. The effect of gamma irradiation on the molecular-weight-dependent complexation affinity of HA fractions with Cs⁺, Sr²⁺, and Eu³⁺ ions was evaluated, which are the typical mono-, di-, or tri-valent cations in nuclear waste, respectively.

3.2 Experimental

3.2.1 Preparation of irradiated HA samples

Technical-grade HA sodium salt (No. H16752) was purchased from Sigma-Aldrich Co. (USA), and was purified prior to use. The purification procedure had been summarized in **Section 2.2.1**. The purified HA powder (0.32 g) was dissolved in a drop of 2 mol/dm³ NaOH solution, then 2 dm³ HA solution (0.16 g/dm³) was prepared by adding pure water. The solution pH and ionic strength (*I*) were adjusted to 8 and 0.05 mol/dm³ (NaCl), respectively, to simulate the Na–Cl dominated saline groundwater in the Horonobe area [10].

The procedure of gamma irradiation experiments has been described in **Section 2.2.2**. In this study, the temperature of gamma irradiation was 20–23 °C. Absorbed doses of gamma irradiation was 0 (non-irradiated), 1, 5, 10, 50, and 100 kGy, respectively, with the constant dose rate of 0.69 kGy/h.

3.2.2 Sequential ultrafiltration

All the HA solutions were re-adjusted to pH 8 prior to ultrafiltration because the molecular aggregation of HA molecules is pH-sensitive [11]. The filter membrane was flushed with ultra-pure water twice prior to use. The HA solution (50 ml) was filtered through Amicon Ultra-15 (Manufacturer, Ireland) low-binding regenerated cellulose ultrafilters following the successively smaller nominal molecular weight limit of 100 (UFC910024), 50 (UFC905024), and 10 kDa (UFC901024), respectively. The samples were centrifuged using a H-103N (Kokusan, Japan) swinging-bucket rotor centrifuge. The HA retained in the filter was collected via repeated rinsing with a small amount of pure water to minimize the loss of solutes. Lastly, four fractions of HA samples were isolated based on molecular weight: UF₁ >100 kDa, UF₂ 50–100 kDa, UF₃ 10–50 kDa, and UF₄ <10 kDa. For the subsequent analyses, the HA retained in the UF₃ fraction and the filtrate of the UF₄ fraction was diluted to 50 mL, whereas the HA in the UF₁ and UF₂ fractions was diluted to 10 mL owing to their low HA concentration. Therefore, some data such as TOC were corrected by the dilution ratio. The ultrafiltration procedures were repeated two times to obtain enough volumes of HA fractions. All treatments were performed in the temperature range of 20–25 °C.

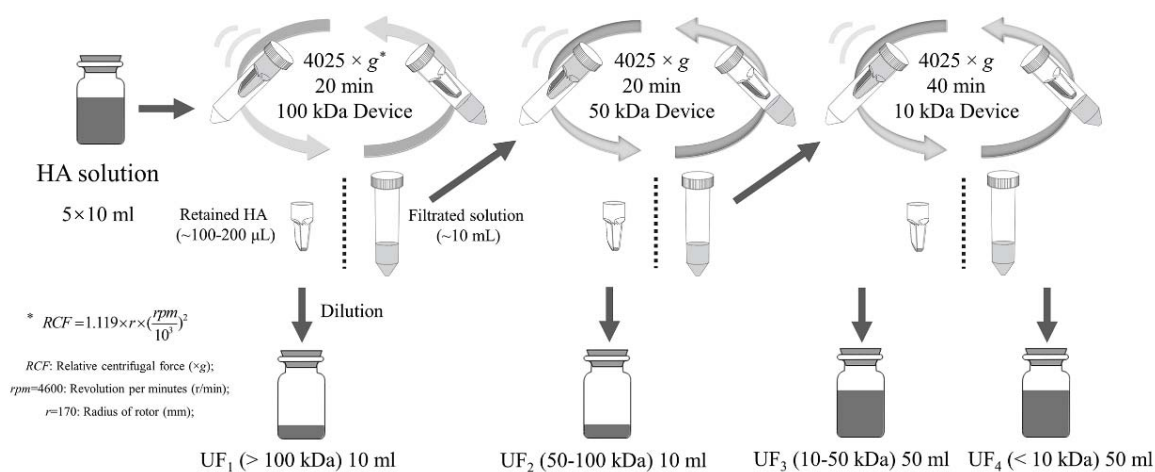


Fig. 3-1 Diagram of HA purification procedure

3.2.3 Characterization of irradiated HA samples

3.2.3.1 Zeta potential methodology

The zeta potential (ζ) of the HA samples was measured using a Zetasizer Nano ZS (Malvern Panalytical, UK) instrument at 25 °C. The incident laser beam passed through the center of a square polystyrene cell and illuminated the particles in the sample solution. Once an electrical field was applied to the cell, the moving HA compounds inside the sample caused a fluctuation in the detected light, which was proportional to the particle speed [12]. Therefore, zeta potential was calculated from the electrophoretic mobility of the particles using the Helmholtz–Smoluchowski approximation. The pH of humic samples ($I = 0.05 \text{ mol/dm}^3 \text{ NaCl}$) was adjusted to 8 using a small amount of NaOH solution. Each sample were tested in triplicate.

3.2.3.2 TOC measurement

See **Section 2.2.3.1**.

3.2.3.3 Acid–base titration of reactive functional groups

The non-filtrated original HA solution and the filtrated fractions as described in **Section 3.2.2** were used in the titration experiment without any adjusting concentration. The procedure of potentiometric titration can be found in **Section 2.2.3.4**.

3.2.4 Experiment on molecular weight distribution of metal–HA complexes

The HA samples were continuously bubbled with high-purity N_2 for 10 min prior to each experiment to eliminate the interference of dissolved CO_2 . Subsequently, 0.5 mL of an approximately 10^{-6} mol/dm^3 individual metal chloride salt solution (CsCl , SrCl_2 , or EuCl_3 >99.99 % purity) was added to 50 mL of HA solution. The solution pH was adjusted to a

final range of 7.9–8.1 using small volumes of NaOH solution. Next, the mixed solution bottles were shaken in the dark using a BR-43FL (Taitec, Japan) oscillating incubator at 25 °C. After one week, the mixtures were weight-fractionated and diluted into four equal 50 mL volume fractions (<100, 50–100, 10–50, and >10 kDa) as **Section 3.2.2**. Each fraction was subjected to TOC analysis, and the metal ion concentration of each fraction after HNO₃ digestion was determined using an ELAN DRC II (PerkinElmer SCIEX, USA) inductively coupled plasma mass spectrometry (ICP-MS) instrument. ICP-MS measurements were repeated three times for each sample solution, and the results were averaged.

3.2.5 Accuracy of ultrafiltration

To estimate the accuracy of the ultrafiltration method, the recovery ratios (R) were calculated using the mass balance, as follows:

$$R_{\text{HA}} = \frac{\sum_i (V_{\text{UF}_i} (c)_{\text{UF}_i})}{V_{\text{ini}} (c)_{\text{ini}}} \quad (3-1a)$$

and

$$R_{\text{M}} = \frac{\sum_i (V_{\text{UF}_i} [\text{M}]_{\text{UF}_i})}{V_{\text{ini}} [\text{M}]_{\text{ini}}} \quad (3-1b)$$

where (c) and $[\text{M}]$ are the concentrations of organic carbon (mg/dm^3) and metal ions (mol/dm^3) determined using TOC measurements and ICP-MS, respectively, and V is the volume of solution sample. The subscripts “ini” and “UF_{*i*}” ($i = 1-4$) indicate the initial solution and the corresponding fractions in the ultrafiltration. The R_{HA} values were satisfactory (93–103 %) after ultrafiltration using the mass balance approach, and the negligible loss of organic carbon was attributed to the sorption of small amounts of HA on the cut-off membranes and container walls. R_{Cs} and R_{Sr} also indicated acceptable recovery (91–97 % and 85–92 %, respectively) mainly because of the relatively simple speciation at

the experimental pH of 8, whereas the poor recovery of Eu^{3+} ($R_{\text{Eu}} = 53\text{--}64\%$) was attributed to the possible formation of highly adhesive hydroxides in neutral media based on solubility product (K_{sp}) estimations [13].

3.3 Theoretical

Owing to the overlap in the wide-range titration results for the two abundant acidic functional groups, namely carboxylic $-\text{COOH}$ and phenolic $-\text{OH}$, it was difficult to distinguish their individual contributions. Simple and empirical model fitting has been common practice for estimating the concentrations of $-\text{COOH}$ and phenolic $-\text{OH}$. The modified Henderson–Hasselbalch model was used to quantify the strength of the functional groups, as recommended by the International Humic Substance Society [14]. The modified Henderson–Hasselbalch model (MHHM) is similar to the described model in **Section 2.3**. The difference is that the dissociation degree (α) of weak acids was introduced in MHHM, as follows:

$$\text{pH} = \text{p}K - n \log \frac{1-\alpha}{\alpha}, \quad (3-2)$$

where K is the mean equilibrium constant and n is an empirical constant [15].

The acidic binding sites in HA are typically attributed to O-containing functional groups (mainly $-\text{COOH}$ and phenolic $-\text{OH}$ groups). Although other functional groups, such as N- and S-containing groups, could also participate in protonation, their contributions can be neglected because of their low content in HA [16]. Therefore, the MHHM can be used to describe the contributions of the $-\text{COOH}$ and phenolic $-\text{OH}$ binding sites as follows:

$$Q = \frac{Q_1}{1+(K_1[\text{H}^+])^{1/n_1}} + \frac{Q_2}{1+(K_2[\text{H}^+])^{1/n_2}} = \frac{Q_1}{1+10^{(\log K_1 - \text{pH})/n_1}} + \frac{Q_2}{1+10^{(\log K_2 - \text{pH})/n_2}}, \quad (3-3)$$

where Q (meq/g) is the amount of ionized functional groups per gram of organic carbon, and

could be obtained from the charge balance at every pH point during titration, Q_1 and Q_2 are the maximum capacities (meq/g) of $-\text{COOH}$ and phenolic $-\text{OH}$, respectively. K_1 and K_2 are the corresponding mean acid dissociation constants, and n_1 and n_2 are empirical constants reflecting the range of the equilibrium constants for the $-\text{COOH}$ and phenolic $-\text{OH}$ protonated sites, respectively [17, 18]. For more accurate and unique fitting results, the average $\log K_1$ and $\log K_2$ ranged between 3–6 and 8–11, respectively. Eq. 3-3 was fitted to the aggregated data sets of Q vs. pH, and the optimum set of Q_1 , $\log K_1$, n_1 , Q_2 , $\log K_2$, and n_2 fitting parameters for each sample was obtained using nonlinear regression to minimize the weighted sum of squared residuals. The best fitting Q_1 , Q_2 , $\log K_1$, $\log K_2$, n_1 , and n_2 values were determined using a non-linear custom function module in the Origin 2019 (Origin Lab, USA) data analysis software.

3.4 Results and discussion

3.4.1 Chemical characteristics of HA solution

The initial pH of the HA solution (7.9) decreased to 7.6, 7.2, 6.9, 6.4, and 5.8 after irradiation with 1, 5, 10, 50, and 100 kGy of gamma rays, respectively. As previously reported in the literature, a large amount of gas was distinctly observed when the sealed glass bottles were open, particularly for the 100 kGy gamma-irradiated samples [19, 20]. Seriesi et al. collected the gas produced during the gamma irradiation of HS samples and used a gas spectrometer to demonstrate that it mainly consisted of CO_2 and small amounts of CO and H_2 [21]. Therefore, the decrease in pH was probably due to the dissolution of CO_2 gas in the HA solution. The contribution of CO_2 to the decrease in pH was confirmed through degassing, as the pH increased to some extent after the HA solutions were bubbled with pure N_2 gas. Moreover, the decrease in pH might have been caused by the decrease in the acid dissociation constant of the acidic functional groups via the reaction between HA molecules

and radicals formed during water ionization. In addition, the logarithm of the absorbed dose (1–100 kGy) was approximately linearly related to the pH of the solution after radiolysis (**Fig. 3-2a**). However, the slope of the fitted line (0.81) was less than 1, which suggested that the amount of generated H^+ ions decreased as the radiation dose increased, and indicated the complexity of radiolysis reactions.

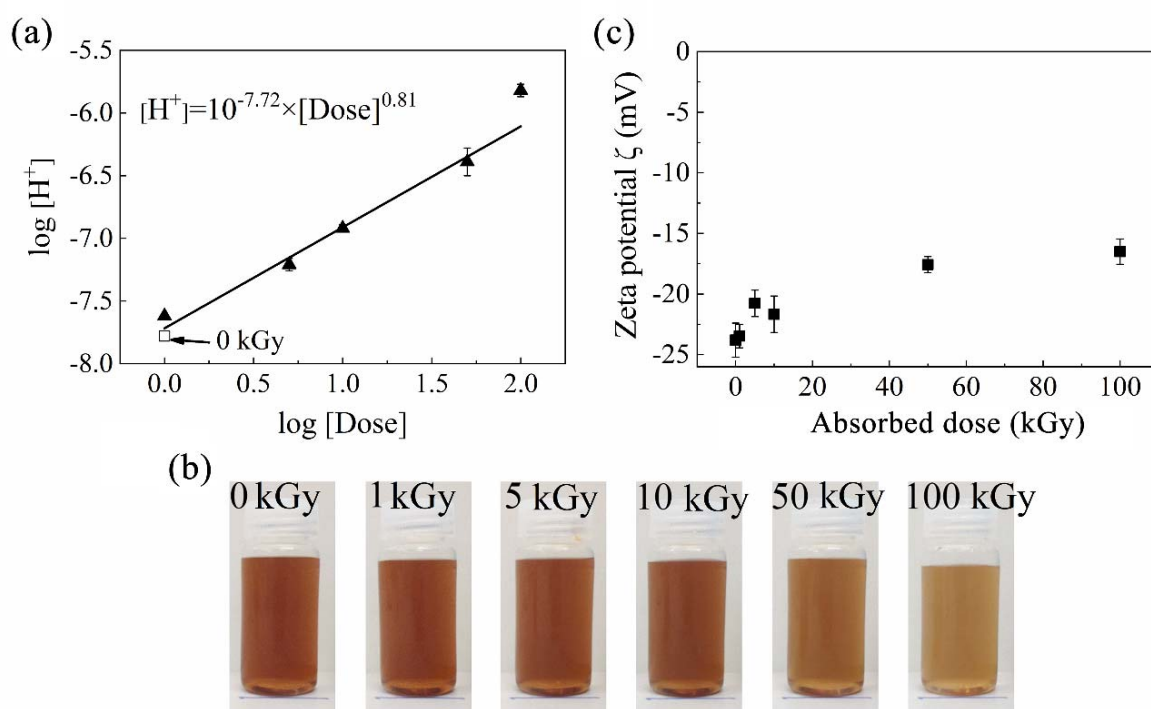


Fig. 3-2 (a) Logarithm dependence of absorbed dose on $[H^+]$; the square plot at 0 kGy is highlighted and the solid line represents the linear fitting relationship. (b) Color of humic acid (HA) solutions at different absorbed dose. (c) Dependence of absorbed dose on the zeta potential of HA samples (pH of 8, ionic strength of 0.05 mol/dm^3). The error bars indicate the standard deviations for three measurements.

The appearance of the HA samples after the pH was adjusted to 8 is illustrated in **Fig. 3-2b**. No precipitation was observed in the glass bottles at the absorbed dose range of 0–100 kGy. The initial HA solution (0 kGy) was dark brown because of the chromophore group

(conjugated double-bond system), which was responsible for the absorption of electromagnetic radiation in the visible light region [22]. The brownish color gradually became lighter with increasing absorbed dose, as previously reported [23], which suggested that decolorization was due to the destruction of the conjugated system within the HA molecules under the attack of radicals [24].

To evaluate the stability of colloids, zeta potential measurement is an effective method, which intrinsically evaluates the outer surface potential of colloids. At pH 8, the zeta potential values of the HA solution were always negative regardless of the absorbed dose (**Fig. 3-2c**). The negative zeta potential values were caused by the surface functional groups, such as the negatively charged carboxylic group ($-\text{COO}^-$) [25, 26]. As the absorbed dose increased, the zeta potential values of the HA solution increased toward zero. The decrease in absolute zeta potential could be attributed to the decrease in the density of functional groups on the HA molecules. The decrease in absolute zeta potential might facilitate the agglomeration and flocculation of HA molecules [27], although the changes in zeta potential were small.

3.4.2 Distribution of TOC in molecular-weight fractions

Fig. 3-3a illustrates the dependence of the absorbed dose on the molecular-weight-related TOC distribution. The TOC content of the HA solution decreased with increasing absorbed dose. It was hypothesized that the decrease in TOC was caused by decarburization into inorganic carbon, such as CO_2 gas. For the initial HA solution (0 kGy), the UF_3 fraction was predominant and contained the largest percentage of TOC (60 %), which was consistent with the previously reported data for Sigma-Aldrich-provided HA [28–30]. As the absorbed dose increased, the UF_4 fraction gradually became dominant, which suggested that large molecules degraded into smaller ones via the radiolytic degradation of HA molecules.

However, even at 100 kGy, the UF₁ fraction was still present. Therefore, high-dose gamma irradiation (100 kGy) did not completely eliminate the high molecular weight fractions of HA. The degradation of HA into small molecular weight fractions could be interpreted based on different structural definitions of HA, as follows. Typically, HA is considered to be a macromolecule; therefore, the random cleavage of the C–C bonds and ring-breakage of aromatic compounds under radical attack could be mainly attributed to decomposition, which has been previously observed in ¹³C nuclear magnetic resonance (NMR) spectra in **Section 2.4.4** [31]. Furthermore, the gamma-irradiation-induced decomposition of the aliphatic structures in some macromolecules, such as triglycerides [32] and polyethylene [33] has been reported. Conversely, some researchers have recently proposed that HA could be a supramolecule consisting of self-assembling, heterogeneous, and relatively small molecules held together by multiple weak interactions, such as hydrogen bonds and van der Waals forces [34]. The stabilization of the structure was mainly attributed to the hydrogen bonds and the intra- or intermolecular interactions between protonated functional groups, such as –COOH and phenolic –OH [35]. For this concept, the decomposition of functional groups, which act as hydrogen donors, would cause the decrease in the molecular weight of HA.

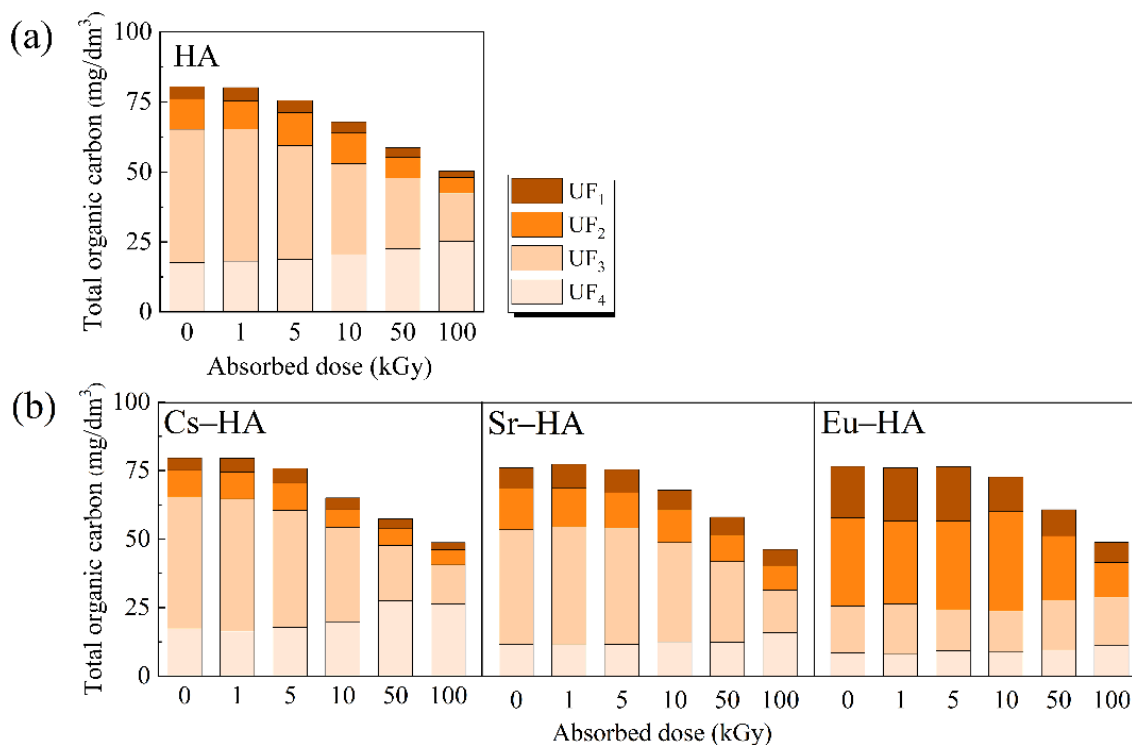


Fig. 3-3 Fractional distribution of total organic carbon in solution (ionic strength of 0.05 mol/dm³, pH of 8) with absorbed dose: **(a)** humic acid (HA) and **(b)** Cs–HA, Sr–HA, and Eu–HA systems. Here, UF₁, UF₂, UF₃, and UF₄ denote the >100, 50–100, 10–50, and <10 kDa nominal molecular weight limit fractions (dark to light in color), respectively.

3.4.3 Determination of –COOH and phenolic –OH group contents

The experimental titration data and the model-generated titration curves of HA are illustrated in **Fig. 3-4**. The fitting curves of Q vs. pH were in good agreement with the experimental data, and the “best fit” parameters that satisfactorily described the curves were obtained. The sum of Q values of UF₁₋₄ at a given pH was close to the Q of the non-filtrated one. The matrices of the best fitting parameters: Q_1 , $\log K_1$, n_1 , Q_2 , $\log K_2$, and n_2 are summarized in **Table 3-1**.

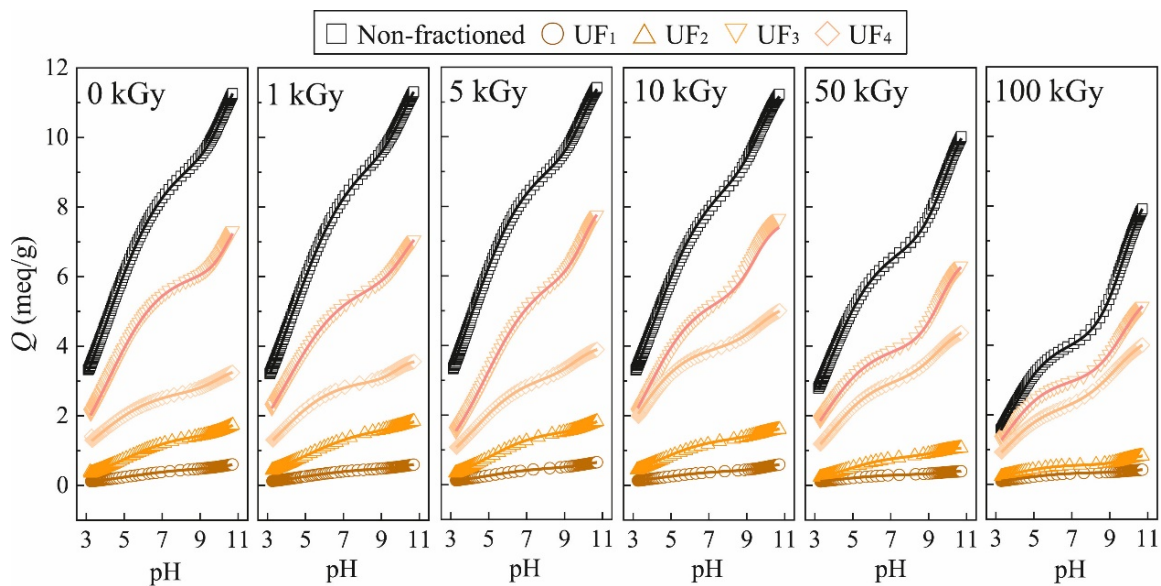


Fig. 3-4 Titration data points and their “best fit” Q vs. pH model curves of gamma-irradiated (0, 1, 5, 10, 50, 100 kGy) HA and its molecular weight fractions. Q denotes the organic charge density. Here, UF₁, UF₂, UF₃, and UF₄ denote the >100, 50–100, 10–50, and <10 kDa nominal molecular weight limit fractions, respectively.

Overall, the Q_1 (–COOH) and Q_2 (phenolic –OH) values in the non-fractionated HA decreased and increased with increasing absorbed dose, respectively, which indicated that gamma irradiation facilitated the decomposition of –COOH groups and the formation of phenolic –OH groups [31]. The decrease in Q_{tot} as the absorbed dose increased supported the decrease in the absolute zeta potential value, as discussed in **Section 3.4.1 (Fig. 3-2c)**. The sums of the –COOH and phenolic –OH contents in the four molecular weight fractions were slightly smaller than that of the non-filtrated original sample, probably because of a loss in residual HA during ultrafiltration. Nevertheless, the fractions with different molecular weights presented significantly different functional group properties. For the non-irradiated sample, the relative content ratio of –COOH to phenolic –OH groups ($D = Q_1/Q_2$) increased from UF₁ to UF₄, and the content of –COOH groups of the smaller molecular weight fractions was higher than that of the higher molecular weight fractions. Shin et al. analyzed

the molecular weight fraction using infrared spectroscopy and proposed that the –COOH groups were predominant in the smaller molecular weight fractions [28]. However, as the absorbed dose was increased, D gradually decreased in order from UF₁ to UF₄; namely, phenolic –OH groups would be predominant in the small molecular weight fractions obtained during the radiolytic degradation of HA. In addition, the mean $\log K_1$ and $\log K_2$ values for each molecular weight fraction decreased as the absorbed dose increased. This tendency could be attributed to the breaking of the intramolecular hydrogen bonds between multiple functional groups owing to the decomposition of the –COOH groups.

Although the current mechanism of the effects of gamma irradiation on HA is unclear, a possible HA degradation mechanism was proposed using TOC analysis, UV–Vis spectrometry, ¹³C NMR, and acid–base titration [31], which is deduced from the radiolysis mechanisms in other similar structures in **Section 2.4.5** [36, 37]. A simplified scheme of the process is illustrated in **Fig. 2-6**. The gamma-irradiation-induced process included the decarboxylation and hydroxylation of the molecule. In this study, the gamma-irradiation-induced shift in the distribution of phenolic –OH groups toward the small molecular weight fractions also supported the radiolysis mechanism.

Table 3-1 Optimized fitting parameters for humic acid (HA) samples and their fractions; here, UF₁₋₄ denote fractions with molecular weights of >100, 50–100, 10–50, and <10 kDa, respectively; Q_1 and Q_2 denote the maximum capacities of –COOH and phenolic –OH groups, respectively; K_1 and K_2 denote the mean acid dissociation constants of –COOH and phenolic –OH, respectively; n_1 and n_2 denote empirical constants reflecting the range of the equilibrium constants for the –COOH and phenolic –OH protonated sites, respectively; S denotes the sum of Q_1 or Q_2 for the UF₁–UF₄ fractions, Q_{tot} denotes the maximum capacity of proton-exchange sites ($= Q_1 + Q_2$), and D denotes the relative content ratio of –COOH to

phenolic –OH groups (= Q_1/Q_2).

Dose (kGy)	Q_1 (meq/g)	$\log K_1$	n_1	Q_2 (meq/g)	$\log K_2$	n_2	Q_{tot} (meq/g)	D
HA	11.03±0.21	4.21±0.09	3.57±0.13	3.76±0.18	10.28±0.04	1.36±0.06	14.79	2.93
S	10.68			3.47			14.15	
UF ₁	0.52±0.01	5.03±0.17	3.66±0.05	0.24±0.00	10.66±0.16	1.65±0.05	0.76	2.17
UF ₂	1.50±0.00	5.00±0.03	3.35±0.07	0.56±0.01	10.63±0.10	1.31±0.07	2.06	2.68
UF ₃	6.08±0.06	4.12±0.04	3.13±0.02	1.97±0.06	10.38±0.03	1.13±0.02	8.05	3.09
UF ₄	2.58±0.18	3.45±0.04	3.49±0.08	0.70±0.01	9.91±0.07	1.47±0.07	3.28	3.69
HA	10.94±0.18	4.34±0.08	3.65±0.04	3.55±0.12	10.31±0.06	1.53±0.03	14.49	3.08
S	10.85			3.07			13.92	
UF ₁	0.50±0.01	4.88±0.01	3.45±0.03	0.22±0.00	10.62±0.02	1.64±0.03	0.72	2.27
UF ₂	1.71±0.02	5.00±0.08	3.79±0.08	0.45±0.00	10.63±0.09	1.55±0.03	2.16	3.80
UF ₃	5.89±0.04	4.07±0.09	3.52±0.00	1.81±0.09	10.20±0.06	1.45±0.03	7.70	3.25
UF ₄	2.75±0.03	3.71±0.01	3.24±0.00	0.59±0.02	9.72±0.06	1.06±0.06	3.34	4.66
HA	10.53±0.11	4.14±0.09	3.45±0.01	3.75±0.08	10.07±0.08	1.40±0.01	14.28	2.81
S	10.59			3.48			14.07	
UF ₁	0.52±0.00	4.82±0.16	3.46±0.06	0.20±0.00	10.36±0.09	1.39±0.01	0.72	2.60
UF ₂	1.57±0.01	4.83±0.26	3.33±0.12	0.40±0.01	10.36±0.04	1.36±0.12	1.97	3.93
UF ₃	6.03±0.11	4.59±0.24	3.29±0.03	2.09±0.14	10.02±0.02	1.21±0.06	8.12	2.89
UF ₄	2.47±0.04	4.21±0.04	3.20±0.01	0.79±0.05	9.68±0.07	1.50±0.03	3.26	3.13
HA	10.06±0.12	3.93±0.08	3.58±0.04	3.72±0.13	9.79±0.01	1.49±0.14	13.78	2.70
S	9.84			4.16			14.00	
UF ₁	0.46±0.01	4.32±0.07	3.75±0.03	0.21±0.01	10.24±0.03	1.19±0.02	0.67	2.19
UF ₂	1.39±0.02	4.36±0.05	3.51±0.09	0.30±0.02	10.02±0.01	1.29±0.01	1.69	4.63
UF ₃	5.41±0.01	3.77±0.01	3.04±0.19	2.42±0.04	9.47±0.05	1.63±0.08	7.83	2.24
UF ₄	2.58±0.08	3.36±0.06	2.85±0.07	1.23±0.05	9.53±0.10	1.63±0.00	3.81	2.10

HA	7.78±0.10	3.67±0.02	3.00±0.04	5.09±0.08	9.75±0.11	1.65±0.04	12.87	1.53
S	7.07			4.60			11.67	
UF ₁	0.32±0.00	4.12±0.04	3.19±0.13	0.11±0.01	9.85±0.09	1.37±0.03	0.43	2.91
UF ₂	0.85±0.00	4.28±0.26	2.88±0.02	0.26±0.01	9.60±0.02	1.52±0.10	1.11	3.27
UF ₃	4.02±0.02	3.50±0.02	2.86±0.05	2.69±0.01	9.55±0.06	1.45±0.00	6.71	1.49
UF ₄	1.88±0.02	3.60±0.26	2.69±0.04	1.54±0.06	9.34±0.14	1.77±0.03	3.42	1.22
HA	5.82±0.14	3.67±0.07	2.44±0.10	5.87±0.05	9.62±0.11	1.70±0.04	11.69	0.99
S	5.39			5.39			10.78	
UF ₁	0.34±0.00	4.15±0.15	2.70±0.12	0.12±0.02	10.12±0.10	1.43±0.06	0.46	2.83
UF ₂	0.56±0.02	3.75±0.00	2.64±0.03	0.29±0.01	9.80±0.06	1.34±0.06	0.85	1.93
UF ₃	2.99±0.01	3.53±0.05	2.38±0.02	2.66±0.08	9.55±0.13	1.79±0.05	5.65	1.12
UF ₄	1.50±0.02	3.53±0.08	2.36±0.05	2.32±0.02	9.37±0.03	1.65±0.03	3.82	0.65

3.4.4 Distribution of Cs⁺, Sr²⁺, and Eu³⁺ ions in the metal–HA molecular weight fractions

The effect of metal ions on the distribution of the molecular weight fractions of HA is illustrated in **Fig. 3-3b**. The TOC of Cs–HA system was not significantly different from that of HA (**Fig. 3-3a**), as Cs⁺ ions did not change the molecular weight distribution of the total organic carbon content of non-irradiated HA. Conversely, the Sr²⁺ and Eu³⁺ ions have significantly shifted the distribution of organic carbon toward the larger molecular weight fractions of the non-irradiated metal–HA systems. Multivalent metal ions might attract several molecules as “bridging” metal cations [38, 39], which suggested that the following combinations would be possible: RCOO–M–OOCR, RCOO–M–OR, and RO–M–OR. By contrast, the same trend in the molecular weight distribution of organic carbon was observed for the irradiated HA and Cs–HA, Sr–HA, and Eu–HA systems, namely the amounts of organic carbon in the small and large molecular weight fractions increased and decreased, respectively with increasing absorbed dose.

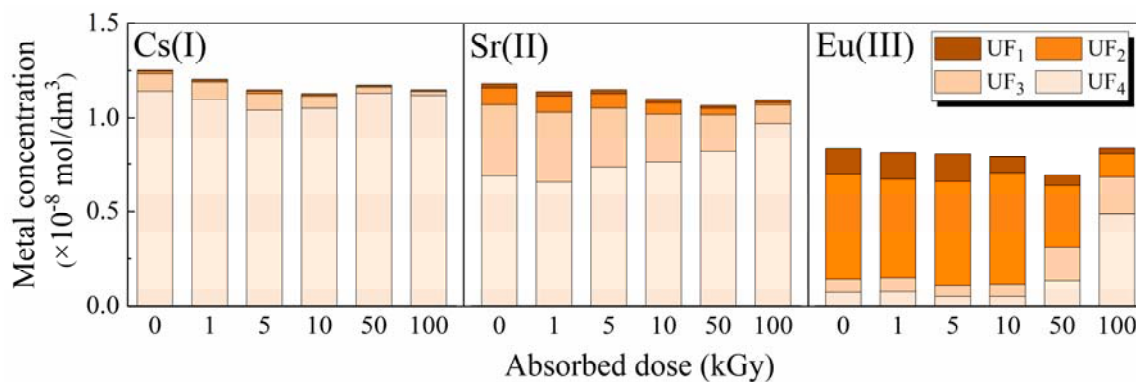


Fig. 3-5 Distributions of Cs(I), Sr(II), and Eu(III) in the molecular weight fractions of the metal–humic acid systems (pH of 8 and ionic strength of 0.05 mol/dm³). Here, UF₁, UF₂, UF₃, and UF₄ denote the >100, 50–100, 10–50, and <10 kDa nominal molecular weight limit fractions (dark to light in color), respectively.

Fig. 3-5 presents the distribution of Cs⁺, Sr²⁺, and Eu³⁺ ions in the molecular weight fractions of the metal–HA systems; the yield loss during ultrafiltration was excluded. For the non-irradiation systems, 90 % of Cs⁺ ions and 60 % of Sr²⁺ ions were present in the UF₄ fraction. The majority of Cs⁺ ions would be dissolved as free Cs⁺ ions at neutral pH, even in the presence of HA [40]. Norwegian mountain lake water analysis revealed that more than 50 % of Sr²⁺ ions were present in the UF₄ fraction of HS [41]. Furthermore, over 60 % of Eu³⁺ ions were present in the UF₂ fraction and only 10 % of Eu³⁺ ions were present in the UF₄ fraction of the non-irradiated Eu–HA system. Nagao et al. analyzed the distribution of Am(III) in the molecular weight fraction of Am–HA at pH 8–9, and suggested that the largest percentage of Am was present the 30–100 kDa molecular weight fraction [42]; these results matched the Eu distribution in this study. The different distributions of the Cs⁺, Sr²⁺, and Eu³⁺ ions in the molecular weight fractions of the metal–HA system were mainly attributed to the different chemical valence states of the metals. More Cs⁺, Sr²⁺, and Eu³⁺ ions were present in the small molecular weight fractions of the metal–HA systems as the absorbed dose increased. The changes in metal distribution were probably ascribed to two reasons.

First, the molecular weight of the HA molecule was radiolytically reduced, which was demonstrated by TOC measurements, thus the apparent molecular weight of the metal–HA complexes would also decrease. Second, the decrease in the maximum capacity of binding sites (Q_{tot}) led to a decrease in metal–HA complexes, and an increase in the fraction of free metal ions not complexed with HA. This has also been demonstrated in a previous study of a Ca–HS system using an ion-selective electrode [31]. However, the Q_1 and Q_2 values of HA (Section 3.4.3) were different than those of the Sr–HA and Eu–HA systems owing to the cation bridging effect. Therefore, it would be difficult to determine a straightforward relationship between Q_1 and Q_2 and the distributions of metal ions in the molecular weight fractions.

3.4.5 Dependence of the gamma irradiation with complexation affinity in molecular-weight fractions

Complexation affinity was defined as the amount of metal ions per gram of organic carbon, and is the ratio of the metal concentration to the TOC content in a given molecular weight fraction ($[M]/(c)$) [43]. The complexation affinities of the metal–HA systems in this study are summarized in **Table 3-2**. The affinity for the UF₄ fraction was not considered because free metal ions (not complexed with HA) were present in the UF₄ fraction. The complexation affinity of the Cs⁺ ions was lower than those of the Sr²⁺ and Eu³⁺ ions. The complexation affinities in a given molecular weight fraction decreased with the absorbed dose for all sample fractions except for the UF₃ fraction of the Eu–HA system. This indicated that gamma irradiation reduced the affinities of the molecular weight fractions of HA for metal ions. Christl proposed that the –COOH groups primarily controlled the binding of Ca with HA using titration experiments with Ca²⁺ ions [44]. Marang et al. suggested that Eu bound mainly to the –COOH-type groups and less to the phenolic –OH-type groups using

time-resolved laser induced luminescence spectroscopy [45]. The complexation affinity of HA for alkali earth metal and lanthanide ions would depend largely on the presence of –COOH groups. Therefore, the complexation affinities in the molecular weight fractions of the metal–HA systems might be reduced because of the decrease in Q_1 by radiolysis.

Table 3-2 Complexation affinities of the molecular weight fractions of humic acid for Cs⁺, Sr²⁺, and Eu³⁺ ions; here, [M] and c denote the concentration of metal and total organic carbon content, respectively, and UF₁₋₃ denote fractions with molecular weights of >100, 50–100, and 10–50 kDa, respectively.

Metal ions	[M]/(c) ($\times 10^{-8}$ mol/g)	Absorbed gamma irradiation dose (kGy)					
		0	1	5	10	50	100
Cs	UF ₁	0.89	0.86	0.86	0.84	0.80	0.78
	UF ₂	1.46	1.38	1.36	1.33	1.25	1.15
	UF ₃	1.96	1.95	2.01	1.80	1.52	1.47
Sr	UF ₁	3.00	2.95	2.78	2.78	2.55	1.80
	UF ₂	6.50	6.57	6.39	5.63	3.91	1.48
	UF ₃	10.1	9.63	8.33	7.97	7.40	7.28
Eu	UF ₁	8.21	8.17	8.24	7.62	6.07	4.68
	UF ₂	19.2	19.1	18.8	18.0	15.6	11.0
	UF ₃	4.46	4.43	4.37	4.73	10.8	12.5

The trend in complexation affinity of the UF₃ fraction for Eu in the Eu–HA system appears to be opposite to those of the Cs–HA and Sr–HA systems (**Table 3-2**). Sasaki et al. suggested that the apparent complex formation constant of HA with metal ions could depend on the abundance of several types of basic ligands in the chemical structure of HA. Each ligand presented negatively charged –COOH and phenolic –OH functional groups. Typically,

because the complexation affinity of ligands increases with increasing number of functional groups of the benzene ring [46], such stabilization of the complexation of HA with Eu^{3+} ions in the UF_3 fraction might be induced by a chelating effect. The chelating effect on the complexation of Eu–HA has been reported [47], while similar effects on complexation affinities were not observed for the Cs^+ and Sr^{2+} ions. Further investigation is needed to assign the chelate complexation of HA with multivalent metal ions.

3.5 Summary

The gamma irradiation (0–100 kGy) to the HA solution resulted in a change of the concentration of two major functional groups, $-\text{COOH}$ and phenolic $-\text{OH}$. Sequential ultrafiltration and chemical analyses showed that the concentration of $-\text{COOH}$ groups in all molecular weight fractions of non-irradiated HA was higher than that of phenolic $-\text{OH}$ groups. However, the phenolic $-\text{OH}$ groups became predominant in the small molecular weight fractions as the absorbed dose increased. The apparent molecular weight distribution of the total organic carbon content in the Cs–HA system was similar to that in pure HA. Moreover, gamma irradiation shifted the distribution of organic carbon in the Sr–HA and Eu–HA systems toward the large molecular weight fractions. Cs^+ , Sr^{2+} , and Eu^{3+} ions were mostly present in the small molecular weight fractions of the irradiated systems. In addition, complexation affinity data indicated that gamma irradiation reduced the complexation affinities for the Cs^+ , Sr^{2+} , and Eu^{3+} ions toward the UF_1 , UF_2 , and UF_3 fractions of the metal–HA systems maybe owing to the decrease in the content of $-\text{COOH}$ groups in all molecular weight fraction. Conversely, the complexation affinity of the UF_3 fraction of the Eu–HA system increased with increasing absorbed dose. One possible explanation might be the chelating effect induced by gamma irradiation stabilized metal–HA complexation, though a direct evidence is necessary in future study. In summary, the gamma irradiation

field in the vicinity of a highly radioactive waste package would alter the molecular weight of metal–HA complexes in groundwater. The effect of the gamma irradiation field should be considered for the assessment of the environmental behavior of radionuclides in nuclear hazard areas.

Reference

- [1] D. Alby, T. Charnay, M. Heran, B. Prelot, J. Zajac, Recent developments in nanostructured inorganic materials for sorption of cesium and strontium: Synthesis and shaping, sorption capacity, mechanisms, and selectivity—A review. *J. Hazard. Mater.* **344** (2018), 511–530.
- [2] A. Rump, B. Becker, S. Eder, A. Lamkowski, M. Abend, M. Port, Medical management of victims contaminated with radionuclides after a “dirty bomb” attack. *Mil. Med. Res.* **5** (2018), 1–10.
- [3] R. Artinger, B. Kienzler, W. Schußler, J.L. Kim, Effects of humic substances on the ²⁴¹Am migration in a sandy aquifer: column experiments with Gorleben groundwater/sediment systems. *J. Contam. Hydrol.* **35** (1998), 261–275.
- [4] M. Havelcová, J. Mizera, I. Sýkorová, M. Pekař, Sorption of metal ions on lignite and the derived humic substances. *J. Hazard. Mater.* **161** (2009), 559–564.
- [5] J.F. McCarthy, K.R. Czerwinski, W.E. Sanford, P.M. Jardine, J.D. Marsh, Mobilization of transuranic radionuclides from disposal trenches by natural organic matter. *J. Contam. Hydrol.* **30** (1998), 49–77.
- [6] J.F. McCarthy, B. Gu, L. Liang, J. Mas-Pla, T.M. Williams, T.C.J. Yeh, Field tracer tests on the mobility of natural organic matter in a sandy aquifer. *Water Resour. Res.* **32** (1996), 1223–1238.
- [7] I. Baek, W.W. Pitt, Colloid-facilitated radionuclide transport in fractured porous rock. *Waste Manag.* **16** (1996), 313–325.
- [8] C.P. Jen, S.H. Li, Effects of hydrodynamic chromatography on colloid-facilitated migration of radionuclides in the fractured rock. *Waste Manag.* **21** (2001), 499–509.
- [9] K. James, W.J. Weber, Transport and separation of organic macromolecules in ultrafiltration processes. *Environ. Sci. Technol.* **26** (1992), 569–577.

- [10] H. Kunimaru, T., Ota, K., Alexander, W. Russell, H. Yamamoto, Groundwater/porewater hydrochemistry at Horonobe URL: Data freeze 1. Preliminary data quality evaluation for boreholes HDB-9, 10 and 11, JAEA-Research-2010-035, Japan Atomic Energy Agency (2010), p107.
- [11] Y. Ai, C. Zhao, L. Sun, X. Wang, L. Liang, Coagulation mechanisms of humic acid in metal ions solution under different pH conditions: A molecular dynamics simulation, *Sci. Total Environ.* **702** (2020), 135072.
- [12] Malvern Instruments Ltd., Zetasizer nano series user manual, Malvern Instruments Ltd., 2004, MAN0317.
- [13] D.R. Lide, W.M.M. Haynes, G. Baysinger, L.I. Berger, H. V Kehiaian, D.L. Roth, K. Kuchitsu, D. Zwillinger, M. Frenkel, R.N. Goldberg, CRC Handbook of Chemistry and Physics, 90th Ed., *J. Am. Chem. Soc.*, 2009.
- [14] International humic substances society. Acidic functional groups of IHSS samples. Retrieved October 4, 2021, from <https://humic-substances.org/acidic-functional-groups-of-ihss-samples/>
- [15] J. Reijenga, A. van Hoof, A. van Loon, B. Teunissen, Development of methods for the determination of pK_a values, *Anal. Chem. Insights* **8** (2013), 53–71.
- [16] S. Yan, N. Zhang, J. Li, Y. Wang, Y. Liu, M. Cao, Q. Yan, Characterization of humic acids from original coal and its oxidization production, *Sci. Rep.* **11** (2021), 1–10.
- [17] S.J. Driver, E.M. Perdue, Acidic functional groups of suwannee river natural organic matter, humic acids, and fulvic acids, in: Advances in the physicochemical characterization of dissolved organic matter: impact on natural and engineered systems. American Chemical Society (2014), 75–86.
- [18] J.D. Ritchie, E. Michael Perdue, Proton-binding study of standard and reference fulvic acids, humic acids, and natural organic matter, *Geochim. Cosmochim. Acta* **67** (2003),

- 85–93.
- [19] W.T.L. da Silva, S.C. da Silva, M.O. de O. Rezende, Influence of gamma-radiation on the behavior of humic acids from peat and tropical soil, *J. Radioanal. Nucl. Chem.* **222** (1997), 29–34.
- [20] W. Goraczko, J. Slawiński, K. Staninski, Spectral distribution of the radiochemiluminescence from gamma-irradiated humic acid, *J. Radioanal. Nucl. Chem.* **277** (2008), 613–618.
- [21] N. Seriesi, Y. Chen, M. Schnitzer, The electron- and γ -irradiation of humic substances, *Fuel* **56** (1977), 171–176.
- [22] M.A. Rahman Bhuiyan, A. Shaid, M.A. Hossain, M.A. Khan, Decolorization and decontamination of textile wastewater by gamma irradiation in presence of H₂O₂, *Desalin. Water Treat.* **57** (2016), 21545–21551.
- [23] T. Sasaki, R. Goto, T. Saito, T. Kobayashi, T. Ikuji, Y. Sugiyama, Gamma-ray irradiation impact of humic substances on apparent formation constants with Cu(II), *J. Nucl. Sci. Technol.* **55** (2018), 1299–1308.
- [24] W. Andayani, A.N.M. Bagyo, Radiation-induced decomposition and decolorization of water in aerated solutions, *Radiat. Phys. Chem.* **65** (2002), 447–450.
- [25] M.R. Esfahani, H.A. Stretz, M.J.M. Wells, Abiotic reversible self-assembly of fulvic and humic acid aggregates in low electrolytic conductivity solutions by dynamic light scattering and zeta potential investigation, *Sci. Total Environ.* **537** (2015), 81–92.
- [26] J.S. Park, H.J. Lee, S.J. Choi, K.E. Geckeler, J. Cho, S.H. Moon, Fouling mitigation of anion exchange membrane by zeta potential control, *J. Colloid Interface Sci.* **259** (2003), 293–300.
- [27] D. Hanaor, M. Michelazzi, C. Leonelli, C.C. Sorrell, The effects of carboxylic acids on the aqueous dispersion and electrophoretic deposition of ZrO₂, *J. Eur. Ceram. Soc.*

- 32** (2012), 235–244.
- [28] H.S. Shin, J.M. Monsallier, G.R. Choppin, Spectroscopic and chemical characterizations of molecular size fractionated humic acid, *Talanta* **50** (1999), 641–647.
- [29] M.E.A. El-sayed, M.M.R. Khalaf, D. Gibson, J.A. Rice, Assessment of clay mineral selectivity for adsorption of aliphatic/aromatic humic acid fraction, *Chem. Geol.* **511** (2019), 21–27.
- [30] I. Guardado, O. Urrutia, J.M. García-Mina, Size distribution, complexing capacity, and stability of phosphate–metal–humic complexes, *J. Agric. Food Chem.* **55** (2007), 408–413.
- [31] Q. Zhao, R. Goto, T. Saito, T. Kobayashi, T. Sasaki, Effect of gamma-irradiation on complexation of humic substances with divalent calcium ion, *Chemosphere* **256** (2020), 127021.
- [32] M.F. Dubravcic, W.W. Nawar, Radiolysis of lipids: Mode of cleavage in simple triglycerides, *J. Am. Oil Chem. Soc.* **45** (1968), 656–660.
- [33] F.J. Medel, F. García-Álvarez, E. Gómez-Barrena, J.A. Puértolas, Microstructure changes of extruded ultra high molecular weight polyethylene after gamma irradiation and shelf-aging, *Polym. Degrad. Stab.* **88** (2005), 435–443.
- [34] A. Nebbioso, A. Piccolo, Advances in humeomics: Enhanced structural identification of humic molecules after size fractionation of a soil humic acid, *Anal. Chim. Acta* **720** (2012), 77–90.
- [35] J. Pertusatti, A.G.S. Prado, Buffer capacity of humic acid: thermodynamic approach, *J. Colloid Interface Sci.* **314** (2007), 484–489.
- [36] A.R. Jones, The radiolysis of aliphatic carboxylic acids. On the decarboxylation of normal acids in the liquid state, *Radiat. Res.* **48** (1971), 447–453.

- [37] E. Brillas, M.Á. Baños, M. Skoumal, P.L. Cabot, J.A. Garrido, R.M. Rodríguez, Degradation of the herbicide 2, 4-DP by anodic oxidation, electro-Fenton and photoelectro-Fenton using platinum and boron-doped diamond anodes, *Chemosphere* **68** (2007), 199–209.
- [38] L. Tan, X. Tan, H. Mei, Y. Ai, L. Sun, G. Zhao, T. Hayat, A. Alsaedi, C. Chen, X. Wang, Coagulation behavior of humic acid in aqueous solutions containing Cs⁺, Sr²⁺ and Eu³⁺: DLS, EEM and MD simulations, *Environ. Pollut.* **236** (2018), 835–843.
- [39] A. Rodrigues, A. Brito, P. Janknecht, M.F. Proena, R. Nogueira, Quantification of humic acids in surface water: Effects of divalent cations, pH, and filtration, *J. Environ. Monit.* **11** (2009), 377–382.
- [40] S. Kumar, B.S. Tomar, S. Ramanathan, V.K. Manchanda, Effect of humic acid on cesium sorption on silica colloids, *Radiochim. Acta* **94** (2006), 369–373.
- [41] B. Salbu, H. Bjørnstad, J. Brittain, Fractionation of cesium isotopes and ⁹⁰Sr in snowmelt run-off and lake waters from a contaminated Norwegian mountain catchment, *J. Radioanal. Nucl. Chem.* **156** (1992), 7–20.
- [42] S. Nagao, N. Fujitake, H. Kodama, T. Matsunaga, H. Yamazawa, Association of Am with humic substances isolated from river waters with different water quality, *J. Radioanal. Nucl. Chem.* **255** (2003), 459–464.
- [43] T. Matsunaga, S. Nagao, T. Ueno, S. Takeda, H. Amano, Y. Tkachenko, Association of dissolved radionuclides released by the Chernobyl accident with colloidal materials in surface water, *Appl. Geochemistry* **19** (2004), 1581–1599.
- [44] I. Christl, Ionic strength- and pH-dependence of calcium binding by terrestrial humic acids, *Environ. Chem.* **9** (2012), 89–96.
- [45] L. Marang, S. Eidner, M.U. Kumke, M.F. Benedetti, P.E. Reiller, Spectroscopic characterization of the competitive binding of Eu(III), Ca(II), and Cu(II) to a

- sedimentary originated humic acid, *Chem. Geol.* **264** (2009), 154–161.
- [46] T. Sasaki, H. Yoshida, S. Aoyama, T. Kobayashi, I. Takagi, H. Moriyama, Discrete fragment model for apparent formation constants of actinide ions with humic substances, *Radiochim. Acta* **103** (2015), 411–421.
- [47] C. Möser, R. Kautenburger, H. Philipp Beck, Complexation of europium and uranium by humic acids analyzed by capillary electrophoresis-inductively coupled plasma mass spectrometry, *Electrophoresis* **33** (2012), 1482–1487.

Chapter 4 Sorption of Cs^+ and Eu^{3+} ions onto sedimentary rock in the presence of gamma-irradiated humic acid

4.1 Introduction

Although the possibility of HLW packaging failure is very unlikely after repository closure, the radionuclides would probably leach by groundwater media from the fractured waste packages, then would migrate to the biosphere. Therefore, the environmental behavior of radionuclides in the groundwater is quite important in the assessment of nuclear safety. Generally, the natural barrier, that is the host rock in the siting of GDF (as described in **Section 1.3.1**) could sorb various metal ions in the groundwater predominantly by cation exchange, surface complexation, or electrostatic interactions [1, 2], which delays the transport of nuclides [3, 4]. However, the presence of anionic HA molecules causes the formation of metal–HA complexes, which disturbs the sorption of metal ions due to its negative or neutral formal charge [5]. Therefore, the understanding of metal sorption in the presence of HA has been indispensable to investigating the migration behavior of nuclides, but few quantitative studies have been conducted. Moreover, the dependence of the sorption behavior of HA and nuclides on the gamma irradiation dose has not been adequately emphasized and explained.

In this study, the solid sorbent used was the sedimentary rock samples obtained from 140 m depth at the Horonobe URL, where the sedimentary rock contains clay minerals with a unique sorption capacity for Cs [6]. Batch sorption experiments were conducted to study the sorption coefficients of gamma-irradiated HA and Cs^+ and Eu^{3+} as typical mono- and tri-valent cations in nuclear waste. In addition, in the event of a nuclear containment failure, radionuclide ions would first contact HA molecules in the groundwater, followed by the sorption reaction of the host rock in the migration pathway. Therefore, the aging effect of

the irradiated HA-metal interaction on sorption was also discussed.

4.2 Materials and methods

4.2.1 Collection of sedimentary rock samples

JAEA has implemented numerous investigations at the Horonobe area in Hokkaido, Japan, to develop geological disposal technologies appropriate in sedimentary environments as part of HLW disposal program [7]. The Horonobe URL has been constructed, and is planned to be operated over a period of about 20 years. The Horonobe URL site is located on the eastern margin of a Neogene to the Quaternary sedimentary basin on the western side of northern Hokkaido [8], where is about 50 km south of the town of Wakkanai (**Fig. 4-1a**). It is situated in a low-lying coastal plain where Quaternary alluvium and terrace deposits overlie Tertiary and Cretaceous sediments that were deposited within the Tempoku Basin. The URL lies within Neogene strata, which unconformable overlie Paleogene sediments. The Neogene rocks include the Miocene Onishibetsu, Masuporo and Wakkanai formations, and the Pliocene Koetoi Formation [9]. The Wakkanai and Koetoi formations are target rocks for investigation in the Horonobe URL.

Sedimentary rock samples in a drillcore were acquired from a borehole drilled in the diatomaceous mudstone of the Koetoi Formation from the 140 m underground gallery (140 m below the ground surface, #08-E140-C01) at the Horonobe URL (**Fig. 4-1b**). The detailed geological setting and hydraulic conditions around the Horonobe URL are described by Hama et al. [10]. The brittle sample was crushed to 30–60 mesh (0.25–0.59 mm, theoretically) and then stored in a sealed bottle. No additional treatments were performed on the samples.

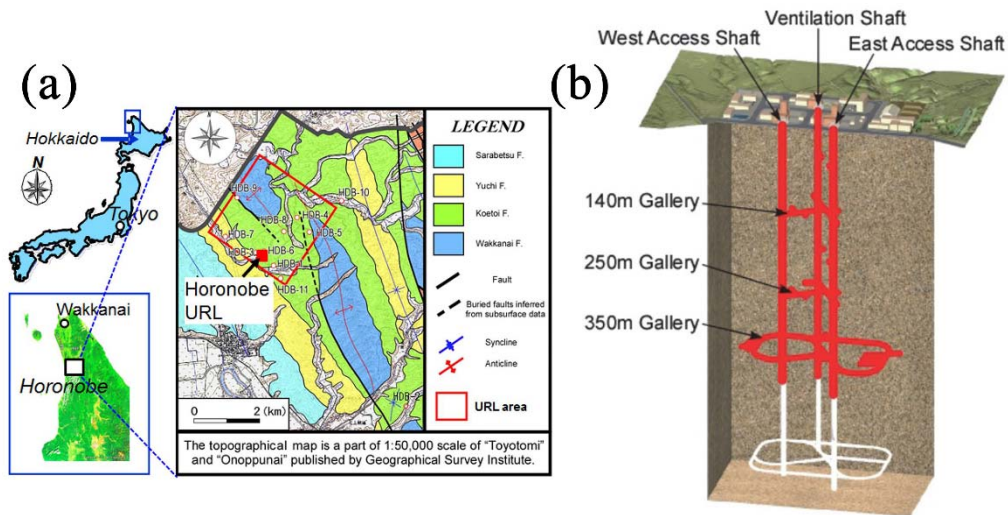


Fig. 4-1 (a) Geological map of the Horonobe region showing the location of the URL site and boreholes HDB-1 to HDB-11 [11]; (b) Diagram of the Horonobe Underground Research Facility. Red-colored shafts and galleries have already been excavated as of April 2015. This layout may be changed depending on the results of further investigation [12].

4.2.2 Characterization methods of sedimentary rock samples

4.2.2.1 X-ray powder spectra

X-ray powder diffraction (XRD) of the Horonobe underground minerals was performed using a MiniFlex 600 X-ray diffractometer (Rigaku Co., Japan) equipped with a rotating table. A Cu K α X-ray source ($\lambda = 0.154$ nm) was used at 40 kV and 15 mV. Data were collected from 5° to 90° (2 θ) with a scan speed of 1°/min. The solid samples were pre-treated by washing ultrasonically with pure water and ethanol before XRD analysis. This step removes the mud and organic matter in the solid samples, and improves the diffraction characteristics.

4.2.2.2 Scanning electron microscopy with X-ray microanalysis system

The morphology and microstructures of the mineral samples were characterized by scanning electron microscopy (SEM) using a JCM-6000 Versatile Benchtop SEM (JEOL,

Japan). The secondary electron imaging mode was used for SE imaging at an accelerating voltage of 15 kV. Semi-quantitative analysis of the mineral composition was performed using an energy-dispersive X-ray microanalysis system (EDX) using an MP-00040EDAP instrument.

4.2.2.3 Determination of external specific surface area

The external specific surface area of the crushed powder sample was determined by the multi-point N₂-sorption method using a BELSORP-MINI2 analyzer (MICROTRAC, Japan). Mineral samples (0.34 g) were dried at 110 °C for 5 h for outgassing. Then, the test sample was measured by calculating the sorption amount of gas corresponding to a monomolecular layer on the surface at the temperature of liquid N₂ (77 K). The sorption isotherms were evaluated for the solid surface area using the standard Brunauer–Emmett–Teller (BET) method using the instrument software [13].

4.2.2.4 Determination of point of zero charge

Potentiometric titrations were performed using an AT-510 (KEM, Japan) automatic potentiometric titration instrument to determine the point of zero charge (PZC) of the Horonobe mineral surface. Solid samples (0.2 g) were added to 20 mL aqueous solution. The pH and ionic strength *I* were adjusted to 3 and 0.05 by the addition of 0.1 mol/dm³ HCl and NaCl. After equilibration for 12 h, the solution was titrated with 0.01 mol/dm³ NaOH solution (Wako, Japan) with a constant stirring speed of 200 rpm at 298 K. After each titrant aliquot, the volume of titrant and pH were automatically recorded when the reading stabilized below ± 0.1 mV/s. Then, the surface charge density of the crushed sample could be determined from the potentiometric titration data using the following equation (**Eq. 4-1**):

$$\sigma = F \frac{(V_a C_a - V_b C_b) - ([H^+] - [OH^-])(V_a + V_b + V_i)}{mS}, \quad (4-1)$$

where σ is the surface charge density (C/m²), and F is the Faraday constant (96485 C/mol). V_a , V_b , and V_i are the volumes (L) of the added acid, titrant, and initial solution, respectively. C_a and C_b are the concentrations (mol/dm³) of the acid–base titrant, respectively. $[H^+]$ was assumed to be the direct measurement of the H⁺ ion activity, and $[OH^-]$ was calculated using the ionic product constant of water (pK_w) at 298 K [14], where m and S refer to the mass (g) and specific surface area (m²/g) of the samples, respectively. The surface charge densities are plotted versus the solution pH, and the PZC is the pH value when the surface charge density is equal to zero [15]. The measurements were performed in triplicate.

4.2.2.5 Dissolution of natural organic components, Cs⁺ and Eu³⁺ ions from crushed sedimentary

To check the dissolved natural organic carbon components, Cs⁺ and Eu³⁺ ions in the Horonobe sedimentary rock, the rock sample was soaked in pure water for 1 month, the TOC and concentration of Cs⁺ and Eu³⁺ ions in the supernatant were measured using a TOC analyzer and ICP-MS, respectively.

4.2.3 Preparation and characterization of irradiated HA solution

The purified HA is prepared and gamma-irradiated as same as described in **Section 3.2.1**. In this study, the temperature of gamma irradiation was about 15 °C. The applied doses of gamma rays at an approximate dose rate of 0.62 kGy/h were 10, 50, and 100 kGy, respectively. The characterization methods of TOC content and acidic functional groups in HA solution can be referred to **Section 3.2.3**.

4.2.4 Sorption experiment

The pH of the irradiated HA solution ($I = 0.05 \text{ mol/dm}^3$) was adjusted to 8 using NaOH. The stock metal solution (CsCl, EuCl₃) was added to the HA solution to obtain an initial metal concentration of approximately $1 \times 10^{-8} \text{ mol/dm}^3$. The sediment rock powder ($0.020 \pm 0.001 \text{ g}$) was weighed and transferred into a polycarbonate (PC) tube. The metal–HA solutions were either not aged or aged for 2 months prior to the following sorption experiment, named as the “co-sorption” and “pre-contact” system, respectively. The solution (10 mL) was injected into the PC tube corresponding to a liquid-to-solid ratio (L/S) of $0.5 \text{ m}^3/\text{kg}$. Blank solutions without HA or metal ions were prepared under the same conditions of pH and I for comparison. All sample tubes were placed horizontally and shaken at a constant rate of 70 rotations per minute and maintained at 298 K in an isothermal shaker (BR-43FL, Taitec Co., Ltd., Japan). The pH values were monitored and adjusted periodically with a small amount of NaOH when the pH shifted to greater than 8.0 ± 0.3 . After a contact time of 1 month, the supernatant was filtered through a membrane filter (pore size of $0.20 \text{ }\mu\text{m}$) (HP020AN, Advantec, Japan). The filtrates were analyzed using a TOC analyzer and ICP-MS for TOC and metal concentrations, respectively. For comparison, the metal concentration of the filtrate was measured by ICP-MS after using a 10 kDa (UFC901024, Amicon, Ireland) pore size filter. For reproducibility, three sets of samples were repeated under identical conditions. Recovery experiments were also carried out for the loss of HA and metal ions in the metal–HA system using a $0.20 \text{ }\mu\text{m}$ pore size filter under the same experimental conditions. In addition, the dissolution of HA, Cs⁺, and Eu³⁺ ions from the crushed rock samples of the Koetoi Formation was evaluated.

4.3 Theoretical

The filtration process separates the species into liquid and solid phases as described

above. The general sorption coefficients (m^3/kg) of HA (K_{d_HA}) and metal ions (K_{d_M}) are defined as follows (**Eqs. 4-2 and 4-3**):

$$K_{d_HA} = \frac{(C_{org})_i - (C_{org})_l}{(C_{org})_l} \frac{V}{m} = \frac{(C_{org})_s}{(C_{org})_l} \frac{V}{m}, \quad (4-2)$$

$$K_{d_M} = \frac{[M]_i - [M]_l}{[M]_l} \frac{V}{m} = \frac{[M]_s}{[M]_l} \frac{V}{m}, \quad (4-3)$$

where (C_{org}) and $[M]$ are the TOC (mg/dm^3) and metal ion concentration (mol/dm^3), with parentheses and square brackets, respectively. V (m^3) is the volume of the solution, m (kg) is the solid weight, and V/m is the liquid-to-solid ratio L/S, which is $0.5 \text{ m}^3/\text{kg}$ in this study. The subscripts i, l, and s, represent the initial, liquid, and solid phases, respectively. The initial concentration ($1 \times 10^{-8} \text{ mol}/\text{dm}^3$) of Eu was lower than the theoretical solubility limit, where the solubility product (K_{sp}) of $\text{Eu}(\text{OH})_3$ at $I = 0.05 \text{ mol}/\text{dm}^3$ was corrected to be 1.16×10^{-23} by the specific ion interaction theory (SIT) [16]. Therefore, the precipitation and suspension of $\text{Eu}(\text{OH})_3$ were negligible in the liquid phase. Based on this definition, the total concentrations of metal ions in the liquid and solid phases can be defined by **Eqs. 4-4 and 4-5**, respectively.

$$[M]_l = [M]_{\text{free}} + [M]_{\text{ML}} + [M]_{\text{MHA}}, \quad (4-4)$$

$$[M]_s = [M]_{\text{SO-M}} + [M]_{\text{SO-MHA}} + [M]_{\text{SO-ML}} + [M]_{\text{aggr}}, \quad (4-5)$$

where the subscripts free, ML, MHA, SO-M, SO-ML, SO-MHA, and aggr represent the free metal ion, metal ion complexed with a (mainly decomposed) fragmental ligand L (defined as $< 10 \text{ kDa}$) and a macromolecule HA ($> 10 \text{ kDa}$), metal ion sorbed on the rock sample, metal-L complex ($< 10 \text{ kDa}$) and metal-HA complex ($> 10 \text{ kDa}$), sorbed on the rock sample, and highly aggregated metal-HA compound ($> 0.20 \mu\text{m}$), respectively. Here, $[M]_{\text{MHA}}$ can be determined by the difference of metal concentration filtered by $0.20 \mu\text{m}$ and

10 kDa.

In the absence of a rock sample and HA, the predominant species of free $[M]_{\text{free}}$ in **Eq. 4-4** would be mononuclear hydroxides, Eu^{3+} , and $\text{Eu}(\text{OH})^{2+}$, which are smaller than the pore size of the 10 kDa filter (corresponding to 1.4 nm in diameter). When adding the non-irradiated HA ($<0.20 \mu\text{m}$) into the Cs and Eu solutions (pH 8, $I = 0.05 \text{ mol/dm}^3$), the recovery factor of organic carbon (as $(C_{\text{org}})_f / (C_{\text{org}})_i$) and metal ion (as $[M]_f / [M]_i$) in the filtered solutions (0.20 μm filter) was 97–102 % for Cs, 94–101 % for the organic carbon of HA in the Cs–HA system, 86–98 % for Eu, and 89–104 % for that of HA in the Eu–HA system, respectively. The quantitative recovery suggests that no aggregation was observed for metal ions, HA, and its metal–HA complexes, which were larger than 0.20 μm . Hence, the $[M]_{\text{aggr}}$ in **Eq. 4-5** was negligible in the present study. The concentration of metal ions sorbed on the rock sample would be regarded as that of the solid phase because the size of the sedimentary rock sample was in the submillimeter order ($\gg 0.20 \mu\text{m}$), as shown in **Section 4.2.1**. Therefore, in the absence of HA, the distribution coefficient K_{d_M} is defined as **Eq. 4-6**:

$$K_{d,1_M} = \frac{[M]_{\text{SO-M}} V}{[M]_{\text{free}} m}, \quad (4-6)$$

and the K_{d_M} in the presence of HA can be expressed as **Eq. 4-7**:

$$K_{d,2_M} = \frac{[M]_{\text{SO-M}} + [M]_{\text{SO-MHA}} + [M]_{\text{SO-ML}} V}{[M]_{\text{free}} + [M]_{\text{ML}} + [M]_{\text{MHA}} m}, \quad (4-7)$$

It should be noted that the ratio of the metal concentration of a metal complexed with HA to that of a non-complexed one would change because of the various solution conditions, which are $\alpha_l = ([M]_{\text{MHA}} + [M]_{\text{ML}}) / [M]_{\text{free}}$ in the liquid phase, and $\alpha_s = ([M]_{\text{SO-MHA}} + [M]_{\text{SO-ML}}) / [M]_{\text{SO-M}}$ in the solid phase, as discussed later.

The radiolytic reduction of the apparent molecular weight of the HA molecule and the metal–HA complexes was suggested by the TOC measurement, which has been

discussed in the previous study [17, 18]. As summarized in **Table 4-1**, the ratio of (C_{org}) in the <10 kDa fraction to that in the non-filtered HA solution was approximately 21 % and 50 % for the non-irradiated and 100 kGy irradiated solutions, respectively. In addition, the maximum capacity of protonation exchange sites (Q_1 and Q_2 values, corresponding to the content (meq/g C) of the $-COOH$ and phenolic $-OH$ groups, respectively) in the < 10 kDa fraction, was determined by acid–base titration in a previous study [18]. The ratio of $Q_1 + Q_2$ in the < 10 kDa fraction to that in the original HA solution showed a similar trend of 23 % and 35 %, respectively.

Table 4-1 Comparison of the ratio of TOC content, capacity, and metal content in the <10 kDa fraction to the non-filtered fraction

System	Dose (kGy)	TOC ratio (%)	Maximum capacity ratio ($Q_1 + Q_2$, %)	Metal content ratio (%)
HA only	0	21	23	
	100	50	35	
Cs-HA	0	22		90
	100	54		97
Eu-HA	0	11		9
	100	23		58

In the Cs–HA system, the solution was fractionated by a 10 kDa pore size filter. No significant difference was observed in the percentage (22 % and 54 %) TOC compared to those in the HA system above (21 % and 50 %). Moreover, the ratio of the Cs^+ concentration in the < 10 kDa fraction was as high as 90 % and 97 % in both the non-irradiated and 100 kGy irradiated solutions, respectively, suggesting that the aggregation and complexation affinity of HA and ligand, L, to the monovalent Cs^+ would be insignificant. However, the

Eu–HA fractionated solution indicated 11 % and 23 % TOC and only 9 % and 58 % Eu^{3+} in the <10 kDa fractions of non-irradiated and 100 kGy irradiated solutions, respectively. With increasing absorbed irradiation dose, however, the percentage for the 100 kGy irradiated solution increased due to the decomposition of HA molecules to the smaller fragmental ligands L, which might result in a lower complexation affinity due to the decrease in the degree of intramolecular multidentate coordination of ligands [19]. Thus, a significant difference in the distribution of Cs^+ and Eu^{3+} between these fractions was observed, probably due to the different electrostatic interactions of metal ions with HA and L under the solution conditions of the present study.

A direct spectroscopic study of HA by C_{1s} near-edge X-ray absorption fine structure spectroscopy proposed that the smaller-molecular-weight HA molecule mainly consists of the fragmented component of ligands such as phthalic acid (B12) and salicylic acid (HSal) [20], which has also been suggested by a model analysis [19]. Therefore, simply assuming that these components of B12 and HSal were regarded as a typical L in the <10 kDa fraction, the distribution of $[\text{M}]_{\text{free}}$ and $[\text{M}]_{\text{ML}}$ can be estimated using a chemical equilibrium model (visual MINTEQ ver. 3.1, KTH, Sweden) under a given solution condition. The $\log \beta$ values for Eu–B12 (4.73), Eu–HSal (2.60), and Eu–OH (6.21) were included in the software [21]. The input parameters required to calculate the distribution were pH (8.0), I (NaCl, 0.05 mol/dm³), temperature (298 K), $[\text{M}]_i$, metal concentration in the <10 kDa fraction, and the concentration of ligand $[\text{L}]_i$. The $[\text{L}]_i$ (eq/dm³) for B12 and HSal were calculated using the following two equations (**Eqs. 4-8a** and **b**) based on the concentration balance of –COOH and phenolic –OH, respectively. The estimated concentrations of metal ions and organic ligands, and metal speciation are summarized in **Table 4-2**.

$$Q_1 \times (C_{\text{org}})_{10\text{kDa}} \times 10^{-6} = 2[\text{B12}]_i + [\text{HSal}]_i, \quad (4-8a)$$

$$Q_2 \times (C_{\text{org}})_{10\text{kDa}} \times 10^{-6} = [\text{HSal}]_i, \quad (4-8b)$$

where the values of Q_1 and Q_2 , $-\text{COOH}$ and phenolic $-\text{OH}$, are determined in **Section 4.4.2**, and the $(C_{\text{org}})_{10\text{kDa}}$ in the <10 kDa fractions for the Cs and Eu systems was calculated based on the TOC ratio of the <10 kDa fraction to the non-fractionated HA solution (**Table 4-1**).

Table 4-2 Estimated logarithmic concentration (mol/dm^3) of metal species in the <10 kDa fraction (pH 8, $1.05 \text{ mol}/\text{dm}^3$ NaCl)

Aging period	0 month				2 months			
	Dose (kGy)	0	10	50	100	0	10	50
Cs system								
$\log [\text{Cs}]_{<10\text{kDa}}$	-8.28	-8.26	-8.25	-8.24	-8.30	-8.28	-8.28	-8.24
$\log [\text{B12}]$	-4.30	-4.32	-4.53	-5.87	-4.88	-4.95	-5.18	-6.34
$\log [\text{HSal}]$	-4.25	-4.13	-3.87	-3.82	-4.83	-4.78	-4.54	-4.29
$\log [\text{Cs}^+]$	-8.29	-8.27	-8.26	-8.25	-8.31	-8.29	-8.29	-8.26
$\log [\text{CsCl}_{(\text{aq})}]$	-9.87	-9.86	-9.84	-9.83	-9.89	-9.87	-9.87	-9.84
Eu system								
$\log [\text{Eu}]_{<10\text{kDa}}$	-9.38	-9.30	-9.13	-9.06	-9.62	-9.44	-9.21	-9.14
$\log [\text{B12}]$	-4.88	-4.95	-5.18	-6.34	-4.85	-4.94	-5.13	-6.32
$\log [\text{HSal}]$	-4.83	-4.78	-4.54	-4.29	-4.80	-4.77	-4.49	-4.26
$\log [\text{Eu}^{3+}]$	-9.63	-9.56	-9.38	-9.29	-9.89	-9.70	-9.46	-9.37
$\log [\text{Eu}(\text{OH})^{2+}]$	-9.82	-9.74	-9.56	-9.48	-10.07	-9.89	-9.65	-9.56
$\log [\text{Eu}(\text{B12})^+]$	-10.6	-10.6	-10.6	-7.91	-10.8	-10.7	-10.6	-7.91
$\log [\text{Eu}(\text{HSal})^{2+}]$	-12.3	-12.2	-11.8	-11.5	-12.6	-12.3	-11.8	-11.5
$[\text{EuL}]/[\text{Eu}]_{\text{free}}$	5.9 %	5.1 %	3.2 %	0.61 %	6.3 %	5.2 %	3.6 %	0.64 %

The distribution of the Eu species such as Eu^{3+} , $\text{Eu}(\text{OH})^{2+}$, and $\text{Eu}(\text{B12})^+$, $\text{Eu}(\text{HSal})^{2+}$, and others (e.g. EuCl^{2+}) was hypothetically estimated by the visual MINTEQ. As discussed below, the estimation implies that the presence of EuL ($\text{Eu}(\text{B12})^+$ and $\text{Eu}(\text{HSal})^{2+}$) cannot be neglected. For Cs, in contrast, the $[\text{Cs}]_{\text{ML}}$ is negligible ($<0.01\%$), so the complexation affinity of L would be quite low, similar to monovalent Na^+ . Here, the ratio (α_l) of HA- and L-complexed and non-complexed species in the liquid phase for Cs and Eu can be defined as follows (**Eqs. 4-9a and b**). This could be an indicator of the contribution of HA to the metal species in the liquid phase.

$$\alpha_{l_Cs} = \frac{[\text{Cs}]_{\text{CsHA}}}{[\text{Cs}]_{\text{free}}}, \quad (4-9a)$$

$$\alpha_{l_Eu} = \frac{[\text{Eu}]_{\text{EuHA}} + [\text{Eu}]_{\text{EuL}}}{[\text{Eu}]_{\text{free}}}, \quad (4-9b)$$

where the molecular size of Eu–HA and EuL would belong to the fractions of >10 kDa and <10 kDa, respectively, based on the different sizes of organic molecules. Therefore, the experimental Eu concentration in the liquid phase (filtered by a 10 kDa filter) was composed of $[\text{Eu}]_{\text{free}} + [\text{Eu}]_{\text{EuL}}$. The ratio of $[\text{Eu}]_{\text{free}}$ and $[\text{Eu}]_{\text{EuL}}$ was estimated using the MINTEQ calculation.

Similarly, the ratio of HA- and L-complexed and non-complexed species in the solid phase is defined as α_s for Cs and Eu (**Eqs. 4-10a and b**), which would be an index to realize the apparent contribution of metal–HA complexation to sorption onto a rock sample under a gamma irradiation field. Although the sorption of CsL, $[\text{Cs}]_{\text{SO-CsL}}$, is negligible, that of EuL needs to be considered.

$$\alpha_{s_Cs} = \frac{[\text{Cs}]_{\text{SO-CsHA}}}{[\text{Cs}]_{\text{SO-Cs}}}, \quad (4-10a)$$

$$\alpha_{s_Eu} = \frac{[\text{Eu}]_{\text{SO-EuHA}} + [\text{Eu}]_{\text{SO-EuL}}}{[\text{Eu}]_{\text{SO-Eu}}}, \quad (4-10b)$$

The direct determination of α_s was difficult in the batch experiment because of the difficulty in assigning the metal species that were complexed with HA and L on the solid surface. Nevertheless, α_s can be expressed by K_d and α_l , which are known values in the present study (Eq. 4-10c):

$$\alpha_{s_M} = \frac{K_{d,2_M}}{K_{d,1_M}} (1 + \alpha_{l_M}) - 1, \quad (4-10c)$$

Lastly, the sorption coefficients (m^3/kg) of HA, including L, in the absence and presence of metal ions, are defined as Eqs. 4-10a and b:

$$K_{d,1_HA} = \frac{(C_{org})_{SO-HA} + (C_{org})_{SO-L}}{(C_{org})_{HA} + (C_{org})_L} \frac{V}{m}, \quad (4-11a)$$

$$K_{d,2_HA} = \frac{(C_{org})_{SO-HA} + (C_{org})_{SO-L} + (C_{org})_{SO-MHA} + (C_{org})_{SO-ML}}{(C_{org})_{HA} + (C_{org})_L + (C_{org})_{ML} + (C_{org})_{MHA}} \frac{V}{m}, \quad (4-11b)$$

where the subscripts ML, MHA, SO–HA, SO–MHA, and SO–ML represent the fragmental ligand L-complexed with M (defined as <10 kDa), a macromolecule HA complexed with M (>10 kDa), an HA, metal–L complex, and a metal–HA complex sorbed on the rock sample (>0.20 μm), respectively.

4.4 Results and discussion

4.4.1 Characterization of Horonobe sedimentary rock sample

XRD analyzes indicated that the dominant mineralogical components of the Koetoi Formation mudstone were opal-A (40–50 wt%), smectite (<11 wt%), illite (9–17 wt%), quartz (7–10 wt%), and plagioclase (3–7 wt%) [22–24]. The same results were obtained in the present study (Fig. 4-1a). The similar rock sample collected from the Koetoi Formation was also composed of 16 wt% smectite and 10 wt% illite, and the cation exchange capacity (CEC) was about 20 meq/100 g [1]. The semi-quantitative method, elemental analysis by

EDX, indicated that the major compositions were O (80.9 wt%) and Si (14.8 wt%), followed by Al (2.7 wt%), Mg (0.6 wt%), Fe (0.4 wt%), and Na (0.3 wt%). The SEM imaging supported that the particle size of the mineral samples was mainly between 0.3 and 0.5 mm, and the mineral samples had a rough surface in the microstructures (**Fig. 4-2b**). The external specific surface area of the mineral samples was measured to be 20.96 m²/g via the N₂ adsorption isotherm. The surface charge of the minerals is evaluated from the difference of positive and negative charges [25]. The PZC, defined as the pH value at which the surface charge of Horonobe mineral is equal to zero, was determined to be 4.11 by potentiometric titration. The PZC of opal-A, quartz, smectite, illite, and plagioclase has been reported as 1.5–2.5 [26], 2.0 [27], 8.2 [28], 2.5 [29], and 1.4–2.4 [30], respectively. Therefore, the sample surface charge at sorption experimental condition (pH 8, which was much larger than the PZC value of 4.11, and $I = 0.05 \text{ mol/dm}^3$) would be negative (**Fig. 4-2c**).

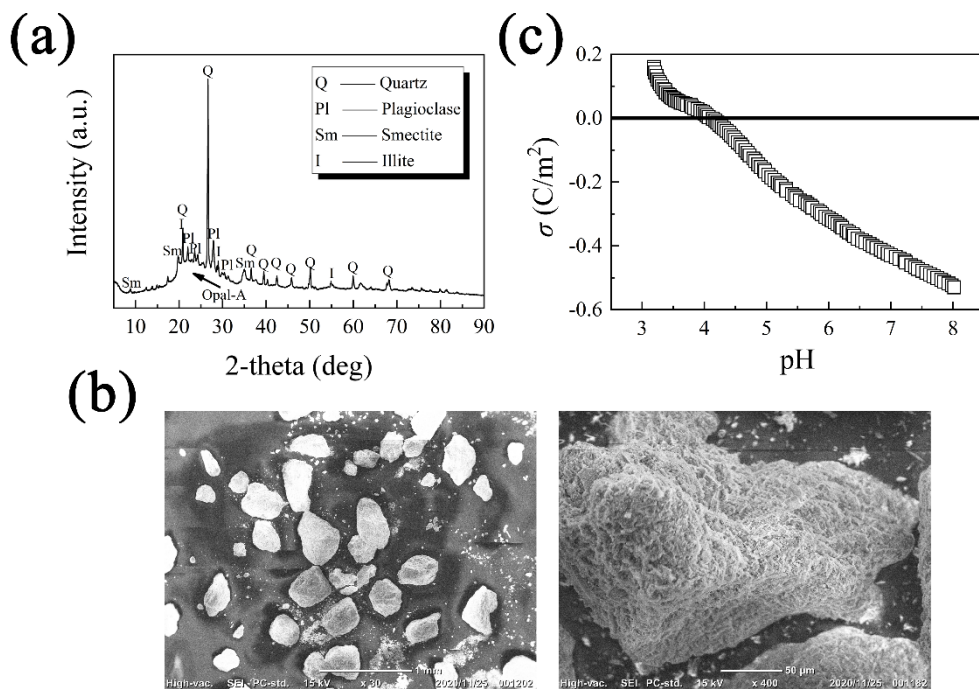


Fig. 4-2 Characterization of the rock sample of the Koetoi Formation. **a**: XRD spectra; **b**: Micrographs obtained at $\times 30$ and $\times 400$, respectively; **c**: The charge density of solid surface with pH

4.4.2 Chemical properties of gamma-irradiated HA solution

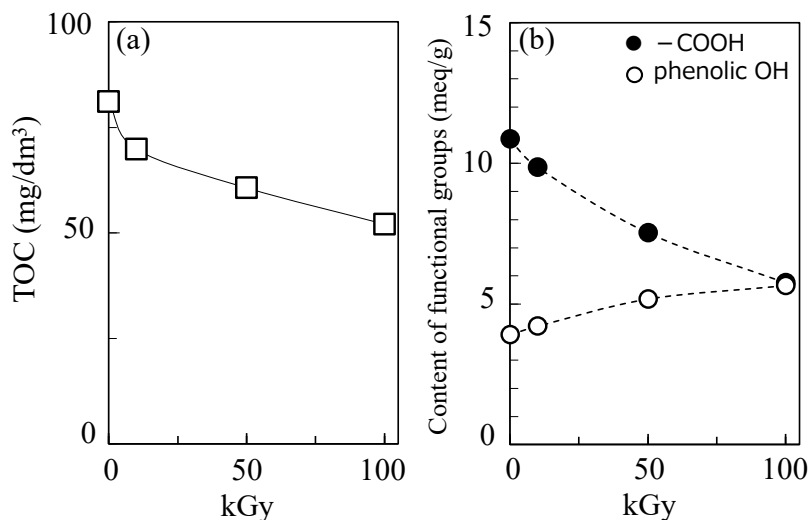


Fig. 4-3 Characterization of gamma-irradiated HA solution. (a) total organic carbon content (TOC), (b) functional group content. Error bars represent the standard errors of the mean of triplicate experiments. Curves represent the eye guide.

The pH of the HA solution decreased from 8.14 to 7.48, 6.78, and 6.12 after irradiation with 10, 50, and 100 kGy of gamma rays, respectively. This decreasing pH tendency with increasing dose has been found in a previous study which attributed it to the degradation of functional groups followed by carbonate formation in water [18]. **Fig. 4-3a** indicates that the TOC content in the original HA solutions decreased with the gamma irradiation dose because of the radiolysis decomposition of HA molecules, but no precipitation was observed at doses up to 100 kGy in the HA solution. The dissolved natural TOC content from the Horonobe sedimentary rock sample was 0.62 mg/dm³. Since it was less than 1 % of the TOC content of the added HA, the contribution of the natural organic content to metal complexation was not considered. In addition, the sorption ability of HA and L was considered to be predominantly responsible for the functional groups in HA molecules [31], thus the acidic functional group contents in HA solution were determined by

acid–base titration, and the modified Henderson–Hasselbalch model was adopted to fit the titration data points [32, 33]. Results indicated that the decomposition of –COOH group and the formation of phenolic –OH group (as shown in **Fig. 1b**).

4.4.3 Effect of gamma irradiation on the sorption of HA molecules

In the absence of metal ions, the sorption coefficient, K_{d_HA} , in **Eq. 4-11a** decreased slightly as the dose increased (**Fig. 4-4a**). In general, sorption mechanisms of HA have been governed by ligand exchange, cation bridge, hydrogen binding, electrostatic interactions (attraction or repulsion) and others [34, 35]. As shown in **Table 4-1**, the ratio of the TOC in the <10 kDa fraction increased with dose, becoming a smaller-molecular-weight HA molecule to L. Non-irradiated HA of higher molecular weight would have a higher sorption ability to the rock surface than the lower molecular weight HA degraded by the gamma irradiation. Kaiser observed that the mineral–organic association decreased with decreasing carboxyl C content in organic ligands by ^{13}C NMR study [29]. Meanwhile, **Fig. 4-4b** indicates that the acid dissociation ratio of the functional groups –COO[–]/–COOH and phenolic –O[–]/–OH, which were calculated based on the pK_1 (4.22, 4.03, 3.61, 3.58 for 0, 10, 50 and 100 kGy) and pK_2 (10.21, 9.90, 9.86, 9.55 for 0, 10, 50, 100 kGy) values, increased with dose. It would enhance an electrostatic repulsion between the negatively charged HA and the mineral surface, resulting in the decrease of K_{d_HA} . Thus, multiple factors have been considered for the decrease of K_{d_HA} with dose. The identification of the predominant sorption mechanism is difficult at this moment.

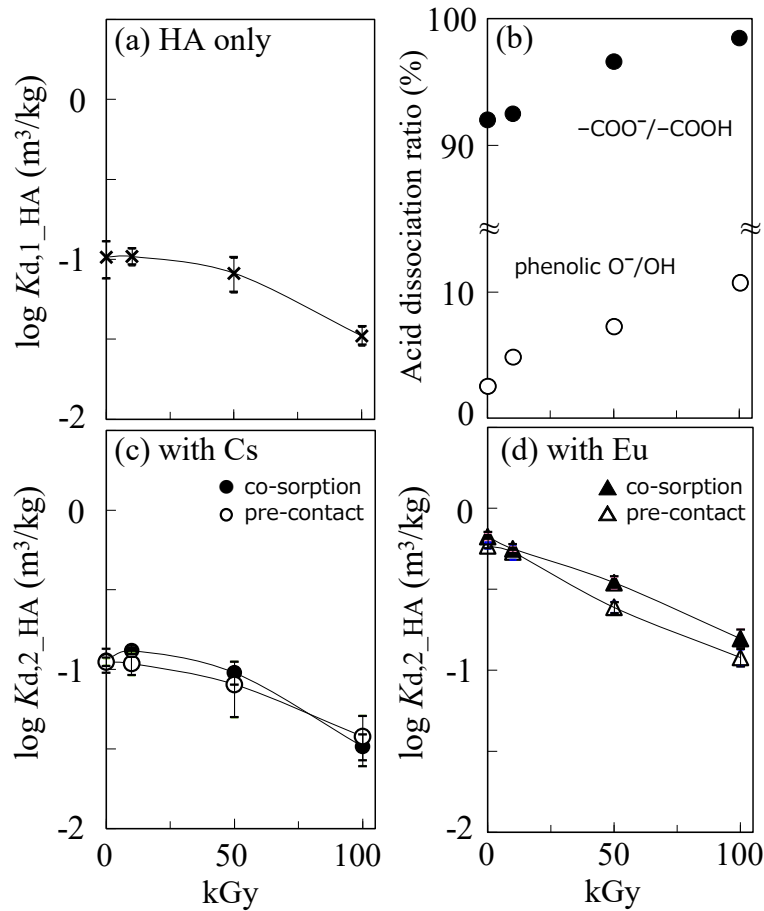


Fig. 4-4 Dependence of the sorption coefficient of HA on the sedimentary rock samples on gamma irradiation dose. **(a)** HA only system; **(b)** Acid dissociation ratio in HA only system; **(c)** and **(d)** Cs–HA and Eu–HA systems. The 0.20 μm pore size filter was used. Curves represent the eye guide. $(C_{\text{org}})_i = 81.12, 69.85, 60.67, 52.05 \text{ mg/dm}^3$ for 0, 10, 50, 100 kGy, respectively; $[\text{Cs}^+]_i = 0.97 \times 10^{-8} \text{ mol/dm}^3$, $[\text{Eu}^{3+}]_i = 1.06 \times 10^{-8} \text{ mol/dm}^3$; $L/S = 0.5 \text{ m}^3/\text{kg}$, $I = 0.05 \text{ mol/dm}^3$ (NaCl), $\text{pH} = 8 \pm 0.3$

In addition, **Fig. 4-4c** shows that $K_{d\text{-HA}}$ in the Cs^+ –HA–mineral system was similar to that in the HA–mineral system, suggesting the weak complexation of Cs^+ ions with HA. On the other hand, under similar low metal ion concentration condition, the $K_{d\text{-HA}}$ in the Eu^{3+} –HA–mineral system (**Fig. 4-4d**) was higher than that in the HA–mineral and Cs^+ –HA–mineral systems. Liu and Gonzalez also found that the sorption coefficient of HA was

enhanced by introducing multivalent metal ions, such as Cd^{2+} , Cu^{2+} , and Pd^{2+} ions [37]. Multivalent metal cations could not only reduce or neutralize the apparent negative charge on HA by metal–HA complexation, but also act as “cation-bridging” of the rock surface–metal ion–HA [37]. Moreover, it is observed that the decreasing trend of the $K_{d\text{-HA}}$ in the Cs^+ –HA and Eu^{3+} –HA systems with the gamma irradiation dose was consistent with that in the HA only system. Thus, this similar trend might be interpreted by the decomposition of –COOH group and the increase of the acid dissociation ratio of the functional groups – COO^- /–COOH, which enhanced the electrostatic repulsion between the negatively charged HA and the mineral surface [38].

4.4.4 Effect of gamma irradiation on the sorption of Cs^+ and Eu^{3+} ions

Dissolution of natural Cs^+ and Eu^{3+} from the Horonobe sedimentary rock sample (pH = 8, $I = 0.05 \text{ mol/dm}^3$ (NaCl)) was lower than $3 \times 10^{-10} \text{ mol/dm}^3$, thus the impact of the dissolution on the initial concentration of these ions was negligible.

Fig. 4-5 shows the sorption coefficients of Cs^+ and Eu^{3+} , $K_{d\text{-Cs}}$ and $K_{d\text{-Eu}}$, on the rock sample in the absence of HA. The logarithmic $K_{d,1\text{-Cs}}$ is -0.54, and the similar $\log K_{d\text{-Cs}}$ value on sedimentary rock system was reported to be -0.30 at pH 8 [39]. The similar $\log K_{d,1\text{-Cs}}$ value on the deeper Horonobe rock sample from the Wakkanai Formation, which was composed of 7 % illite and 11 % smectite [40], also suggested the Cs–selective sorption site of these clay mineral components with high CEC [1]. Such a mechanism of Cs sorption reaction has been well investigated, e.g. the highly selective frayed edge site (FES) in illites [41] and the interlayer sites in smectite [42]. Thus, the Cs sorption in this study would be predominant in the sedimentary rock sample.

For Eu, the $\log K_{d,1\text{-Eu}}$ value is 0.49, and the similar value on sedimentary rock system was reported to be 0.32 at pH 7.86 [43]. The values of $K_{d,1\text{-Eu}}$ are significantly higher than

those of $K_{d,1_Cs}$ [44]. The stronger sorption of europium has been attributed to differences in the ability of the chemical exchange, electrostatic interaction and surface complexation [45]. The sorption of Eu^{3+} on Na-montmorillonite by time-resolved laser fluorescence spectroscopy, suggesting that the surface complexation of Eu^{3+} and its positively charged hydroxides such as $Eu(OH)^{2+}$, is mainly predominant at pH 8 range rather than the cation exchange reaction [46]. In addition, it has also been observed that Eu could sorb on oxide minerals in a sedimentary rock, such as opal-A, quartz, and plagioclase because of the deprotonation induced by the surface hydroxyl groups on oxides [47].

The $\log K_{d,2}$ value of Cs^+ with non-irradiated HA was almost identical to that without HA, similarly, the K_{d_HA} values in the absence and presence of Cs^+ , as shown in **Figs. 4-4a** and **c**, were similar. This result also supports the premise that Cs^+ sorption on the rock surface (probably, on a cation exchange site) did not facilitate HA sorption, and vice versa. The $\log K_{d,2}$ values of Cs^+ were independent of the dose (0–100 kGy). There are two possible explanations; one is that the complexation affinity of HA with Cs^+ is significantly low, which has been found in a previous study [18], and the other is that enough sorption sites for a trace amount of Cs^+ would exist in a rock sample although some of sites would be occupied by the sorption of HA [48]. Here, it is noted that the impact of HA on the Cs sorption depends on the concentration ratio of them. Even in the case of early failure of radioactive waste package in the deep geological repository, the leaching concentration of radioactive Cs will be kept low, as intended by the experimental conditions of this study. Under a tracer metal concentration condition, the decrease in the number of sorption sites due to the sorption of HA molecules to the rock might not affect the K_d value of Cs.

In contrast, the sorption coefficient of Eu^{3+} was suppressed by the addition of non-irradiated HA solution (**Fig. 4-5b**), where the $\log K_{d,1_Eu}$ value in the absence of HA was as high as +0.5. This less sorption of Eu has been explained by the formation of soluble metal

organic complexes in aqueous solution [49], suggesting that the complexation between metal ions with functional groups of HA would be predominant compared to the metal sorption on the solid surface. Nevertheless, the $K_{d,2_Eu}$ values recovered slightly with the applied doses of gamma rays. It is interesting to note that the value of $K_{d,2_HA}$ (**Fig. 4-4d**) is one order of magnitude higher than that in the only-HA and Cs systems, even though the sorption of Eu is suppressed by the coexistence of HA. The gamma irradiation of HA resulted in a decrease in the content of total functional groups, especially $-COOH$, resulting in the decrease of Eu–HA complexing ability, and the increase of the free Eu^{3+} concentration. This consideration seems to be reasonable, but the sorption reactions in the ternary metal–HA–rock system are likely to be affected by their quantitative balance.

It should be noted that the $\log K_{d,2_Eu}$ value at 0 kGy in the pre-contact system (-1.0) was 0.5 order lower than that in the co-sorption system (-0.5) (**Fig. 4-5b**). During the aging period of 2 months in the pre-contact system, Eu^{3+} complexation with the humic heterogeneous macromolecule occurred. Wang et al. investigated the dissociation of Am^{3+} with HA by the chelating exchange resin and found that the dissociation rate would decrease with increasing aging time, suggesting that bonding becomes stronger [50]. In fact, with an insight into the interaction of actinides and HA, two types of binding sites on HA, assuming spherical particles, were suggested: reversible ion exchange sites on HA molecular surfaces, and less exchangeable, kinetically hindered sites inside the molecules [51]. Some studies have also suggested that multivalent metal ions (e.g., Am^{3+} , Eu^{3+} , Th^{4+}) on the HA surfaces would be gradually surrounded within the HA folding, penetrating from the surface to the interior with increasing aging time [52, 53], and then become thermodynamically stable inner-sphere complexes with macromolecular structures [54]. Such “kinetically controlled” reactions of metal–HA interaction are related to the molecular size of HA, that is, a smaller-molecular-weight HA might provide less kinetic impact for complexation within the HA

folds. Further experimental evidence is needed for the interpretation of the dependence of the kinetic reaction of HA with metal ions on the gamma irradiation dose.

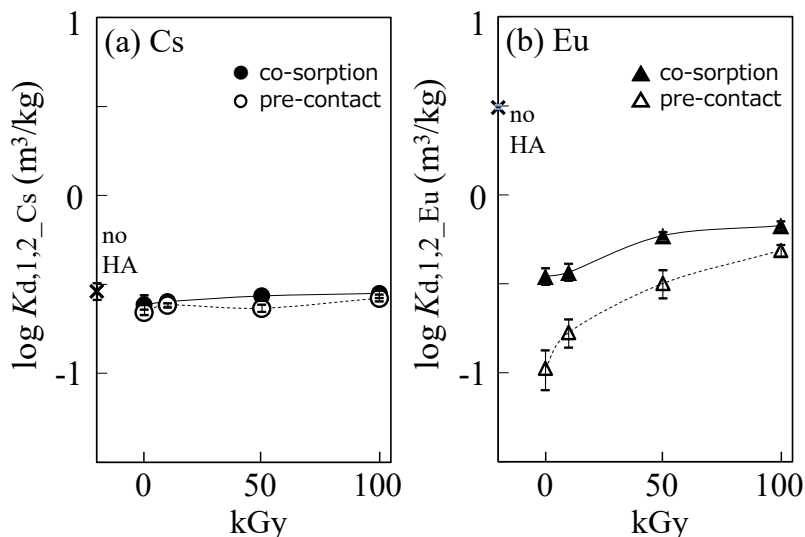


Fig. 4-5 Dependence of sorption coefficient of Cs⁺ (a) and Eu³⁺ (b) on the sedimentary rock samples on gamma irradiation dose. The 0.20 μm pore size filter was used. Curves represent the eye guide. $(C_{org})_i = 81.12, 69.85, 60.67,$ and 52.05 mg/dm^3 for 0, 10, 50, and 100 kGy, respectively; $[Cs^+]_i = 0.97 \times 10^{-8}$ mol/dm^3 , $[Eu^{3+}]_i = 1.06 \times 10^{-8}$ mol/dm^3 ; $L/S = 0.5$ m^3/kg , $I = 0.05$ mol/dm^3 (NaCl), $pH = 8 \pm 0.3$

Fig. 4-6 shows the dependence of α_l and α_s on the gamma irradiation dose. The α_l value of Cs⁺ in **Eq. 4-9a** was low, approximately, 0.1–0.2, throughout the entire irradiation dose range (**Fig. 4-6a**), suggesting the weak complexation of Cs⁺ with HA in the liquid phase, similar to that found in a previous study [18]. The α_s values were also close to 0 (0.01–0.05). Both these low values supported the negligible contribution of HA to Cs⁺ sorption in the present study. In contrast, α_s and α_l for Eu³⁺ were higher than those for Cs⁺ (**Fig. 4-6b**), indicating that the complexing ability of HA to Eu³⁺ was higher than that of HA to Cs⁺. The α_s and α_l values in the pre-contact system were almost twice as high as those in the co-sorption system, suggesting that the Eu–HA complexation was facilitated in the aging period.

In these cases, the ratio of the sum of Eu–HA and EuL and the free Eu concentration in **Eq. 4-9b** decreased with increasing dose, suggesting that gamma irradiation reduced the formation of stable Eu–HA(L) complexes. However, since the impact of the EuL complex on the α_1 value could not be determined experimentally, the relative proportions of $[\text{Eu}]_{\text{EuL}}$ and $[\text{Eu}]_{\text{free}}$ in the <10 kDa fraction was roughly estimated using MINTEQ. Owing to the negligible complexation affinity of L, the high α_1 values of 36 (pre-contact) and 14 (co-sorption) decreased with increasing irradiation dose. However, the α_s values for Eu^{3+} (**Eq. 9b**) were less than 1, indicating that the stable Eu–HA complex in the liquid phase suppressed Eu^{3+} sorption, whereas the smaller molecular ligand L had little involvement in sorption and complexation.

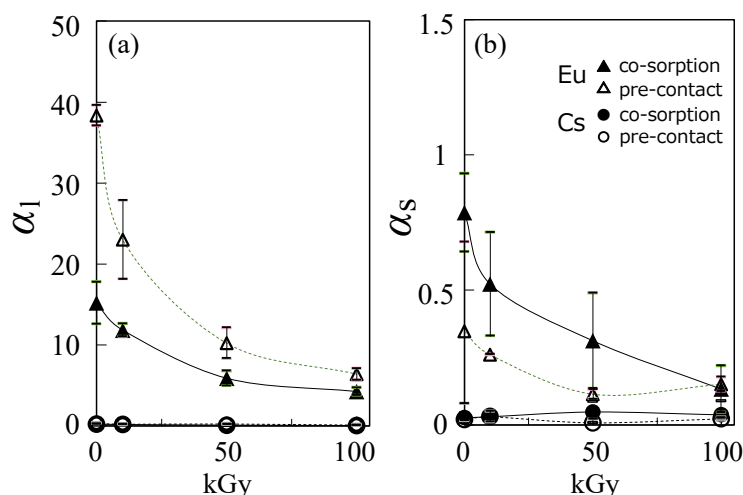


Fig. 4-6 Dependence of α_1 and α_s for Cs^+ –HA and Eu^{3+} –HA systems on irradiation dose. Curves represent the eye guide

Table 4-3 summarized the distribution of concentration of metal species. The distribution of Cs species is almost independent of the gamma irradiation dose; In the Eu system, the direct sorption of non-complexed Eu ions on a rock sample is predominant ($A_{\text{SO-M}} > A_{\text{SO-MHA}}$). In addition, it is noted that the percentage of Eu–HA complexes sorbed on solid ($A_{\text{SO-MHA}}$) was nearly constant and independent of dose, while the percentage of Eu–

HA complexes (A_{MHA}) in liquid decreased with dose. These phenomena support the radiolysis products such as a smaller-molecular-weight catechol derivative due to the decomposition of HA [18], which would contribute to the formation of surface complexation.

Table 4-3 Distribution of estimated concentration of metal species in ternary systems (metal ion–HA–rock) by modeling. The subscript “free”, “SO–M”, “MHA” and “SO–MHA” represented the free metal ions, the metal ions sorbed, the metal ions complexed with HA and the metal–HA sorbed, respectively

Systems	Dose (kGy)	A_{free} (%)	A_{SO-M} (%)	A_{MHA} (%)	A_{SO-MHA} (%)
	0	54.5	31.5	13.1	0.9
Cs/HA/rock	10	56.1	32.5	10.4	1.0
Co-sorption	50	58.0	33.6	6.8	1.6
	100	60.0	34.7	4.0	1.3
	0	57.7	29.9	11.8	0.6
Cs/HA/rock	10	54.7	31.6	12.7	1.0
Pre-contact	50	62.1	31.4	6.2	0.3
	100	58.3	33.8	7.1	0.8
	0	3.7	26.7	55.7	13.9
Eu/HA/rock	10	4.5	27.8	53.2	14.5
Co-sorption	50	6.7	38.2	39.3	15.8
	100	8.1	42.5	34.7	14.7
	0	2.1	13.0	80.4	4.5
Eu/HA/rock	10	3.1	19.5	73.3	5.1
Pre-contact	50	5.5	34.2	56.4	3.9
	100	6.9	42.7	44.0	6.4

4.5 Summary

Batch sorption experiments were performed to evaluate the effect of gamma-irradiated HA on the sorption reactions of Cs^+ and Eu^{3+} at neutral pH. The purified Aldrich HA in solution was irradiated by a ^{60}Co source of gamma rays to 0, 10, 50, and 100 kGy. Gamma irradiation reduced the sorption coefficients of the HA molecules. In the absence of HA, the sorption coefficient of trivalent Eu ions was as high as the reported values. By adding non-irradiated HA, the sorption of Eu ions complexed with HA was largely suppressed owing to the formation of neutral or negatively charged complexes in the liquid phase. Although the ratio of HA- and L-complexed and non-complexed species in the liquid phase was more than 10, the ratio in the solid phase was less than 1. These ratios were evaluated based on the difference in metal and TOC concentration solutions filtered by 0.20 μm and 10 kDa pore size filters, to estimate the contribution of HA in liquid and solid to metal sorption. The results indicated the ratios decreased with increasing irradiation dose, suggesting that the metal complexation affinity of the decomposed fragments of HA (ligands) was lower than that of the original HA. Meanwhile, the sorption of Cs^+ was unaffected by the presence of HA and the gamma irradiation dose, mainly due to the weak complexation ability of monovalent cation with HA, indicating the insignificant contribution of HA to Cs^+ sorption, mainly by cation exchange reaction, in the present study. This novel and easy filtering method to evaluate the molecular-weight distribution of species in liquid and solid could provide more quantitative findings of the impact of HA on the sorption of metal ions onto sedimentary rock sample. Further experimental investigation of the sorption mechanism will provide more detailed insight into the different impacts of humic substances on Cs and Eu ions.

Sorption database has been widely established for decades in various countries to evaluate the sorption of metal ions in the groundwater, which is important for the safety

assessment of nuclear waste disposal. However, the conclusion in this study would provide new insight that effect of long-term gamma irradiation field probably needs to be considered into the evaluation of the retardation and the acceleration effects of radionuclides migration in the near field of a disposal site.

Reference

- [1] Y. Tachi, K. Yotsuji, Y. Seida, M. Yui, Diffusion and sorption of Cs^+ , I^- and HTO in samples of the argillaceous Wakkanai Formation from the Horonobe URL, Japan: Clay-based modeling approach. *Geochim. Cosmochim. Acta* **75** (2011), 6742–6759.
- [2] M. Pédrot, A. Dia, M. Davranche, Double pH control on humic substance-borne trace elements distribution in soil waters as inferred from ultrafiltration. *J. Colloid Interface Sci.* **339** (2009), 390–403.
- [3] M. Ge, D. Wang, J. Yang, Q. Chen, Z. Wu, Z. Guo, Co-transport of U(VI) and akaganéite colloids in water-saturated porous media: Role of U(VI) concentration, pH and ionic strength. *Water Res.* **147** (2018), 350–361.
- [4] H. Fakour, T. Lin, Experimental determination and modeling of arsenic complexation with humic and fuvic acids, *J. Hazard. Mater.* **279** (2014), 569–578.
- [5] Y. Seida, M. Terashima, Y. Tachi, K. Iijima, T. Nakazawa, M. Yamada, M. Yui, Sorption and diffusion of Eu in sedimentary rock in the presence of humic substance. *Radiochim. Acta* **98** (2010), 703–709.
- [6] S.A. Adeleye, P.G. Caly, M.O.A. Oladipo, Sorption of caesium, strontium and europium ions on clay minerals. *J. Mater. Sci.* **29** (1994), 954–958.
- [7] K. Ota, H. Abe, T. Kunimaru, Horonobe underground research laboratory project; synthesis of phase I investigations 2001–2005, volume “Geoscientific research”, JAEA-Research-2010-068, Japan Atomic Energy Agency (2010).
- [8] T. Sasaki, T. Koukami, T. Kobayashi, A. Kirishima, H. Murakami, Y. Amano, T. Mizuno, T. Iwatsuki, H. Sasamoto, K. Miyakawa, Determination of dissolved natural thorium and uranium in Horonobe and Mizunami underground research laboratory groundwater and its thermodynamic analysis, *J. Nucl. Sci. Technol.* **54** (2017), 373–381.

- [9] H. Kunimaru, T., Ota, K., Alexander, W. Russell, H. Yamamoto, Groundwater/porewater hydrochemistry at Horonobe URL: Data freeze 1. Preliminary data quality evaluation for boreholes HDB-9, 10 and 11, JAEA-Research-2010-035, Japan Atomic Energy Agency (2010).
- [10] K. Hama, T. Kunimaru, R. Metcalfe, A.J. Martin, The hydrogeochemistry of argillaceous rock formations at the Horonobe URL site, Japan, *Phys. Chem. Earth* **32** (2007), 170–180.
- [11] H. Sasamoto, H. Satoh, R.C. Arthur, Characterization of mineralogical controls on ammonium concentrations in deep groundwaters of the Horonobe area, Hokkaido, *J. Geochemical Explor.* **188** (2018), 318–325.
- [12] E. Ishii, Y. Hashimoto, D. Inagaki, Washout of clay-rich gouge in a pre-grouted fault zone and increase in groundwater inflow during tunnel excavation in Neogene siliceous mudstone (Horonobe, Japan), in: Proceedings of 10th Asian Regional Conference of International Association for Engineering Geology and the Environment (IAEG ARS 2015), Japan Society of Engineering Geology, 2015.
- [13] M. Naderi, Surface Area: Brunauer-Emmett-Teller (BET), *Prog. Filtr. Sep.* (2015), 585–608.
- [14] A.K. Covington, M.I.A. Ferra, R.A. Robinson, Ionic product and enthalpy of ionization of water from electromotive force measurements, *Faraday Trans. I* **73** (1977), 1721–1730.
- [15] T. Mahmood, M.T. Saddique, A. Naeem, P. Westerhoff, S. Mustafa, A. Alum, Comparison of different methods for the point of zero charge determination of NiO, *Ind. Eng. Chem. Res.* **50** (2011), 10017–10023.
- [16] M. Jiménez-Reyes, M. Solache-Ríos, A. Rojas-Hernández, Application of the specific ion interaction theory to the solubility product and first hydrolysis constant of

- europium, *J. Solution Chem.* **35** (2006), 201–214.
- [17] Q. Zhao, R. Goto, T. Saito, T. Kobayashi, T. Sasaki, Effect of gamma-irradiation on complexation of humic substances with divalent calcium ion, *Chemosphere* **256** (2020), 127021.
- [18] Q. Zhao, T. Kobayashi, T. Saito, T. Sasaki, Gamma-irradiation-induced molecular-weight distribution and complexation affinity of humic acid with Cs^+ , Sr^{2+} , and Eu^{3+} , *J. Hazard. Mater.* **411** (2021), 125071.
- [19] T. Sasaki, H. Yoshida, S. Aoyama, T. Kobayashi, I. Takagi, H. Moriyama, Discrete fragment model for apparent formation constants of actinide ions with humic substances, *Radiochim. Acta* **103** (2015), 411–421.
- [20] I. Christl, R. Kretzschmar, C-1s NEXAFS spectroscopy reveals chemical fractionation of humic acid by cation-induced coagulation, *Environ. Sci. Technol.* **41** (2007), 1915–1920.
- [21] R.M. Smith, R.J. Motekaitis, A.E. Martell, NIST standard reference database 46, NIST critically selected stability constants of metal complexes database Ver 2, (2004).
- [22] M. Mazurek, U. Eggenberger, Mineralogical analysis of core samples from the Horonobe area, in: Switz. RWI Tech. Rep. 05-01, Institute of Geological Sciences, University of Bern: Bern, Switzerland, 2005.
- [23] N. Hiraga, E. Ishii, Mineral and chemical composition of rock core and surface gas composition in Horonobe underground research laboratory Project (Phase I), JAEA-Data/Code 2007-022, Japan Atomic Energy Agency (2008), p100.
- [24] H. Harrison, D. Wagner, H. Yoshikawa, J.M. West, A.E. Milodowski, Y. Sasaki, G. Turner, A. Lacinska, S. Holyoake, J. Harrington, D. Noy, P. Coombs, K. Bateman, K. Aoki, Microbiological influences on fracture surfaces of intact mudstone and the implications for geological disposal of radioactive waste, *Mineral. Mag.* **75** (2011),

- 2449–2466.
- [25] T. Mahmood, M.T. Saddique, A. Naeem, P. Westerhoff, S. Mustafa, A. Alum, Comparison of different methods for the point of zero charge determination of NiO. *Ind. Eng. Chem. Res.* **50** (2011), 10017–10023.
- [26] L.A. Williams, D.A. Crerar, Silica diagenesis: II. General mechanisms, *J. Sediment. Petrol.* **55** (1985), 312–321.
- [27] W. Wang, J. Cong, J. Deng, X. Weng, Y. Lin, Y. Huang, T. Peng, Developing effective separation of feldspar and quartz while recycling tailwater by HF pretreatment, *Minerals* **8** (2018), 1–15.
- [28] S. Arfaoui, N. Hamdi, N. Frini-Srasra, E. Srasra, Determination of point of zero charge of PILCS with single and mixed oxide pillars prepared from Tunisian-smectite, *Geochemistry Int.* **50** (2012), 447–454.
- [29] S.A. Hussain, Ş. Demirci, G. Özbayoğlu, Zeta potential measurements on three clays from Turkey and effects of clays on coal flotation, *J. Colloid Interface Sci.* **184** (1996), 535–541.
- [30] A.C. Lasaga, Chemical kinetics of water-rock interactions, *Journal Geophys. Res.* **89** (1984), 4009–4025.
- [31] C.R. Evanko, D.A. Dzombak, Influence of structural features on sorption of NOM-analogue organic acids to goethite, *Environ. Sci. Technol.* **32** (1998), 2846–2855.
- [32] S.J. Driver, E.M. Perdue, Acidic Functional groups of Suwannee river natural organic matter, humic acids, and fulvic acids, in: *Advances in the physicochemical characterization of dissolved organic matter: impact on natural and engineered systems*. American chemical society, 2014, p4–75.
- [33] J.D. Ritchie, E. M. Perdue, Proton-binding study of standard and reference fulvic acids, humic acids, and natural organic matter, *Geochim. Cosmochim. Acta* **67** (2003),

85–96.

- [34] A.J. Fairhurst, P. Warwick, The influence of humic acid on europium-mineral interactions, *Colloids Surfaces A Physicochem. Eng. Asp.* **145** (1998), 229–234.
- [35] R.L. Parfitt, A.R. Fraser, V.C. Farmer, Adsorption on hydrous oxides. III. Fulvic acid and humic acid on goethite, gibbsite and imogolite, *J. Soil Sci.* **28** (1977), 289–296.
- [36] K. Kaiser, Sorption of natural organic matter fractions to goethite (α -FeOOH): Effect of chemical composition as revealed by liquid-state ^{13}C NMR and wet-chemical analysis, *Org. Geochem.* **34** (2003), 1569–1579.
- [37] A. Liu, R.D. Gonzalez, Adsorption/desorption in a system consisting of humic acid, heavy metals, and clay minerals, *J. Colloid Interface Sci.* **218** (1999), 225–232.
- [38] I. Christl, R. Kretzschmar, Interaction of copper and fulvic acid at the hematite-water interface, *Geochim. Cosmochim. Acta* **65** (2001), 3435–3442.
- [39] S.R. Aston, E.K. Duursma, Concentration effects on ^{137}Cs , ^{65}Zn , ^{60}Co and ^{106}Ru sorption by marine sediments, with geochemical implications, *Netherlands J. Sea Res.* **6** (1973), 225–240.
- [40] E. Ishii, A. Furusawa, Detection and correlation of tephra-derived smectite-rich shear zones by analyzing glass melt inclusions in mineral grains. *Eng. Geol.* **228** (2017), 158–166.
- [41] C. Poinssot, B. Baeyens, M.H. Bradburg, Experimental and modelling studies of caesium sorption on illite. *Geochim. Cosmochim. Acta* **63** (1999), 3217–3227.
- [42] R. Sutton, G. Sposito, Molecular simulation of interlayer structure and dynamics in 12.4 Å Cs-smectite hydrates. *J. Colloid Interface Sci.* **237** (2001), 174–184.
- [43] S. Holgersson, Oskarshamn site investigation Batch experiments of I , Cs , Sr , Ni , Eu , U and Np sorption onto soil from the Laxemar area, No. SKB-P-09-29, Swedish nuclear fuel and waste management Co., 2009.

- [44] B. Grambow, M. Fattahi, G. Montavon, C. Moisan, E. Giffaut, Sorption of Cs, Ni, Pb, Eu(III), Am(III), Cm, Ac(III), Tc(IV), Th, Zr, and U(IV) on MX 80 bentonite: An experimental approach to assess model uncertainty, *Radiochim. Acta* **94** (2006), 627–636.
- [45] B.K. Singh, R. Tomar, S. Kumar, A. Jain, B.S. Tomar, V.K. Manchanda, Sorption of ^{137}Cs , ^{133}Ba and ^{154}Eu by synthesized sodium aluminosilicate (Na-AS). *J. Hazard. Mater.* **178** (2010), 771–776.
- [46] T. Sasaki, K. Ueda, T. Saito, N. Aoyagi, T. Kobayashi, I. Tagaki, T. Kimura, Y. Tachi, Sorption of Eu^{3+} on Na-montmorillonite studied by time-resolved laser fluorescence spectroscopy and surface complexation modeling. *J. Nucl. Sci. Technol.* **53** (2016), 592–601.
- [47] I.M. Ugwu, O.A. Igbokwe, Sorption of heavy metals on clay minerals and oxides: a review. *Advanced Sorption Process Applications*, Serpil Edebali, IntechOpen, 2018.
- [48] K. Chang, C. Hsu, H. Tamaki. Basic study of ^{137}Cs Sorption on Soil. *J. Nucl. Sci. Technol.* **30** (1993), 1243–1247.
- [49] X.L. Tan, X.K. Wang, H. Geckeis, TH. Rabung, Sorption of Eu(III) on humic acid or fulvic acid bound to hydrous alumina studied by SEM-EDS, XPS, TRLFS, and batch techniques. *Environ. Sci. Technol.* **42** (2008), 6532–6537.
- [50] X. Wang, C. Chen, J. Du, X. Tan, D. Xu, S. Yu, Effect of pH and aging time on the kinetic dissociation of $^{243}\text{Am(III)}$ from humic acid-coated $\gamma\text{-Al}_2\text{O}_3$: A chelating resin exchange study, *Environ. Sci. Technol.* **39** (2005), 7084–7088.
- [51] W. Schuessler, R. Artinger, B. Kienzler, J. Il Kim, Conceptual modeling of the humic colloid-borne americium(III) migration by a kinetic approach, *Environ. Sci. Technol.* **34** (2000), 2608–2611.
- [52] A. Stockdale, N.D. Bryan, The influence of natural organic matter on radionuclide

- mobility under conditions relevant to cementitious disposal of radioactive wastes : A review of direct evidence, *Earth Sci. Rev.* **121** (2013), 1–17.
- [53] R. Artinger, W. Schuessler, T. Schaefer, J. Il Kim, A kinetic study of Am(III)/humic colloid interactions, *Environ. Sci. Technol.* **36** (2002), 4358–4363.
- [54] X. Wang, W. Dong, X. Dai, A. Wang, J. Du, Z. Tao, Sorption and desorption of Eu and Yb on alumina: Mechanisms and effect of fulvic acid, *Appl. Radiat. Isot.* **52** (2000), 165–173.

Chapter 5 Conclusions, significance of the study, and recommendations for future work

5.1 General conclusions

The sorption behavior of radionuclides is related to their complexation with HSs. The gamma irradiation field near nuclear waste repositories can induce decomposition and chemical changes in the HSs, which can affect the complexation of HSs with metal ions. Therefore, the effects of gamma irradiation on the complexation and sorption behavior of metal ions in the presence of HSs were investigated in this study. The research contents and conclusions of each chapter are summarized as follows:

Chapter 1 provides an overview of the deep geological disposal of nuclear waste, and introduces the complexation and sorption behavior of radionuclides in groundwater.

Chapter 2 describes the effects of gamma irradiation on the complexation of HSs with Ca^{2+} ions. HS solutions were gamma-irradiated to 0 (non-irradiation), 10, 100, and 500 kGy at dose rates of 1 kGy/h or 0.1 kGy/h. The chemical properties of the irradiated HS solutions were investigated using TOC measurements, UV–vis spectrometry, ^{13}C NMR, and acid–base titration. The characterization results indicated that the gamma irradiation decreased the TOC content and facilitated the degradation of the HS molecules. Under the influence of the applied gamma irradiation, $-\text{COOH}$ was decomposed and phenolic $-\text{OH}$ was formed in the HS solution. A possible mechanism of the effects of radiolysis on HSs involving decarboxylation and hydroxylation was proposed. The complexation ability of irradiated HS with Ca^{2+} ions was studied using a Ca-ISE. The apparent formation constants of the Ca–HS complexes increased as the irradiation dose increased, which was attributed to the relative increase in the ratio of the phenolic $-\text{OH}$ to the carboxylic groups of the HS. The contribution of the phenolic $-\text{OH}$ groups to the Ca–HS complexes was suppressed at a pH

of 5 owing to their high acid dissociation constants. In addition, the radiation dose rates of 1 kGy/h and 0.1 kGy/h did not significantly affect the properties of the HS and the apparent formation constants of the Ca–HS complexes.

Chapter 3 describes the effects of gamma irradiation on complexation affinity in terms of the molecular-weight fractions of HA (the main component of the HS) with Cs^+ , Sr^{2+} , and Eu^{3+} ions. HA solutions were subjected to gamma irradiation (0, 1, 5, 10, 50, and 100 kGy) using a ^{60}Co source. The non-irradiated and irradiated HA molecules were fractionated by ultrafiltration into four categories: >100, 50–100, 10–50, and <10 kDa. TOC measurements and potentiometric titration analysis suggested that certain gamma-irradiated HA molecules degraded into smaller molecules, and that the radiolysis-degradation-induced phenolic –OH became the predominant functional group in the low-molecular-weight fractions of HA. The effects of the absorbed dose of gamma rays on the distributions of Cs^+ , Sr^{2+} , and Eu^{3+} ions in the molecular weight fractions of the metal–HA systems were examined to analyze the complexation affinity. The metal ions were distributed in the low-molecular-weight fractions at different doses, which corresponded to the degradation of HA molecules. For a predetermined absorbed dose, the Cs^+ ions did not alter the molecular weight distribution of the TOC of the degraded HA molecules. Conversely, the Sr^{2+} and Eu^{3+} ions redistributed the organic carbon content toward the higher-molecular-weight fractions.

Chapter 4 describes the influence of HA and its radiological degradation on the sorption of Cs^+ and Eu^{3+} using sedimentary rock that was obtained from the Horonobe URL in Japan. A HA solution was irradiated with different doses of gamma irradiation (0, 10, 50, and 100 kGy) using a ^{60}Co gamma-ray source prior to establishing contact between the metal ions and the solid sorbent. The HA molecule decomposed into smaller molecules with low complexation affinities. Batch sorption experiments were performed to evaluate the effects of gamma-irradiated HA on the sorption of Cs^+ and Eu^{3+} ions by TOC analysis and

inductively coupled plasma–mass spectrometry (pH, 8; ionic strength, 0.05 mol/dm³; liquid-to-solid ratio, 0.5 m³/kg). The addition of non-irradiated HA weakened the sorption of Eu because of the lower sorption of neutral or negatively charged Eu–HA complexes compared with that of free Eu ions. The sorption of monovalent Cs ions was barely affected by the presence of HA and the gamma irradiation. The concentration ratios of the HA-complexed species (including decomposed HA) and the non-complexed species in the solid and liquid phases were evaluated by sequential filtration and chemical equilibrium calculations. The ratios were low in both phases for Cs, which supported the minimal contribution of HA to the sorption of Cs. However, the concentration ratio for Eu³⁺ in the liquid phase was high, indicating that the complexing ability of HA to Eu³⁺ was higher than that of HA to Cs⁺ ions. Therefore, the sorption of free Eu³⁺ dominated in the scenario involving the HA solution subjected to gamma irradiation under a radiation field near the HLW package.

Chapter 5 summarizes the general conclusions and proposes the possible applications for the estimation of radionuclide migration and future-work-related strategies.

5.2 Significance of this thesis

The dependence of gamma irradiation on the sorption ability of metal ions in the presence of HS and its basis, that is, apparent formation constants and complexation affinity, were investigated. The possible applications based on the results can be summarized as follows:

- (1) Information on gamma-irradiation-induced differences in chemical properties of macromolecules is lacking. A possible radiolysis mechanism of HSs was proposed in this thesis, which included the decomposition of HS molecules and changes in the acidic functional groups. This can facilitate the understanding of radiolysis mechanisms of other macromolecular mixtures, such as liquor, starch, and cellulose.

Additionally, the gamma-irradiation-induced changes in the ratio of the contents of $-COOH$ and phenolic $-OH$ can enable the understanding of the interactions of HSs with metal ions and complexation speciation. For example, in the non-irradiated HS system, $-COOH$ is known to be the main contributor to the complexation of metal ions with HSs [1]. In contrast, the role of phenolic $-OH$ in the complexation can dominate with the applied dose, indicating the formation of different complex species.

- (2) Several quantitative studies have been conducted on multisystems of metal ions and NOM (such as HSs) in the solid phase because of the heterogeneity of HS and the complexity of these systems. A simple filtration method was proposed in this study to evaluate the concentration distribution of four metal species (free metal ions and metal complexed in liquid phase, metal sorbed and complexes sorbed in solid phase). The metal ions in the >10 kDa fraction were regarded to be complexed with the HSs. Assuming that phthalic acid and salicylic acid were the typical fragmented components of the HS molecules in the <10 kDa fraction, a balance between acidic functional groups ($-COOH$ and phenolic $-OH$) was established to evaluate the contents of these two ligands, which helped in estimating the content of the metal complexed with HS in the <10 kDa fraction using thermodynamic calculations. This method can assist in enhancing the understanding of the behavior of metal ions and in analyzing the species in the prediction of radionuclide migration. For example, the conclusion of this study indicates that the direct sorption of non-complexed Eu ions on sedimentary rock is predominant rather than that of the Eu-HA complexes; therefore, the information on the sorption species is important for analyzing the desorption behavior [2], especially in the field of radioactive pollution remediation.
- (3) Based on the vast amount of data on the formation constants and sorption coefficients of metal ions, several comprehensive databases have been established, such as the

TDB project setup by Canada, France, Japan, the US, and the UK. These can help in providing high-quality, traceable, internally consistent, and internationally recognized chemical thermodynamic data of selected elements relevant to the safety of radioactive waste repositories, which can also assist in facilitating geochemical modelling of these systems. The NEA TDB Project has published 15 authoritative volumes consisting of thermochemical data for over 1500 species. The Thermodynamic, Sorption, & Diffusion Databases developed by JAEA compiles K_d data in buffer material and rock, which is a key parameter for assessing the performance of geological disposal strategies. The Rossendorf Expert System for Surface and Sorption Thermodynamics (RES³T), developed by Helmholtz–Zentrum Dresden–Rossendorf, is a digitized thermodynamic sorption database that is mineral-specific; therefore, it can be used for additive models of more complex solid phases, such as rocks and soils. It is worth noting that the formation constants of natural organic substances (such as HSs) with metal ions are not included in these databases because HSs are complex materials with multiple functional groups, and the proposed models for interpreting the complexation behavior of HSs are empirical and cannot unambiguously assign values of formation constants. Generally, typical organic ligands such as citric acid, oxalic acid, and isosaccharic acid are selected as the analogs of HSs. However, the results of this study indicate the generation of near-field gamma irradiation from the decay of nuclear waste, which can affect the sorption of metal ions in the presence of NOM. Therefore, the gamma-irradiation-corrected complexation and sorption data should probably be considered to improve the reliability of predicting the sorption of hazardous radionuclides and assess the performance of repositories.

5.3 Recommendations for future research

This thesis demonstrated that gamma irradiation could affect the complexation constant and sorption coefficient of metal ions in the presence of humic substance. In the further study, the modelling of these reactions in the gamma irradiation field could be established, based on a large number of the gamma-irradiation-corrected complexation and sorption data. Although this study has demonstrated the dependence of gamma irradiation on the apparent formation constants, the complexation affinity of metal ions with HSs, and the sorption behavior of metal ions in the presence of HSs, information on the role of gamma irradiation on the kinetics of metal–HS interactions remains insufficient, which is crucial for analyzing radionuclide migration in the environment. Most recent studies have focused on the thermodynamics of metal–HS interactions by presuming that the experimental systems reach equilibrium on the laboratory scale (several days or weeks). However, certain studies have indicated that the complexation reaction of metal ions with HSs can last for several years or even decades [3]. Therefore, the reliability of the thermodynamic data must be clarified, especially for long-term assessments. The molecular weight of HSs appears to be an important index for the kinetics of metal–HS interactions because of the complexity [4], macromolecules, and heterogeneity of HSs. The gamma irradiation could affect the kinetics of the metal–HS interactions in deep geologic repository environment.

Reference

- [1] P. Zhou, H. Yan, B. Gu, Competitive complexation of metal ions with humic substances, *Chemosphere* **58** (2005), 1327–1337.
- [2] H. Ashworth, L. Abrahamsen-Mills, N. Bryan, L. Foster, J.R. Lloyd, S. Kellet, S. Heath, Effect of humic acid & bacterial exudates on sorption–desorption interactions of ⁹⁰Sr with brucite, *Environ. Sci.: Processes Impacts* **20** (2018), 956–964.
- [3] T. A. Vasilchuk, The role of humic substances in the processes of complexation and detoxication (by the example of the dneiper reservoirs), *Hydrobiol.* **38** (2002).
- [4] G.R. Choppin, S.B. Clark, The kinetic interactions of metal ions with humic acids. *Mar. Chem.* **36** (1991), 27–38.

List of publications and presentations

趙 祺 (Zhao Qi)

List of journals (peer review):

1. Qi Zhao, Ryohei Goto, Takeshi Saito, Taishi Kobayashi, and Takayuki Sasaki. Effect of gamma-irradiation on complexation of humic substances with divalent calcium ion, *Chemosphere*, Vol. 256, 127021, 2020.
2. Qi Zhao, Taishi Kobayashi, Takeshi Saito, and Takayuki Sasaki. Gamma-irradiation-induced molecular-weight distribution and complexation affinity of humic acid with Cs^+ , Sr^{2+} and Eu^{3+} , *J. Hazard. Mater.*, Vol. 411, 125071, 2021.
3. Qi Zhao, Takeshi Saito, Kazuya Miyakawa, Hiroshi Sasamoto, Taishi Kobayashi, and Takayuki Sasaki. Sorption of Cs^+ and Eu^{3+} ions onto sedimentary rock in the presence of gamma-irradiated humic acid, *J. Hazard. Mater.*, Vol. 428, 128211, 2022.

List of Presentations:

1. Gamma-ray irradiation impact on complexation of humic substances with divalent calcium ions, *Poster presentation, 17th International Conference on Chemistry and Migration Behavior of Actinides and Fission Products in the Geosphere*, Kyoto University, Kyoto, Japan, September 2019.
2. Molecular size distribution of gamma-ray irradiated humic acid complexed with metal ions, *Oral conference presentation, Atomic Energy Society of Japan (AESJ) Spring Meeting*, March 2020.
3. Molecular-weight-dependent distribution of humic acid induced by gamma-irradiation complexed with metal ions, *Oral conference presentation, Japan Nuclear and Radiochemical Society (JNRS)*, September 2020.
4. Gamma-irradiation-induced molecular-weight-dependent distribution of humic acid complexed with metal ions, *Oral conference presentation, AESJ Spring Meeting*, March 2021.

Reports:

1. Qi Zhao, Ryohei Goto, Takeshi Saito, Taishi Kobayashi and Takayuki Sasaki. Effect of gamma-irradiation on complexation of humic substances with divalent calcium ion. *Annual Report of Quantum Science and Engineering center*, Kyoto University, Vol. 22, ISSN 1345-0700, 2020.

